

**Cross-wind from linear and angular satellite dynamics  
The GOCE perspective on horizontal and vertical wind in the thermosphere**

Visser, Tim

**DOI**

[10.4233/uuid:36063bcb-0a9b-4a14-bc36-cb18b43eb413](https://doi.org/10.4233/uuid:36063bcb-0a9b-4a14-bc36-cb18b43eb413)

**Publication date**

2019

**Document Version**

Final published version

**Citation (APA)**

Visser, T. (2019). *Cross-wind from linear and angular satellite dynamics: The GOCE perspective on horizontal and vertical wind in the thermosphere*. [Dissertation (TU Delft), Delft University of Technology]. <https://doi.org/10.4233/uuid:36063bcb-0a9b-4a14-bc36-cb18b43eb413>

**Important note**

To cite this publication, please use the final published version (if applicable).  
Please check the document version above.

**Copyright**

Other than for strictly personal use, it is not permitted to download, forward or distribute the text or part of it, without the consent of the author(s) and/or copyright holder(s), unless the work is under an open content license such as Creative Commons.

**Takedown policy**

Please contact us and provide details if you believe this document breaches copyrights.  
We will remove access to the work immediately and investigate your claim.

# **CROSS-WIND FROM LINEAR AND ANGULAR SATELLITE DYNAMICS**

THE GOCE PERSPECTIVE ON HORIZONTAL AND VERTICAL  
WIND IN THE THERMOSPHERE



# **CROSS-WIND FROM LINEAR AND ANGULAR SATELLITE DYNAMICS**

THE GOCE PERSPECTIVE ON HORIZONTAL AND VERTICAL  
WIND IN THE THERMOSPHERE

## **Proefschrift**

ter verkrijging van de graad van doctor  
aan de Technische Universiteit Delft,  
op gezag van de Rector Magnificus prof. dr. ir. T.H.J.J. van der Hagen,  
voorzitter van het College voor Promoties,  
in het openbaar te verdedigen op woensdag 27 november 2019 om 12:30 uur

door

**Tim VISSER**

Ingenieur in de Luchtvaart en Ruimtevaart,  
Technische Universiteit Delft, Delft, Nederland,  
geboren te Groningen, Nederland.

Dit proefschrift is goedgekeurd door de promotoren.

Samenstelling promotiecommissie:

|                                |   |
|--------------------------------|---|
| Rector magnificus,             | voorzitter                                |
| Prof. dr. ir. P.N.A.M. Visser, | Technische Universiteit Delft, promotor   |
| Dr. ir. C.C. de Visser,        | Technische Universiteit Delft, copromotor |

*Onafhankelijke leden:*

|                                    |   |
|------------------------------------|---|
| Prof. dr. S. Hickel                | Technische Universiteit Delft             |
| Prof. dr. F. Scarano               | Technische Universiteit Delft             |
| Prof. dr. C. Stolle                | GFZ, Helmholtz Zentrum, Duitsland         |
| Ir. R.H.N. Haagmans,               | Europese Ruimtevaartorganisatie           |
| Prof. dr. ir. H.W.J. Russchenberg, | Technische Universiteit Delft, reservelid |

*Overige leden:*

|                        |  |
|------------------------|--|
| Dr. ir. E.N. Doornbos, | Koninklijk Nederlands Meteorologisch Instituut |
|------------------------|--|



*Keywords:* Gravity field and steady-state Ocean Circulation Explorer (GOCE), Thermospheric wind, Vertical wind, Satellite angular dynamics

*Printed by:* Ipskamp Printing

*Front & Back:* A photo of a relief inspired by Jan Schoonhoven, depicting GOCE in orbit, centered on the horizon, measuring both the Earth below and the skies above.

Copyright © 2019 by T. Visser

ISBN 978-94-028-1787-4

An electronic version of this dissertation is available at

<http://repository.tudelft.nl/>.

***De invloed van matige wind op kleren***

*Ga je naar het strand? Mag ik  
als je terugkomt het zand  
uit je schoenen voor de  
bodem van mijn aquarium?*

K. Schippers, *Sonatines door het open raam*, Querido (1972)



# CONTENTS

|  |             |
|--|-------------|
| <b>Summary</b>   | <b>ix</b>   |
| <b>Samenvatting</b>  | <b>xiii</b> |
| <b>Preface</b>   | <b>xvii</b> |
| <b>1 Introduction</b>  | <b>1</b>    |
| 1.1 The thermosphere . . . . .                                 | 2           |
| 1.2 Thermospheric measurements . . . . .                       | 4           |
| 1.3 Satellite aerodynamics . . . . .                           | 7           |
| 1.4 The GOCE mission . . . . .                                 | 8           |
| 1.5 Research goal . . . . .                                    | 9           |
| <b>2 Torque model verification</b>                             | <b>13</b>   |
| 2.1 Introduction . . . . .                                     | 14          |
| 2.2 The GOCE mission and datasets . . . . .                    | 16          |
| 2.3 Torque models . . . . .                                    | 20          |
| 2.3.1 Magnetic control . . . . .                               | 20          |
| 2.3.2 Aerodynamics . . . . .                                   | 23          |
| 2.3.3 Gravity gradient . . . . .                               | 25          |
| 2.3.4 Solar radiation . . . . .                                | 25          |
| 2.3.5 Ion thruster . . . . .                                   | 26          |
| 2.3.6 Constant dipoles of spacecraft bus and payload . . . . . | 27          |
| 2.4 Validation . . . . .                                       | 31          |
| 2.4.1 Magnetic control torque . . . . .                        | 31          |
| 2.4.2 Aerodynamics . . . . .                                   | 37          |
| 2.4.3 Gravity gradient . . . . .                               | 39          |
| 2.4.4 Solar radiation pressure . . . . .                       | 39          |
| 2.4.5 Ion thruster . . . . .                                   | 44          |
| 2.4.6 Constant dipoles of spacecraft bus and payload . . . . . | 44          |
| 2.4.7 Complete model . . . . .                                 | 46          |
| 2.5 Discussion and conclusion . . . . .                        | 46          |
| <b>3 Cross-wind from accelerations</b>                         | <b>49</b>   |
| 3.1 Introduction . . . . .                                     | 50          |
| 3.2 GOCE force and torque models . . . . .                     | 51          |
| 3.3 Methodology . . . . .                                      | 53          |
| 3.4 Results . . . . .  | 59          |
| 3.5 Sensitivity analysis . . . . .                             | 63          |
| 3.6 Conclusion . . . . .                                       | 66          |

---

|          |                                       |            |
|----------|---------------------------------------|------------|
| <b>4</b> | <b>Vertical wind</b>                  | <b>71</b>  |
| 4.1      | Introduction . . . . .                | 73         |
| 4.2      | Data. . . . .                         | 74         |
| 4.3      | Methodology . . . . .                 | 78         |
| 4.4      | Validation . . . . .                  | 82         |
| 4.5      | Results . . . . .                     | 83         |
| 4.6      | Conclusion . . . . .                  | 91         |
| <b>5</b> | <b>The accommodation coefficient</b>  | <b>97</b>  |
| 5.1      | Introduction . . . . .                | 97         |
| 5.2      | Estimated parameters. . . . .         | 99         |
|          | 5.2.1 Methodology. . . . .            | 99         |
|          | 5.2.2 Results. . . . .                | 100        |
| 5.3      | Aerodynamic coefficients . . . . .    | 103        |
|          | 5.3.1 Methodology. . . . .            | 105        |
|          | 5.3.2 Results. . . . .                | 106        |
| 5.4      | Wind comparison. . . . .              | 106        |
|          | 5.4.1 Methodology. . . . .            | 107        |
|          | 5.4.2 Results. . . . .                | 108        |
| 5.5      | Conclusion . . . . .                  | 110        |
| <b>6</b> | <b>Conclusion</b>                     | <b>113</b> |
| 6.1      | Research questions and goal . . . . . | 113        |
| 6.2      | Recommendations . . . . .             | 117        |
|          | <b>References</b>                     | <b>119</b> |
|          | <b>Curriculum Vitae</b>               | <b>127</b> |
|          | <b>List of Publications</b>           | <b>129</b> |

# SUMMARY

The decay of satellite orbits has been used extensively to obtain thermospheric density measurements. With the introduction of accelerometers in spacecraft, the spatial resolution of these data could be increased. At the same time, the direction of the measured acceleration provides a measure for the direction of the incoming flow, and therefore of the local cross-wind. In this thesis, the angular acceleration of the Gravity field and steady-state Ocean Circulation Explorer (GOCE) satellite, an Earth explorer by the European Space Agency (ESA), is used as a source for such thermospheric wind data for the first time. The goal is to improve aerodynamic parameter estimates and assess the quality of accelerometer-derived wind data by comparing this new data set to that derived from linear accelerations.

The first step in obtaining wind data from angular accelerations, is to model the disturbance torques acting on the satellite. The GOCE satellite, equipped with accurate accelerometers, star trackers, and GPS receivers, presents an opportunity to validate these models. Although the forces on GOCE and other accelerometer-carrying missions have been extensively analyzed in the past, a similar analysis has so far not yet been made for the torques. Therefore we present a set of torque models for the GOCE satellite. It consists of six main parts: 1) magnetic torquer actuators, 2) aerodynamic torque, 3) gravity gradient torque, 4) solar radiation pressure torque, 5) thruster torque, and 6) passive magnetic torque. The magnetic properties of the payload are approximated using a parametrization, of which the parameters are estimated from the observation data. Based on data recorded during selected spacecraft events, the model for the control torques can be validated and error sources are identified in the other models. The models perform best in roll and pitch, where the standard deviation of the difference between modeled and observed torques is reduced to 15.2% and 2.1% of the standard deviation of the control torque around those axes respectively. In yaw the standard deviation is significantly larger at 30.5%. The remaining differences between models and observations show magnetic signatures due to electric currents and signatures of aerodynamic model errors. The latter correspond well with an increase in thermosphere density and wind speed with increased geomagnetic activity. The observed pitch torque is found to be a potential source of vertical wind data.

Thermospheric wind measurements obtained from linear non-gravitational accelerations of the GOCE satellite show discrepancies when compared to ground-based measurements. Therefore the cross-wind is derived from both the linear and the angular accelerations using a newly developed iterative algorithm. The two resulting data sets are compared to test the validity of wind derived from angular accelerations and quantify the uncertainty in accelerometer-derived wind data. In general the difference is found to be less than 50 m/s vertically after high-pass filtering at 4000 km spatial scales, and 100 m/s horizontally. A sensitivity analysis reveals that continuous thrusting is a major source of uncertainty in the torque-derived wind, as are the magnetic properties of the

satellite. The energy accommodation coefficient is identified as a particularly promising parameter for improving the consistency of thermospheric cross-wind data sets in the future. The algorithm may be applied to obtain density and cross-wind from other satellite missions that lack accelerometer data, provided the attitude and orbit are known with sufficient accuracy.

The vertical wind derived from the linear accelerations of the GOCE satellite is compared to wind data derived from the mass spectrometers of the Atmosphere Explorer C (AE-C) and E (AE-E), and Dynamics Explorer 2 (DE-2) satellites, all operated by the National Aeronautics and Space Administration (NASA). From a statistical analysis of the 120-second moving-window standard deviation of the vertical wind ( $\sigma(V_z)$ ), no systematic discrepancy is found between the accelerometer-derived and the mass spectrometer-derived data. The validated GOCE data is then used to investigate the influence of several parameters and indices on the vertical wind activity. To this end, the probability distribution of  $\sigma(V_z)$  is plotted after distributing the data over bins of the parameter under investigation. The vertical wind is found to respond strongly to geomagnetic activity at high latitudes, although the response settles around a maximum standard deviation of 50 m/s at an Auroral Electrojet index of 800. The dependence on magnetic local time changes with magnetic latitude, peaking around 04:30 magnetic local time over the polar cap and around 01:30 and 13:30 in the auroral oval. Seasonal effects only become visible at low- to mid-latitudes, revealing a peak wind in both local summer and winter. The vertical wind is not affected by the solar activity level.

In the aerodynamic modeling of satellites, the energy accommodation coefficient ( $\alpha_E$ ) plays a central role. To find an experimental value for this parameter, the consistency can be investigated of thermospheric density and wind simultaneously observed from the linear and angular motion of a satellite. The applicability of this approach to the GOCE satellite is investigated in three ways. First of all, the magnetic dipoles, thruster misalignment angles, and vertical acceleration bias are estimated for a range of accommodation coefficient values. No significant improvement is however observed in these estimates. Second of all, the sensitivity of the difference between force- and torque-derived wind to  $\alpha_E$  is evaluated using the aerodynamic model. In the horizontal wind component, a bias of up to 10 m/s is expected between the two data sets; in the vertical component a scale factor up to 10%. Finally, the wind is derived from forces and from torques for a range of accommodation coefficients, and the two data sets are compared. The bias in the horizontal wind component is found to be reduced by the thruster misalignment estimates to a level below the uncertainty caused by those estimates. The vertical wind scale factor suggests the optimal accommodation coefficient lies in the range between 0.80 and 0.93, but this result strongly depends on the torque model set-up. We conclude that more accurate torque models are required to find an optimal accommodation coefficient based on simultaneous observation of linear and angular motion of GOCE.

Since the difference between force- and torque-derived wind is rather insensitive to aerodynamic model parameters for GOCE, we conclude that this satellite is not particularly suitable for reaching the research goal. We therefore recommend that other satellites are considered for a study as the one described in this dissertation. Especially the accelerometer-carrying LEO missions CHAMP, GRACE, and Swarm are promising candi-

dates, as they have a less symmetric geometric design. This will likely lead to a relatively stronger aerodynamic signal in roll, and a smaller dependency between the force and torque components. A future atmospheric research mission carrying both accelerometers and a mass spectrometer is required to convincingly validate the different sources of thermospheric data, and conclusively improve the aerodynamic models of satellites.



# SAMENVATTING

Het verval van satellietbanen is al uitgebreid gebruikt voor het bepalen van de dichtheid van de thermosfeer. Door de introductie van versnellingsmeters in ruimtevaartuigen is de ruimtelijke resolutie van deze meetgegevens verhoogd. Tegelijkertijd biedt de richting van de gemeten versnelling de mogelijkheid om de richting van de luchtstroom te bepalen, en daarmee de lokale wind. In dit proefschrift worden voor het eerst de hoekversnellingen van de *Gravity field and steady-state Ocean Circulation Explorer* (GOCE) satelliet, een aardobservatiesatelliet van de Europese Ruimtevaartorganisatie (ESA), gebruikt als bron voor windmetingen in de thermosfeer. Het doel is om de schattingen van aerodynamische parameters te verbeteren en de kwaliteit te bepalen van windmetingen afgeleid uit versnellingen, door de nieuwe metingen te vergelijken met die afgeleid uit lineaire versnellingen.

De eerste stap in het meten van de wind via de hoekversnellingen is het modelleren van de verstoringen die op de satelliet werken. De GOCE satelliet, uitgerust met accurate versnellingsmeters, stersensoren en GPS ontvangers, biedt een uitgelezen mogelijkheid om deze modellen te valideren. Hoewel de krachten die op GOCE en andere versnellingsmetermissies werken in het verleden uitgebreid zijn bestudeerd, is een dergelijke analyse tot dusver niet uitgevoerd voor de momenten. Daarom presenteren wij een verzameling momentmodellen voor de GOCE satelliet. Die bestaat uit zes hoofdbestanddelen: 1) aansturing door electromagnetische spoelen, 2) aerodynamisch moment, 3) zwaartekrachtsgradiëntmoment, 4) moment door stralingsdruk van de zon, 5) moment door de stuwmotor, en 6) passieve magnetische momenten. De magnetische eigenschappen van de wetenschappelijke lading worden benaderd door een parametrisatie, waarvan de parameters worden bepaald uit de verschillende metingen. Door specifieke situaties uit de metingen apart te beschouwen, kan het model voor de electromagnetische aansturing worden gevalideerd en de bronnen van fouten in andere modellen worden geïdentificeerd. De modellen presteren het beste in de rol- en stampriching, waar de standaarddeviatie beperkt blijft tot respectievelijk 15.2% en 2.1% van de standaarddeviatie van het besturingsmoment rond deze assen. In de gierrichting is de standaarddeviatie met 30.5% significant hoger. De overgebleven verschillen tussen model en observatie lijken overeen te stemmen met magnetische signalen door elektrische stromen in de satelliet, alsmede met delen van het aerodynamisch model. Het laatste komt overeen met een verhoging van de dichtheid en windsnelheid bij verhoogde geomagnetische activiteit. Het stampmoment wordt aangewezen als mogelijke bron om verticale wind uit af te leiden.

Windmetingen in de thermosfeer afgeleid uit de lineaire versnellingen van de GOCE satelliet komen niet geheel overeen met metingen vanaf de grond. Daarom wordt de wind afgeleid uit zowel de lineaire als de hoekversnellingen met behulp van een nieuw iteratief algoritme. De twee resulterende metingen worden met elkaar vergeleken om zowel de geldigheid van de wind uit hoekversnellingen te bepalen, als de onzekerheid in

de wind uit versnellingen in het algemeen te kwantificeren. In het algemeen is het verschil tussen de twee metingen minder dan 50 m/s verticaal na het wegfilteren van lage frequenties, en 100 m/s horizontaal. Een gevoeligheidsanalyse onthult dat de continue stuwkracht een belangrijke bron is van onzekerheid in de windmetingen afgeleid uit de momenten, net als de magnetische eigenschappen van de satelliet. De energieaccommodatiecoëfficiënt valt op als bijzonder veelbelovende parameter voor het bewerkstelligen van toekomstige verbeteringen van de consistentie van thermosferische windmetingen. Het nieuw ontwikkelde algoritme kan toegepast worden om dichtheid en wind te bepalen met behulp van satellieten zonder versnellingsmeters, als de standhoek en baan met voldoende precisie worden gemeten.

De verticale wind afgeleid uit de lineaire versnellingen van de GOCE satelliet wordt vergeleken met windmetingen van de massaspectrometers van de *Atmosphere Explorer C* (AE-C) en *E* (AE-E), en *Dynamics Explorer 2* (DE-2) satellieten, alle gelanceerd door de *National Aeronautics and Space Administration* (NASA).. Uit een statistische analyse van de 120-seconden brede voortschrijdende standaarddeviatie van de verticale wind ( $\sigma(V_z)$ ) wordt geen systematisch verschil gevonden tussen de metingen uit versnellingen aan de ene kant, en die uit de massaspectrometers aan de andere kant. De gevalideerde metingen van GOCE worden vervolgens gebruikt om de invloed te onderzoeken van verscheidene parameters en indices op de verticale windactiviteit. Daartoe wordt de kansverdeling van  $\sigma(V_z)$  geplot, nadat de gegevens over klassen van een bepaalde parameter zijn verdeeld. Hieruit blijkt dat de verticale wind sterk reageert op geomagnetische activiteit op hoge breedtegraad, al bereikt de activiteit een maximum standaarddeviatie van 50 m/s bij een *Auroral Electrojet* index van 800. De trend in de lokale magnetische tijd is afhankelijk van de breedtegraad, met een piek rond 04:30 magnetische lokale tijd boven de poolkap en rond 01:30 en 13:30 in de poollichtovaal. Seizoenseffecten worden slechts zichtbaar op lage breedtegraden, waar een piek te vinden is in de lokale zomer en winter. De verticale wind wordt niet beïnvloed door de zonneactiviteit.

Binnen het modeleren van de aerodynamica van satellieten speelt de energieaccommodatiecoëfficiënt ( $\alpha_E$ ) een centrale rol. Om een experimentele waarde te vinden voor deze parameter kan de consistentie worden onderzocht van de dichtheid en wind in de thermosfeer die tegelijk gemeten wordt uit lineaire en hoekversnellingen van een satelliet. De toepasbaarheid van deze methode op de GOCE satelliet wordt op drie manieren onderzocht. Ten eerste worden de magnetische dipolen, de standhoeken van de stuwmotor en de afwijking van de verticale versnelling geschat op basis van verschillende waarden voor de accommodatiecoëfficiënt. Er wordt echter geen significante verbetering waargenomen in deze schattingen. Ten tweede wordt de gevoeligheid van het verschil tussen wind uit lineaire en hoekversnellingen voor  $\alpha_E$  bepaald met behulp van het aerodynamisch model. In de horizontale windcomponent wordt een constante afwijking van 10 m/s verwacht tussen de twee metingen; in de verticale component een lineaire schaalfactor tot 10%. Als laatste wordt de wind berekend uit de krachten en uit de momenten voor een waaier aan accommodatiecoëfficiënten, en de twee metingen worden vergeleken. De schatting van de standhoeken van de stuwmotor blijken de constante afwijking tussen de twee metingen te reduceren tot onder het onzekerheidsniveau van deze schattingen. De schaalfactoren tussen de verticale windmetingen suggereren dat de optimale accommodatiecoëfficiënt ligt tussen 0.80 en 0.93, maar dit

resultaat hangt sterk af van de opbouw van het momentenmodel. We komen dan ook tot de conclusie dat meer accurate momentenmodellen nodig zijn om een optimale accommodatiecoëfficiënt te vinden op basis van gelijktijdige observatie van de lineaire en hoekbeweging van GOCE.

Omdat het verschil tussen wind uit krachten en uit momenten in het geval van GOCE vrij ongevoelig is voor aerodynamische modelparameters, trekken we de conclusie dat deze satelliet niet bij uitstek geschikt is voor het behalen van ons onderzoeksdoel. We doen daarom de aanbeveling om andere satellieten te overwegen als onderzoeksobject voor de studie die in dit proefschrift wordt beschreven. De versnellingsmetermissies in een lage baan CHAMP, GRACE en Swarm lijken bij uitstek geschikt, daar zij een minder symmetrisch ontwerp hebben. Dit zal waarschijnlijk leiden tot een groter aerodynamisch signaal in de rolrichting, en een verminderde afhankelijkheid tussen kracht- en momentcomponenten. Een toekomstige onderzoeksmissie die zowel versnellingsmeters als een massaspectrometer aan boord heeft, is nodig om op overtuigende wijze de verschillende windmetingen te valideren en het aerodynamisch model van satellieten te verbeteren.



# PREFACE

In science, as in life itself, things are often not as straightforward as they seem. When I first read the research proposal that forms the basis of this work, I was struck by the simplicity of the idea: to measure the wind in the thermosphere by its effect on the attitude motion of a satellite. Looking more closely at the artist impression of the satellite in question, the arrow-shaped ‘Space Ferrari’ GOCE, the research suggestion became even more obvious to me. Clearly the weather vane stability of this sleek design would result in a strong wind signal.

It was only when I started working with the mission data and documentation, that I realized why no one had yet ventured into the maze that is GOCE’s attitude motion. Since the mission was only to retrieve the Earth’s gravity field and ocean currents, most of the documentation and data was dedicated to the description, measurements, and calibration of the gradiometer: the contraption of six accelerometers at the heart of the satellite. After studying said resources, I found myself knowing exactly what GOCE was doing, but having no idea why it was doing exactly that.

Luckily I found ESA, specifically Björn, Christian, Roger, and Rune, on my side at this point. Enthusiastic about the fact that someone was still interested in this successful, but old mission, they swiftly provided me with the proper resources to help me move forward. File after file, data set after data set, were recovered from the most obscure corners of the ESA repository. Models that notified me of the significant torque caused by on-board magnets; currents running through the attitude control actuators; magnetometer calibration routines; even currents coming from the individual solar panels. No request was denied, no questions were asked. All was provided in good faith that I was going to put it to good use, even when I was not always so sure of that myself.

As the torque models were slowly taking shape, I became aware of a gentle, yet increasing push from my supervisors, Coen and Eelco, to visit meetings and present at conferences. This push was as necessary as it was successful: it took me places I would probably otherwise never have visited. Among them the world famous towns of Kissimmee before it became the backdrop of the critically acclaimed art-house movie *The Florida Project*, Banff during avalanche season, and Ostseebad Kühlungsborn in January. Although some say traveling is all about the journey, not the destination, I would argue it is about something entirely different: your companions. I will never forget how we spent the whole first day in Kühlungsborn talking about how we got to Kühlungsborn; how Jose convinced me to operate the excavator in the ball pit of a Prague toy store (there is no consensus on how much convincing was required); how Christian and I crossed a frozen Lake Louise; or how Dieter, Ezra, Rody, and I watched a rocket launch from Cape Canaveral, alligators in the Everglades, and monkeys (as in the Dutch expression) on Miami Beach, all in one single day. So thank you, companions, for making my travels unforgettable. And a special thanks to Claudia for inviting me to so many SPP DynamicEarth meetings, which were among the most valuable and fun of all.

But as all (former) PhD candidates know, doing a PhD is not all fun. Most of the peers I have met over the last four years would even argue that the majority of it is not fun at all, and I am inclined to agree. A large part of it is trying to understand why your code stopped running, why everything broke over the weekend, what you could possibly present at the conference next week, why you wanted this in the first place, and ultimately: what is the point of anything anyway? It was especially at those times that I was very glad to be part of the infamous 9.18-gang. A group of hardened individuals with exceptional talents: Günther – Gundrano – March, with the childlike innocence that can make a brand new MacBook crash; Jacco – Go, Go, Gadget – Geul, with the telepathic ability to get a cut from a knife that is five meters away; and Svenja – Master Baker – Woicke, with the iron discipline that allows her to have cheesecake for dinner and still stay top fit. Between them they had the power to pull me through every setback with a combination of laughter and mental support. I love you guys, and would not have made it without you. The same holds for all the other ninth floor PhD's and postdoc's: thank you all for the vital ridiculousness, and your patience in listening to my ramblings about life, the universe, and everything.

As the lack of progress in scientific work can be maddening, it is vital to touch base from time to time. Luckily I could often hang-out with 'the kids': one of the DSE groups that I was lucky enough to supervise, or my MSc student Rutger. Outside of work I was always welcome at my parents', brothers', and sister's homes. While the half-year birthday carousel got my blood sugar to acceptable levels and beyond, it were the many visits in between that helped me put my daily struggles in perspective. It is just extremely difficult to worry about work when you are building a truck out of Duplo with your nephews, or while hacking and slashing away at some digital bad guys, or with a guinea pig on your lap. The same is true for painting a ceiling or sanding a wooden floor, for which I have to thank Gerben and Marielonne as much as they have thanked me; for the regular evening talks with Lisanne or Carolien about anything but my work; and for the many high-fives with Yoda. Thank you all for keeping me grounded.

All the above, combined with the organizational and mental support of Relly and the unwavering support and dedication of Coen, Eelco, and Pieter, brings me where I am today: at my dinner table on a Sunday night, finishing the last sentences of this book. And while you may be preparing to read the rest of it, I finally find myself in a position to say: that's it, I'm done, Tim out.

*Tim Visser*  
*Delft, 7 April 2019*

# 1

## INTRODUCTION

Starting from the very first artificial satellite, the Soviet Union's Sputnik 1, atmospheric research has been at the core of many satellite missions. For most satellites in a low Earth orbit (LEO), this research follows a similar approach. As the satellite moves through the top layer of the Earth's atmosphere, it is slowed down by the aerodynamic drag induced by the air particles. The resulting reduction in speed causes the satellite to drop to a lower orbit. The rate of change of the orbit is thus an indirect measure of the density of the atmosphere at the satellite's altitude. The step from aerodynamic acceleration to atmospheric density however, requires an aerodynamic model. In the process of gathering bulk data from large amounts of satellites, the aerodynamic model has often been reduced to a single drag coefficient. For simple designs, such as spherical geometries, an estimate for the drag coefficient suffices. For more complex shapes however, the drag may depend heavily on the attitude of the spacecraft, and a more advanced aerodynamic model is required.

The introduction of miniaturized accelerometers into satellite-based atmospheric research, allowed for a sharp increase in the accuracy and resolution of density measurements. Instead of integrating the decelerating effect over the orbit, the accelerations could be measured directly. On top of that, lateral and vertical accelerations were added to the observation set, providing a measurement of the direction of the incoming flow of particles. To translate these measurements into wind observations however, the aerodynamic model had to be expanded with lateral and vertical forces, again depending on the attitude of the spacecraft.

For modern accelerometer-carrying missions, such as German CHAMP, US/German GRACE, and ESA GOCE (*Floberghagen et al., 2011*) and Swarm (*Olsen et al., 2013*), the acceleration and attitude can be measured with exceptional precision, leaving the aerodynamic model as the main source of uncertainty in the atmospheric measurements. Apart from a need to further improve the aerodynamic model, this also presents an opportunity to do so. After all, as the amount of measurements increases, more parameters can be estimated simultaneously. Therefore the aim of this thesis is to improve the aerodynamic model of satellites, by optimizing for consistency between different, yet si-

multaneously gathered wind data sets. More specifically, we compare the wind derived from the angular dynamics of the GOCE satellite, to that derived from its linear motion.

Before diving into this topic, several concepts require introduction. First, in section 1.1, the layer of the atmosphere in which GOCE made its orbits, the thermosphere, is introduced. The response of this highly dynamical layer to solar illumination, geomagnetic activity, and forcing from lower layers is discussed in some detail. A general understanding of this behavior is vital for the validation of wind data in the remainder of this dissertation. Second, in section 1.2, the methods of taking measurements of the thermosphere are listed and briefly discussed. The focus lies on in situ observations, as they form the basis for all data used in this work. Third, in section 1.3, the different ways to model satellite aerodynamics are presented. Most importantly, the most sensitive aerodynamic parameter, the energy accommodation coefficient, is introduced. In section 1.4 the GOCE mission is described in some detail, as it forms the primary subject of study in this thesis. Finally, in section 1.5 the goal of this work is formulated, and the research questions are listed.

## 1.1. THE THERMOSPHERE

The atmosphere of the Earth is built up of several layers, that are characterized by their temperature profile (see Figure 1.1). In the troposphere (0–10 km altitude) and the mesosphere (50–100 km) temperature decreases with increasing altitude, while in the stratosphere (10–50 km) and the thermosphere (> 100 km) temperature increases. Close to the lower boundary of the thermosphere, at approximately 100 km, the atmosphere becomes too thin for an aircraft to create sufficient lift at velocities below the local orbital velocity. This so called Kármán line is therefore often used to define the edge of space. Below it, one can theoretically fly a plane; above it lies the realm of satellites.

Instead of being strictly bound, the atmosphere slowly dies out as the density decreases further and further with increasing altitude. The upper bound of the thermosphere, defined by the altitude at which the density is too low for particles to collide, is not easily found. On top of that, the density profile of the thermosphere depends strongly on external factors, including solar illumination, bombardment by the solar wind, and waves and tides propagating through the atmosphere. The density variations in turn give rise to horizontal and vertical motion, resulting in a complex dynamical system.

Solar illumination primarily causes slow variations in density, ranging from diurnal to multi-year variations. During the day, the thermosphere heats up and expands, causing significant drag on satellites at altitudes up to and exceeding 1000 km. This day-time bulge lags approximately two hours behind the sub-solar point. During the night, the atmosphere contracts again, reducing the density by up to a factor 5 at 500 km altitude. On top of that, a semiannual variation of about 30% can be observed, which peaks just after equinox, and may be due to a variation in mixing of the different atmospheric constituents (*Fuller-Rowell, 1998*). The intensity of the illumination depends on the 11-year solar cycle, which introduces a long-term oscillation in the density of up to a factor 20.

Fast changes in local density occur during geomagnetic storms, or due to waves propagating from lower layers of the atmosphere. Geomagnetic storms occur when the solar wind, consisting of charged particles ejected from the Sun's corona, reaches the

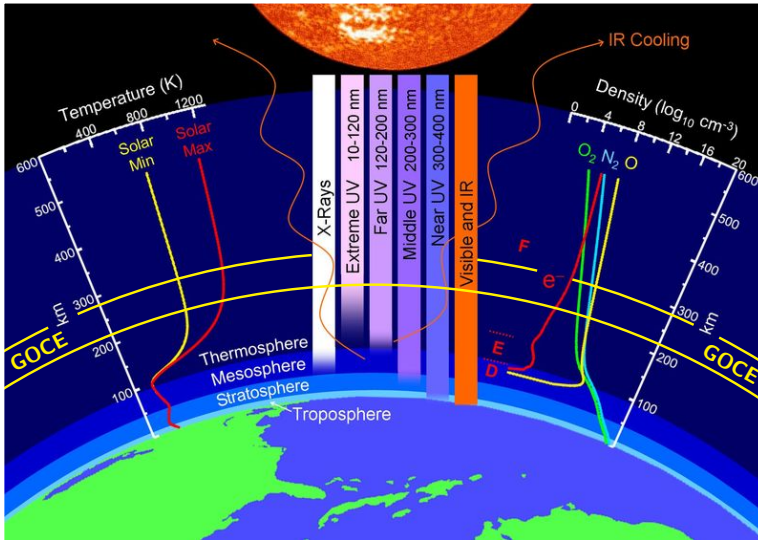


Figure 1.1: Overview of the structure of the atmosphere, including the temperature profile, the atmospheric constituents, and the orbit altitude range of GOCE (in yellow). (Figure adapted from J. Emmert (NRL).)

Earth. When the particles arrive at the magnetic field of the Earth, they are deflected and start following the magnetic field lines. As some solar wind and magnetospheric particles eventually enter the atmosphere near the magnetic poles, they interact with the neutral particles, which causes the aurora and heats the neutrals locally. These temperature enhancements cause a local expansion of the atmosphere, and thus a density increase in the thermosphere above of up to several orders of magnitude. Density variations due to gravity waves are significantly smaller. They may be caused by events in the lower regions of the atmosphere, or even by earthquakes ([Garcia et al., 2013](#)). The air that is moving upwards due to such events, is slowed down by gravity, which creates consecutive upward and downward wind peaks.

The differences in density between different locations are the main driver of horizontal wind in the thermosphere. The imbalance between the day- and night-side induces a strong horizontal flow of a few hundred meters per second away from the day-side bulge. Along the auroral oval however, ions flow towards the day-side, dragging along neutral particles in their vicinity. This causes a flow reversal, concentrated near the dusk and dawn local times, that is enhanced during geomagnetic storms ([Rees et al., 1983](#), e.g.). During severe geomagnetic events, wind speeds exceeding 1000 m/s have been observed.

Vertical wind in the thermosphere follows a completely different pattern. The diurnal expansion and contraction of the atmosphere (sometimes referred to as 'breath') does translate to vertical motion, but this is generally limited to a few meters per second ([Smith, 1998](#)). Contrary to horizontal flows, vertical velocity enhancements are often limited both in space and time. On the one hand, small local enhancements of 10–50 m/s have been observed to persist for several hours, at a wide range of latitudes ([Anderson](#)

*et al.*, 2012; *Larsen and Meriwether*, 2012). The direction of these winds has been linked to local time, being predominantly downward during the day and upward around midnight (*Sipler et al.*, 1995). On the other hand, the strongest vertical winds are observed in the auroral region and over the polar cap, especially in the midnight–dawn sector (*Innis and Conde*, 2002). They are generally characterized by a wavelet structure, propagating both in space and time. Strong vertical winds have been observed over Antarctica spanning at least  $10^5$  km<sup>2</sup>, and moving along with the expansion of the auroral oval under geomagnetic forcing (*Smith and Hernandez*, 1995). These waves generally peak at 100–150 m/s, at least a factor two smaller than the horizontal wind component (*Innis et al.*, 1999, e.g.).

The density, horizontal, and vertical wind influence each other, creating a complex dynamic in the thermosphere. A vertical motion may transport high-density air to a higher altitude, where it is dispersed horizontally. In turn, the resulting horizontal wind may distribute the density increase over the Earth, causing a cascade of interactions between these three entities. In the past, vertical winds have often been ignored, because measurements were rare and difficult to interpret. The characterization of vertical wind presented in chapter 4 of this thesis could aid atmosphere researchers to include this essential piece of information in their models.

## 1.2. THERMOSPHERIC MEASUREMENTS

Thermospheric properties can be measured in several different ways, that depend on a wide range of physical phenomena. Techniques have been developed to infer wind from the light emitted by the night sky, from following trace gases, from spectrometry, and from the motion of satellites. In this section a short overview is provided of the dominant methods.

The primary source of thermospheric wind data is Fabry–Perot Interferometry (FPI). In this method, the Doppler shift in the airglow emission of the night sky is measured at a specific wavelength. Based on the change in wavelength, the velocity of the air with respect to the observer can be calculated. In order to properly observe these small changes in wavelength, night-time clear-sky conditions are required. Most FPI measurements are made from ground stations, that can be found around the world, but are most concentrated near the North and South Pole. These stations can only operate during night-time clear-sky conditions, as obstructions and abundant scattered light would prevent any measurement from being made. Ground-based FPI measurements are therefore limited in both the measurement location and the local time of observation. FPI equipment has also been flown on several satellites, including the Atmosphere Explorers and Dynamics Explorer 2. In those cases, this measurement technique was used to obtain along-track winds, as this component cannot be inferred from other observations. Although direct sunlight into the receiver would still prevent measurements from being made, a much wider range of local times and locations (along the ground track) could be observed. One of the major flaws of FPI is that it requires a zero Doppler baseline, which can be difficult to obtain. In many cases, FPI equipment is calibrated with the assumption that the average vertical wind is zero over a given amount of time (*Aruliah and Rees*, 1995). It has been suggested that, combining all error sources, large wind peaks measured with FPI may be up to 100% uncertain (*Harding et al.*, 2017).

Contrary to FPI, all other measurement techniques require at least part of the set-up to reach the thermosphere. As this layer of the atmosphere is out of reach for aircraft and balloons, the simplest option is to send a sounding rocket. Apart from taking direct measurements with thermometers, pressure gauges, and other equipment, the rocket's trajectory presents the opportunity to inject a trace gas into its surroundings. By tracking the movement of this trace gas from the ground, wind patterns at the altitude of the gas can be deduced. Due to its high speed and short lifetime, sounding rockets generally provide a single altitude profile of atmospheric properties, at a single location and time.

To obtain longer time series of in situ thermospheric observations, satellites are the only remaining candidate. Satellite missions dedicated to direct observation of the thermosphere date back to the seventies and eighties of the twentieth century, when a range of Atmosphere Explorers and the Dynamics Explorer 2 were flown (see Figure 1.2). These satellites all relied on mass spectrometry to obtain wind measurements (*Spencer et al., 1973a, 1981*). In such measurements, the orifice through which particles enter the measurement chamber is partially closed by a moving baffle. By moving the baffle, a range of directions of incoming flow is scanned. The direction for which the baffle blocks the largest amount of incoming particles, is the most likely direction of incoming flow. Combined with the orbital velocity and the spacecraft attitude, this measurement provides the cross-track wind velocity. Depending on the orientation of the baffle, either the vertical or the horizontal cross-wind can be measured. Note that a wind along the track of the satellite cannot be measured in this way. A headwind for example, would align the incoming flow velocity more with the orbit direction. The same measurement can however be induced by a smaller cross-track wind. Therefore the along-track wind is either assumed to be small, or measured using FPI (as was the case for the Dynamics Explorer 2 (*Hoffman, 1980*)).

Finally, the most common satellite-based observation technique is that of tracking the spacecraft's motion as it traverses the thermosphere. In its simplest form, it consists of tracking the orbit of a satellite, and inferring the neutral density from its decay. This method has been applied to the very first artificial satellite, Sputnik 1, and many thereafter. The temporal resolution of orbit-based densities is however limited by the need for integration (from aerodynamic acceleration to orbit velocity and position), and potentially the scarcity of tracking opportunities. This resolution can be improved if the satellite is continuously tracked, for example by using on-board GPS receivers, or even more drastically by directly measuring the acceleration. An added benefit of the latter, is that the direction of acceleration can be measured as well, which allows for cross-track winds to be observed (*Doornbos et al., 2010*, e.g.). Similar to the spectrometer measurements, the along-track wind component cannot be distinguished from an increase in density from acceleration measurements alone.

Observation of the spacecraft dynamics, be it from orbit tracking or accelerometry, is only an indirect measurement of thermospheric properties. Between the atmosphere and the acceleration it causes, lie the aerodynamic properties of the spacecraft. Initially, aerodynamic drag coefficients were simply assumed to have a certain value, especially for simple geometric designs like spheres. Later, attempts were made to circumvent this assumption by analyzing a large amount of similar objects (*Bowman and Moe, 2005*), or by simultaneously observing the linear and angular dynamics of the so called paddle-

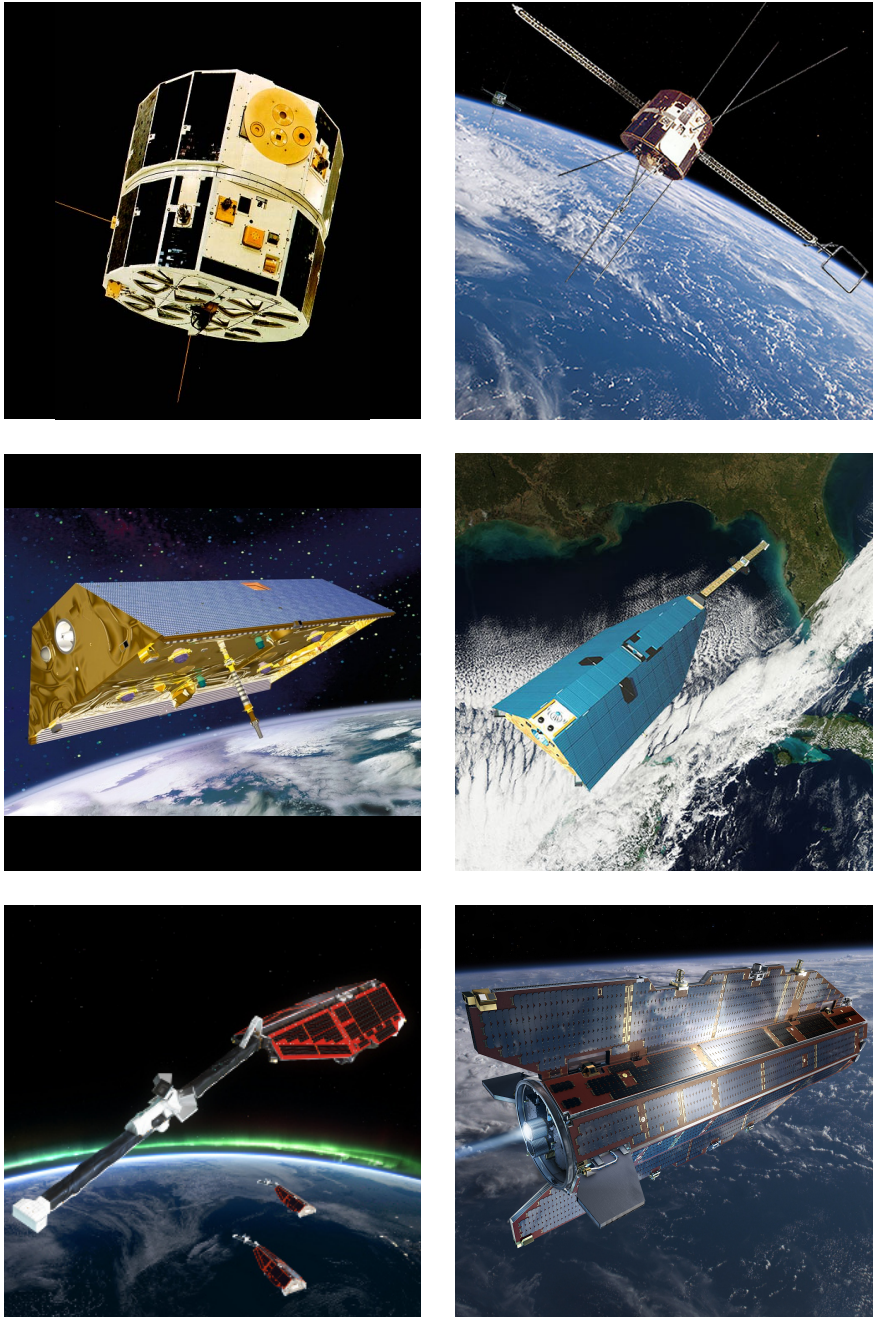


Figure 1.2: Artist impressions of several satellites used for atmospheric research. From left to right, from top to bottom: Atmosphere Explorer C (NASA), Dynamics Explorer 2 (NASA), GRACE (NASA,DLR), CHAMP (GFZ,DLR), Swarm (ESA), and GOCE (ESA). (Images courtesy of NASA/DLR/ESA.)

wheel satellites (*Pilinski et al., 2011*). For more modern accelerometer-carrying satellite missions, the only way to improve the thermospheric output is to improve the aerodynamic model. This is the subject of the next section.

### 1.3. SATELLITE AERODYNAMICS

At the ground level, the atmosphere is so thick that air particles collide with each other on a regular basis. Due to these particle collisions, information about obstacles can be propagated through the flow, which results in the well-known gradual flow of air around objects like buildings, cars, and aircraft. At satellite altitude however, the mean distance traveled before one air particle collides with another, the so called mean free path, is generally larger than the satellite itself. This flow condition is called free molecular flow. Rather than studying a flow of air, its aerodynamics are defined by the statistical behavior of single molecules.

Because we are dealing with single particles, the effect of an incoming particle is easily defined by a collision. The question then remains how this particle leaves the satellite wall. Much like light, particles may be reflected specularly (like light hitting a mirror) or re-emitted diffusively (like light hitting a white wall). The latter re-emission pattern is generally described by the Lambert cosine law. The three different aerodynamic models described hereafter have selected or mixed these two types of reflection in different ways.

First of all, the Maxwell model assumes that a fraction of the particles is reflected specularly, while the others are re-emitted diffusively (*Bird, 1994*). From observations on the Space Shuttle it was found that only 2–3% of particles are reflected specularly at 225 km altitude (*Gregory and Peters, 1987*). Combining a range of measurements, reflection was found to be almost purely diffusive at altitudes around 200 km (*Moe et al., 1993*).

Second, specular and diffuse reflection can also be mixed in a different way. Within the Cercignani–Lampis–Lord model, all reflected particles are assumed to be re-emitted quasi-specularly (*Cercignani and Lampis, 1971*). That is, all particles are reflected within a lobe around the specular direction. As this model is more complex than the previous, more assumptions are required considering e.g. the shape of the lobe to come to a usable aerodynamic model.

Finally, the few percent of specular reflection may be ignored, and a fully diffuse reflection can be assumed. Within this model however, a distinction can be made based on the level to which atmospheric particles accommodate their temperature to the satellite wall temperature before being re-emitted. Atmospheric particles generally have a significantly higher temperature than satellites. Combined with their high impact velocity, their total kinetic temperature can exceed the temperature of the satellite wall by several orders of magnitude. The level up to which the atmospheric particles cool down to this temperature, defined by the energy accommodation coefficient, is therefore an important parameter. This gives rise to the model of Diffuse Reflection with Incomplete Accommodation (DRIA). Different studies have found different values for the accommodation coefficient, depending on the orbit altitude, orbit eccentricity, and solar flux (*Agrawal and Prabhu, 2008; Pilinski et al., 2010, e.g.*). It has proven to be difficult to match horizontal wind measurements derived using a high accommodation value of

0.93 with ground-based observations (*Dhadly et al., 2017, 2018*).

Irrespective of the model selected, there are two main ways to implement the aerodynamic model in computer code. The first is the analytic panel model (*Sentman, 1961*). In this model, the spacecraft geometry is defined by a set of standard shapes, such as spheres, cylinders, and flat panels. Each panel has an area, orientation, and (preferably) position, from which the average force and torque produced by incoming flow on the panel can immediately be obtained analytically. The benefit of this analytic description is that it is fast to compute, and that the aerodynamic acceleration can be solved directly for the density and wind. The model does however often not take into account shadowing effects, or the possibility of a reflected particle hitting another part of the spacecraft. To include such complex interactions, which may have a significant impact on the aerodynamic properties of complex satellite geometries, a Direct Simulation Monte Carlo (DSMC) is often used (*Bird, 1994*). This method allows for complex geometries to be defined, after which the spacecraft is digitally bombarded by a large amount of randomly spatially distributed particles. The impact of these particles on the geometry combined with their statistical reflection pattern provides a measure for the force and torque on the body. Repeating this process for a range of flow incidence angles results in a complete aerodynamic model in the form of a data table. While shadowing and multiple-reflection effects are included in these models, their nonlinear nature introduces the need for iterative solvers to obtain the thermospheric density and wind from aerodynamic accelerations. Throughout this thesis, DSMC results from either the AN-GARA (*Fritsche and Klinkrad, 2004*) (in chapter 2) or the SPARTA software (*Gallis et al., 2014*) have been used.

## 1.4. THE GOCE MISSION

The Gravity field and steady-state Ocean Circulation Explorer (GOCE) satellite, sometimes referred to as the ‘Space-Ferrari’ because of its aerodynamic shape, was launched on 17 March 2009 as the first core Earth Explorer mission of the European Space Agency (ESA). Its purpose was to map the static part of the Earth’s gravity field at high spatial resolution (*Floberghagen et al., 2011*).

A variety of scientific and housekeeping instruments was required to successfully perform this mission, most of which are depicted in the cutaway in Figure 1.3. The primary scientific instrument was the Electrostatic Gravity Gradiometer (EGG): a construction of six three-axis accelerometers, evenly spaced along the satellites principle axes around the central point. While each accelerometer by itself measured a combination of several dynamic effects, taking different combinations of the set of accelerometer readings, either gravity gradients, non-gravitational linear accelerations, or non-gravitational angular accelerations could be isolated. To provide the accelerometers with a quiet measurement environment, and to prevent orbit decay due to drag, GOCE was fitted with a Xenon fueled, solar-powered ion engine (and a second, redundant one, obscured behind the first in Figure 1.3). To provide an accurate reference for the gravity measurements, the orbit was determined by satellite-to-satellite tracking (using the GPS network) and the attitude was measured by star trackers. The attitude was controlled with three magnetic torquers (i.e. electromagnetic coils) that could be activated to align the body with respect to the geomagnetic field. They are visible in Figure 1.3 as three perpendicular

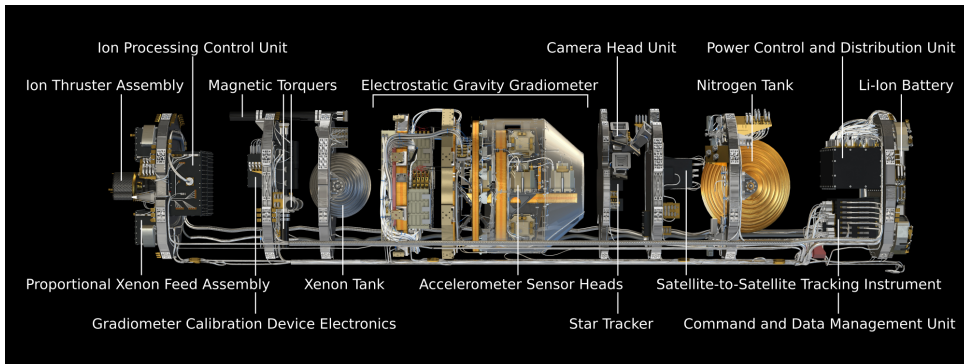


Figure 1.3: Top view of the GOCE instrumentation as it was positioned in the satellite body. The direction of flight is from left to right. (Image courtesy of ESA/AOES Medialab.)

black rods: one coming out of the page, one vertically to its left, and one horizontally at the top.

The orbit design was instrumental to GOCE's mission success. The constant low altitude of approximately 260 km was required to obtain a sufficiently small global spatial resolution, but immediately sparked the need for an ion engine to overcome aerodynamic drag. Due to the high power demand of the engine, a nearly continuous input of solar power was required. Therefore GOCE was injected into a near-Sun-synchronous dusk-dawn orbit at  $96.7^\circ$  inclination. Due to the near-polar orbit, near-global coverage was obtained.

The satellite geometry consisted of a  $5 \times 1.1 \text{ m} \times \text{m}$  cylinder with octagonal cross-section, with two 1 m wide wings spanning the top and bottom (see Figure 1.2). At the back of the cylinder, two smaller wings were attached on the left and right of the body. Because of the sun-synchronous orbit, the left side of the body and wings was covered in solar cells, whereas the other contained a radiator. The wings were designed such that GOCE was aerodynamically stable.

Because GOCE was not initially intended for atmospheric research, several limitations of the mission design can be identified. Due to the specific orbit geometry, all measurements taken by GOCE are limited in local time (ascend between 18:22 and 19:52, descend between 06:22 and 7:52) and altitude (continuous operation at 225–295 km). On top of that, the mission duration was limited to four years (including a two year extension), only one third of a solar cycle. Most of the mission took place during a solar minimum, followed by the particularly low solar maximum of 2013. Despite these limitations, a large amount of unique thermospheric density and horizontal wind data was already obtained from the linear accelerations of the GOCE satellite ([Doornbos, 2016](#)).

## 1.5. RESEARCH GOAL

Improvements to the aerodynamic model of satellites and the thermospheric data derived from satellite accelerations go hand in hand. On the one hand, a more correct aerodynamic model will improve the thermospheric data, on the other hand, a more

consistent thermospheric data set may imply that the aerodynamic model has improved. The simultaneous, high-accuracy observation of linear and angular accelerations by the GOCE satellite presents a unique opportunity to quantify this consistency of thermospheric data. Therefore the goal of this thesis is set as follows.

The goal of this thesis is to improve our estimates of aerodynamic parameters and assess the quality of accelerometer-derived thermospheric wind data, by adding the angular accelerations of the GOCE satellite as a source of wind data, and comparing these data to those derived from linear accelerations.

To reach this goal in a structured manner, a set of research questions has been formulated. For each question, reference is made to the chapter in which the answer may be found.

First and foremost, the angular accelerations of the GOCE satellite need to be analyzed, and the aerodynamic signal has to be extracted. This amounts to answering the questions:

1. Which torques provide a significant contribution to the total torque on a medium-size LEO satellite like GOCE?
2. With what level of accuracy can the total torque on such a LEO satellite be modeled, and what are the main sources of uncertainty?

These questions form the basis for chapter 2, in which a set of torque models is presented. These models include solar radiation pressure, gravity gradient, thruster misalignment, passive and active magnetic, and aerodynamic torque. The total model is compared to the measurements of GOCE, leading to an estimate for the accuracy of some of the individual models, as well as for the modeled torque as a whole. In chapter 5, question 1 is revisited when an electric dipole is estimated to improve the consistency of force- and torque-derived wind.

Second, the thermospheric density and wind should be derived, such that the aerodynamic torque they cause explains the unmodeled torque residual. This model output can then replace the initial aerodynamic model used before, such that the entire measured torque signal can be explained. If all models are correct, these density and wind data should be equal to those data derived from the forces acting on GOCE. Therefore, the following questions are added.

3. How can horizontal and vertical wind be obtained from an arbitrary combination of force and torque residuals?
4. With what level of accuracy can the thermospheric horizontal and vertical wind be obtained from torques, as compared to forces?

Both these questions are answered in chapter 3 of this thesis. The first question results in an iterative algorithm that derives both the horizontal and vertical cross-wind component from three or more residual force or torque components. Some force and torque components are found to be linearly dependent up to a large extent; in the case of GOCE,

the roll component is not sufficiently affected by aerodynamic torque to provide a valuable input to the algorithm. The force-derived and torque-derived wind are compared, and the sensitivity of both data sets to a large amount of measurement errors and model parameters is investigated.

Third, since vertical wind data are rare and this is the first time that this wind component was derived from GOCE accelerations, the force-derived vertical wind requires validation against other data sources. To compare the global set of data, a comparison with other satellite missions is the obvious choice, leading to the question:

5. To what level of accuracy can vertical wind obtained from the GOCE accelerations be validated against satellite mass spectrometry-derived data?

In chapter 4, the force-derived vertical wind data is therefore compared to data from Atmosphere Explorers C and E, and (primarily) Dynamics Explorer 2. Since vertical wind in the thermosphere mostly takes the form of short-lived, small-scale wavelets, the wind data is first converted to an activity measure. The dependence of this activity on geomagnetic activity, as well as on latitude, local time, and the day of year, is investigated in detail.

Finally, when the accuracy of both the force- and torque-derived wind is known, and its sensitivity to model parameters has been evaluated, an attempt can be made to improve the aerodynamic model by optimizing the consistency between the two data sets. This amounts to answering the question:

6. How can simultaneous observation of linear and angular satellite dynamics aid to improve the aerodynamic model and the thermospheric data?

In chapter 5, the effect of changing the aerodynamic model on the wind data, as well as on several estimated parameters is evaluated. The combination of the achieved consistency between force- and torque-derived wind on the one hand, and the sensitivity of this consistency to changes in the aerodynamic model on the other, results in an answer to this question. Although this thesis focuses entirely on the GOCE satellite, some conclusions and recommendations can be drawn for LEO satellites in general.

Chapters 2 and 3 have been published as papers in the peer-reviewed journal *Advances in Space Research*, and chapter 4 in the peer-reviewed *Journal of Geophysical Research: Space Physics*. Chapter 5 is structured as a paper, for consistency. To improve the readability of this dissertation as a whole, references to past or future research have been changed throughout this book to references to the respective chapters. The answers to all research questions are collected in chapter 6. On top of that, recommendations are made for future research into both satellite aerodynamics and thermosphere dynamics.



# 2

## TORQUE MODEL VERIFICATION FOR THE GOCE SATELLITE

**T. VISSER, E. DOORNBOS, C. DE VISSER, P. VISSER, and  
B. FRITSCHÉ**

*The modeling of torques acting on satellites is essential for the design of satellite attitude control systems. The GOCE satellite, equipped with accurate accelerometers, star trackers and GPS receivers, presents an opportunity to validate these models. Although the forces on GOCE and other accelerometer-carrying missions have been extensively analyzed in the past, a similar analysis has not yet been made for the torques.*

*In this chapter, we present a set of torque models for the GOCE satellite. It consists of six main parts: 1) magnetic torquer actuators, 2) aerodynamic torque, 3) gravity gradient torque, 4) solar radiation pressure torque, 5) thruster torque, and 6) passive magnetic torque. The magnetic properties of the payload are approximated using a parametrization, of which the parameters are estimated from the observation data.*

*Based on data recorded during selected spacecraft events, the model for the control torques can be validated and error sources are identified in the other models. The models perform best in roll and pitch, where the standard deviation is reduced to 15.2% and 2.1% of the standard deviation of the control torque around those axes respectively. In yaw the standard deviation is significantly larger at 30.5%. The remaining differences between models and observations show magnetic signatures due to electric currents and signatures of aerodynamic model errors. The latter correspond well with an increase in thermosphere density and wind speed with increased geomagnetic activity. The pitch torque is found to be a potential source of vertical wind data.*

---

This chapter has been published as a paper in *Advances in Space Research* **62**, 5 (2018) ([Visser et al., 2018](#)).

## 2.1. INTRODUCTION

The goal of this chapter is to test the validity of torque models for the Gravity field and steady-state Ocean Circulation Explorer (GOCE) satellite, by comparing the individually modeled torques with total torques obtained from the angular accelerations that were measured on the satellite. The models that are investigated represent the aerodynamic, radiation pressure, gravity gradient, magnetic and actuator torques. Second, we demonstrate that models and measurements of torques on GOCE are important for improving our understanding of satellite aerodynamics and investigating thermosphere density and wind. The further pursuit of these goals will be the subject of the other chapters of this dissertation.

GOCE was a unique satellite. Its highly accurate measurements and low orbit are especially suitable for analyses of aerodynamic forces and torques. However, this does not mean that the results of this chapter are only applicable to GOCE. In fact, in our conclusions and recommendations, we will discuss the extent to which the models can be applied to both existing satellite missions and concepts for future missions in low Earth orbit, and how data from such other satellites could be applied for the same goals.

This work is motivated by the need to resolve outstanding issues in the field of satellite aerodynamics and related discrepancies between datasets and models of thermosphere dynamics. Since the early days of spaceflight, analyses of accelerations on satellites in low Earth orbit have been used to derive observation data of the thermosphere (e.g. [King-Hele, 2005](#)). With the near-continuous operation of space-based accelerometers in polar low Earth orbits, provided by CHAMP, GRACE, GOCE and Swarm, this domain has received a strong boost, leading to a significant increase in publications on thermosphere dynamics and improvements of thermosphere models (see e.g. [Doornbos \(2011\)](#); [Emmert \(2015\)](#); [Visser et al. \(2013\)](#) and references therein). In all recent studies using these satellites, only linear acceleration measurements have been used, even though the star camera and accelerometer measurements also contain information on angular accelerations. The main argument for not using these is most likely that the angular acceleration measurements are more contaminated by non-aerodynamics signals than their linear counterparts, such as magnetic perturbations and control activities.

The most important limitations in the thermosphere datasets resulting from these missions are due to the use of approximative satellite geometry models and assumptions made in the gas-surface interaction models used to describe the satellite aerodynamic interaction. This is a fairly complex multi-disciplinary topic, and these limitations might not be immediately obvious to users of the affected data. The most obvious indications of such limitations might be found in the form of scale differences between the density data sets of different missions and models ([Doornbos, 2011](#), section 5.3), and discrepancies between the accelerometer-derived and ground-based wind measurements, especially at high latitudes ([Dhadly et al., 2017](#); [Kärräng, 2015](#)). It is likely that there are also more subtle consequences. It is certain that such problems in the models mix with any data-related problems and thereby limit our ability to disentangle, model and remove them.

Among the previous work done to increase the fidelity of the accelerometer data processing is the application of non-hyperthermal satellite aerodynamics ([Doornbos, 2011](#); [Koppenwallner, 2008](#); [Sutton, 2009](#)), the development of an attitude-independent algo-

rithm that properly takes into account lift and wind (Doornbos *et al.*, 2010), empirical modeling of gas-surface interaction parameters (Pilinski *et al.*, 2013; Walker *et al.*, 2014a) and development of high-fidelity satellite geometry models (Mehta *et al.*, 2014, 2017). However, due to the sparsity of data, so far these efforts have undergone only limited validation. So far, these data processing developments have not been applied to all modern accelerometer satellites in the same way, making it difficult to further investigate inconsistencies. Finally, the empirical gas-surface parameter modeling efforts are based on old and sparse data on aerodynamic forces and torques, on so-called paddlewheel satellites, that were flown in the late 1960s and early 1970s (Pilinski *et al.*, 2011). Due to the obscurity of the paddlewheel data and associated mission documentation, it is difficult to assess their accuracy and impossible to replicate these studies from scratch.

The high cadence and accurate angular acceleration measurements by GOCE are a readily available additional data source for this line of investigation. Along with house-keeping data that enables accurate torque modeling, it is our intention that this modern dataset will augment or replace the paddlewheel satellite analyses, to provide new insights on satellite aerodynamics and thermosphere variability.

The data processing and modeling work presented here has value in the engineering as well as the scientific domain. Models of torques on satellites (e.g. Wertz, 1978; Wie, 2008) are crucial for the design and scaling of spacecraft attitude control subsystems, and have therefore been tested extensively by indirect methods, i.e. by assessing whether these systems are capable of maintaining the desired attitude pointing and maintaining desired angular rates. However, a direct and precise comparison of modeled torques and observed angular accelerations has, to the best of our knowledge, not been published before.

The chapter describes how the torque models from the engineering literature cited above have been adapted for the GOCE satellite. To validate the torque models, we have first calculated a *measured torque* from the measured angular rate, angular acceleration, and satellite inertia matrix. In the next step, all models have been evaluated and summed to come to a total of the directly modeled torque. Because the magnetic properties of the satellite payload are not known to us, an extra set of magnetic dipoles was estimated for each day from the residual torque. A linear fit was made to the daily estimates, from which the dipole at each time instance was obtained. The torque caused by these dipoles was added to the total modeled torque. To validate the complete set of models the two results were compared and their differences were examined for signatures that point to specific model errors. The control torque was individually validated by investigating the model error over an episode of increased control activity.

The result of this endeavor is a complete, validated set of torque models for the GOCE satellite. This result is generalized to other low Earth orbiting satellites by identifying the magnitude and source of the main model errors. Most notably, the pitch and especially the yaw residual show significant signatures that point to aerodynamic torque modeling errors.

The chapter is structured as follows. First in section 2.2, the data sources are presented, as well as the Earth models used and the reference frames in which these data are defined. Then in section 2.3, the model definitions are provided for each source of torque. The procedure of estimating payload dipoles is described in section 2.3.6. In sec-

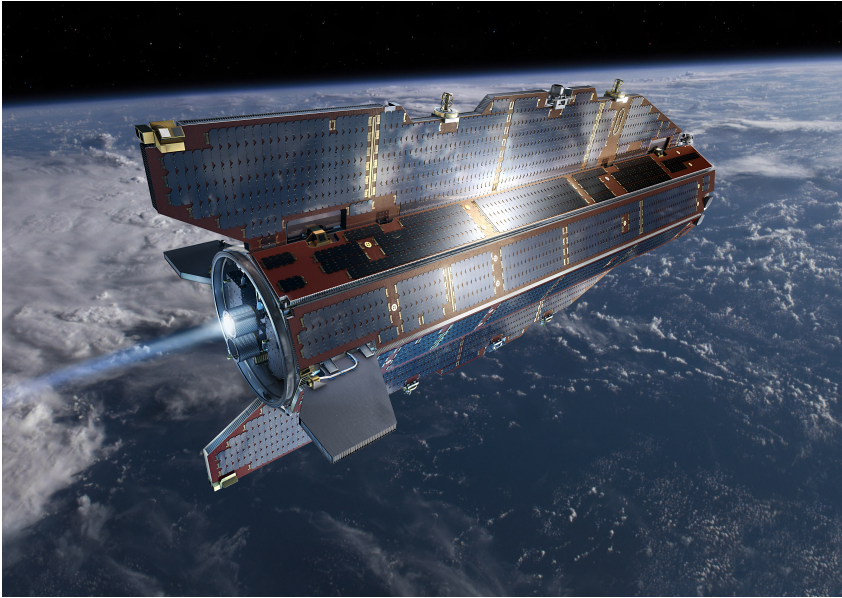


Figure 2.1: Artist impression of the GOCE satellite in orbit. Courtesy of ESA/AOES Medialab.

tion 2.4, the validation of each individual contribution to the total torque is discussed. Finally the conclusions of this work are provided in section 2.5, where the possibility of extracting aerodynamic and thermospheric information from the torque residuals is further discussed, as well as implications for other existing missions and future mission concepts.

## 2.2. THE GOCE MISSION AND DATASETS

The GOCE satellite (Gravity field and steady-state Ocean Circulation Explorer) (*Drinkwater et al., 2003; Fehring et al., 2008; Floberghagen et al., 2011*) was launched on 17 March 2009 for the purpose of mapping the static part of the Earth's gravity field at high spatial resolution. This improved gravity field mapping capability has many application areas, including the investigation of ocean circulation patterns. As its main instruments, the satellite carried GPS receivers for satellite-to-satellite tracking and a gradiometer to measure gravity gradients. An ion engine, driven by solar power and Xenon fuel, was used to provide a quiet environment for the accelerometers and counteract orbit decay due to drag to maintain a very low mean altitude (below 270 km).

A set of star trackers was used for attitude determination. In order to minimize disturbances of the gradiometer readings, attitude control in science mode was implemented using three magnetic torquer actuators only. Four fins on the top, bottom, and back of the satellite were designed for additional aerodynamic stability (see Figure 2.1). Three 3D fluxgate magnetometers were available as sensors in the AOCS subsystem, in addition to the star trackers.

A near-polar, near sun-synchronous dusk-dawn orbit with  $96.7^\circ$  inclination was se-

lected to maximize available solar power and achieve near-global coverage. After depletion of the Xenon fuel on October 22, 2013, the orbit underwent natural decay, after which the satellite broke up during re-entry over the South-Atlantic on November 11, after more than 4.5 years of successful operations (*GOCE Flight Control Team (HSO-OEG), 2014*).

The Electrostatic Gravity Gradiometer (EGG) instrument on-board GOCE consisted of six individual accelerometers that each measured the linear accelerations in all three principle body-fixed axis directions. The gravity gradients, as well as the linear non-gravitational accelerations and angular accelerations can be derived by taking specific combinations of these individual measurements (*Rummel et al., 2011*).

In preparation for the creation of the torque model, all relevant data and documentation were acquired. This included finding information on the positioning and magnetic properties of the satellite parts in the mission documentation. These data were then implemented in a custom made Matlab toolbox in which the measured and modeled torques were calculated. As the magnetic properties of the payloads were not available, additional hard magnetic and soft magnetic dipoles were estimated, reducing the residual, unmodeled torque in a weighted least squares sense. This was done for the complete science phase of the mission. Periods for which the data are deemed of insufficient quality, as reported by ESA, were excluded.

For each model an attempt was made to isolate a short part of the mission in which that torque was dominant, changing abruptly, or known a priori. This approach has led to the validation of most parts of the individual models. Finally the sum of the torque model output was compared to the measured torque over the entire mission, resulting in the validation of the model as a whole.

In the presented analysis, five different reference frames are used. They are listed in Table 2.1, along with the abbreviations used in the remainder of this chapter. All analyses are performed in the body (B) frame. The orbital (O) frame is used only to define Euler attitude angles, since the attitude control was designed to keep the satellite body axes aligned with respect to the orbital velocity and orbital angular momentum vector directions. The other frame definitions in Table 2.1 are used to convert measurements and model outputs to the B-frame.

For the analysis of the torques acting on GOCE, both scientific data products and housekeeping data are required. A list of the data used is provided in Table 2.2. Note that the reference frame symbols refer to Table 2.1. Of the EGG\_NOM and SST\_PSO products we use version 5.06. A recent reprocessing effort by *Siemes (2018)* suggests that the calibration of these data may be improved in a future release.

The Earth models used in the analysis are listed in Table 2.3. The International Geomagnetic Reference Field (IGRF) is only used to calibrate the magnetometer readings, whereas the other models are used in torque calculations directly. NRLMSISE-00 is only used to calculate the local temperature and the number density of thermospheric constituents. At GOCE's altitude the main contributions to drag will be due to oxygen and nitrogen, which have similar molecular mass. Errors in the atmospheric composition will therefore have a limited effect on the aerodynamic coefficients (see Figure 3.9 in *Doornbos (2011)*). The number densities are scaled with the ratio of density from NRLMSISE-00 to the density estimated from the linear accelerations of GOCE (*Doornbos, 2016*). The

Table 2.1: Reference frame definitions, all right-handed.

| Frame       | Origin                        | $x$                        | $y$              | $z$                   |
|-------------|-------------------------------|----------------------------|------------------|-----------------------|
| Inertial    | Earth's center of mass        | Mean equinox               | (-)              | Earth's rotation axis |
| Earth fixed | Earth's center of mass        | Greenwich meridian         | (-)              | Earth's rotation axis |
| Spacecraft  | Reference point on back plate | Forward (symmetry axis)    | (-)              | Main fin (nadir)      |
| Body        | Satellite center of mass      | Forward (symmetry axis)    | (-)              | Main fin (nadir)      |
| Orbital     | Satellite center of mass      | Velocity (Earth's surface) | Angular momentum | (-)                   |
| Local NED   | Satellite center of mass      | North                      | East             | Down                  |

Table 2.2.: Overview of used science (above) and housekeeping data (below the line).

| Data                           | Product                             | Field                                | Unit                 | Rate [Hz] | Frame |
|--------------------------------|-------------------------------------|--------------------------------------|----------------------|-----------|-------|
| Orbit and velocity             | SST_PSO                             | PRD                                  | km, dm/s             | 1/10      | E     |
| Earth's orientation quaternion | SST_PSO                             | PRM                                  | (-)                  | 1         | E/I   |
| Satellite attitude quaternion  | EGG_NOM                             | IAQ                                  | (-)                  | 1         | B/I   |
| Angular rate                   | EGG_NOM                             | GAR                                  | rad/s                | 1         | B     |
| Angular acceleration           | EGG_NOM                             | CGA                                  | rad/s <sup>2</sup>   | 1         | B     |
| Magnetometer                   | AUX_NOM                             | MGM[1/2/3]_[X/Y/Z]_out <sup>a</sup>  | nT                   | 1/16      | S     |
| Magnetic torquer current       | MTR_POFF <sup>b</sup>               | (-)                                  | A                    | 1         | S     |
| Ion engine current             | AUX_NOM                             | MAGNET_CURRENT_8                     | mA                   | 1/8       | (-)   |
| Ion engine commanded thrust    | AUX_NOM                             | THRUST_DEMAND_8                      | $\mu$ N              | 1/8       | S     |
| Latch valve setting            | AUX_NOM                             | GCODE_[A/B]_LV[1/2/3/4] <sup>a</sup> | (-)                  | 1/16      | (-)   |
| Inertia, center of mass        | Mass property file <sup>c</sup>     | (-)                                  | kgm <sup>2</sup> , m | weekly    | (-)   |
| Solar panel currents           | Personal communication <sup>b</sup> | PCU[1/.../6]_INPUT_CUR <sup>a</sup>  | A                    | 1/16      | (-)   |

<sup>a</sup> Different field names are indicated by options in square brackets.

<sup>b</sup> These data was provided by ESA separately upon request, as the related fields are not available in AUX\_NOM or incorrectly converted from binary data.

<sup>c</sup> Available at [earth.esa.int/goce](http://earth.esa.int/goce).

latter data is also the source for horizontal wind. Vertical wind is not modeled.

Table 2.3: The models used in the data analysis and calibration.

| Input                  | Model                                 | Output                        |
|------------------------|---------------------------------------|-------------------------------|
| Orbit                  | IGRF                                  | Magnetic field                |
| Orbit, time, ap, F10.7 | NRLMSISE-00                           | Number densities, temperature |
| Time                   | GOCE+ Thermospheric Data <sup>a</sup> | Neutral density, cross-wind   |

<sup>a</sup>Thermospheric density and cross-wind derived from GOCE linear accelerations by [Doornbos \(2016\)](#).

For the analysis of the data the argument of latitude is used to describe the progress of the satellite in its orbit. This parameter runs from 0 to 360 degrees for each orbit, with the origin defined at the ascending node. For GOCE, which was in a near-circular, near-polar orbit, this parameter is between 0 and 180 degrees over the Northern hemisphere, and close to 90 and 270 degrees over the North and South pole respectively.

All instrument data has been (re)sampled using linear interpolation at 0.1 Hz before further processing. Only the magnetometer data is provided at a lower rate than this. As the magnetic field varies smoothly over the orbit, the upsampling by interpolation of this data will not invalidate the presented results.

## 2.3. TORQUE MODELS

The main result of this work is a toolbox containing models for each significant torque acting on the GOCE satellite. The total modeled torque (indicated with a bar) can be described as a sum of individual contributions

$$\bar{\mathbf{T}} = \bar{\mathbf{T}}_M + \bar{\mathbf{T}}_A + \bar{\mathbf{T}}_G + \bar{\mathbf{T}}_S + \bar{\mathbf{T}}_I, \quad (2.1)$$

where  $\bar{\mathbf{T}}_M = \bar{\mathbf{T}}_T + \bar{\mathbf{T}}_{D,I} + \bar{\mathbf{T}}_D$  is the total magnetic torque, caused by the magnetic control torquers ( $\bar{\mathbf{T}}_T$ ), the ion thruster's main magnet ( $\bar{\mathbf{T}}_{D,I}$ ), and other magnetic parts of the satellite bus and payload ( $\bar{\mathbf{T}}_D$ ). In this chapter the latter is split into a component known a-priori that is mostly due to the spacecraft bus ( $\bar{\mathbf{T}}_{D,B}$ ), and a component that had to be estimated and stems primarily from the payload ( $\bar{\mathbf{T}}_{D,P}$ ).  $\bar{\mathbf{T}}_A$  is the aerodynamic torque,  $\bar{\mathbf{T}}_G$  the gravity gradient torque,  $\bar{\mathbf{T}}_S$  signifies the torque caused by solar radiation pressure and Earth albedo, and finally  $\bar{\mathbf{T}}_I$  is the torque caused by misalignment of the ion thruster with respect to the satellite center of mass. In this section, each of these models is described. In relevant cases the sensitivity of the models to existing uncertainties is also analyzed. All modeled torques are plotted in [Figure 2.2](#) for a representative orbit on May 28, 2011, to provide an overview of their individual magnitude and trend.

### 2.3.1. MAGNETIC CONTROL

To control the attitude, GOCE had three magnetic torquers, nominally aligned with the body principal axes. To accommodate the torquers, magnetometers were installed to measure the Earth magnetic field.

A magnetic torquer induces a torque by creating a magnetic dipole  $\boldsymbol{\mu}_T$ . The dipole has a natural tendency to orient itself along the local magnetic field lines, which are assumed to be equal to the local Earth magnetic field lines  $\mathbf{B}_E$ . This results in a torque

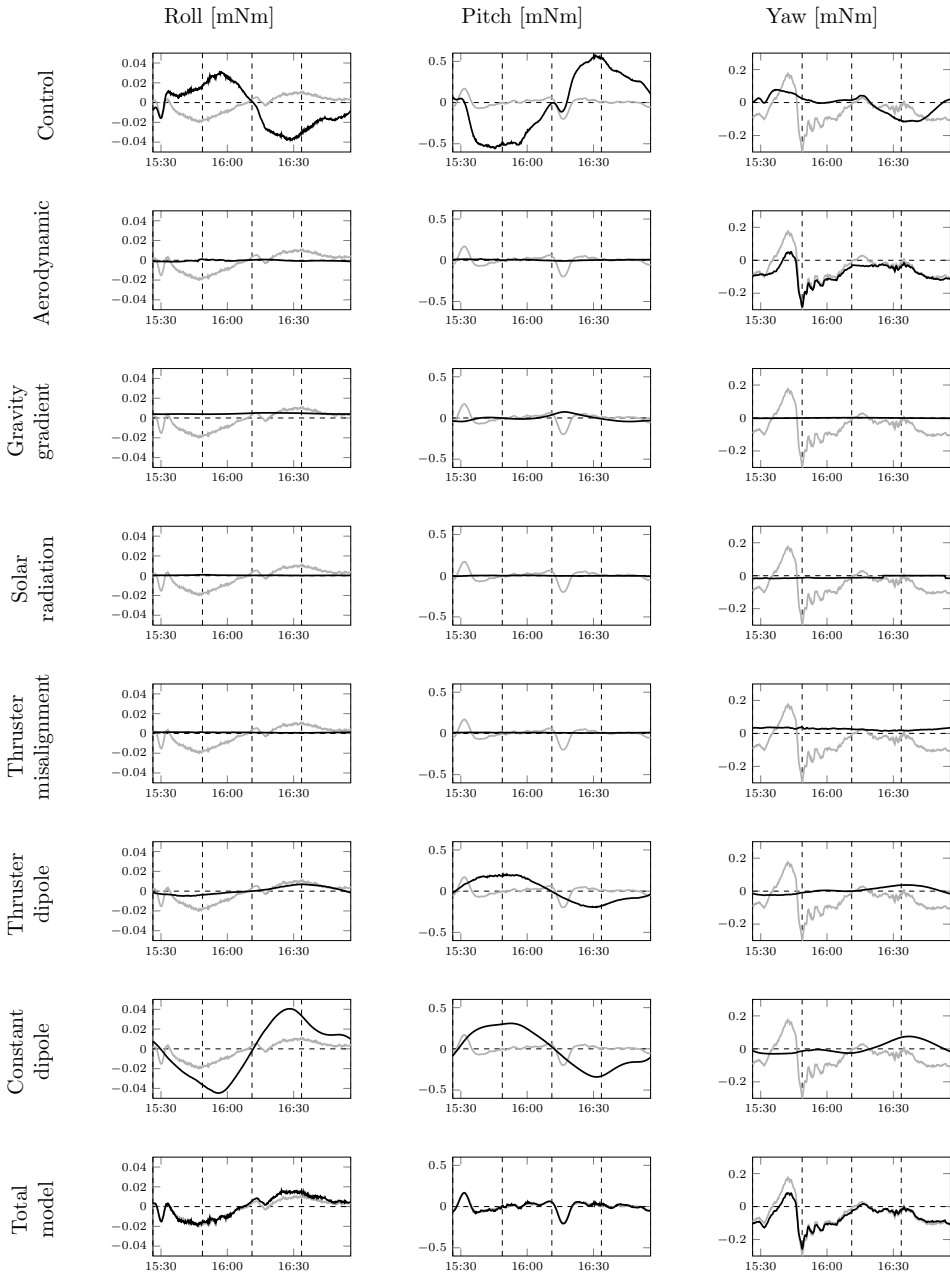


Figure 2.2: The output from all individual models (black) for a representative orbit on May 28, 2011, compared to the total measured torque (gray). The plot starts and ends at the ascending nodes, passing through the Northernmost point, descending node, and Southernmost point of the orbit, in that order, indicated with dashed vertical lines.

$$\vec{T}_T = \boldsymbol{\mu}_T \times \mathbf{B}_E. \quad (2.2)$$

The dipole is directly related to the current running through the device. This dependence can be modeled as an adaptive cubic relation (Cometto, 2007).

Because the magnetometers of GOCE were situated inside the satellite body, their readings require thorough calibration. During pre-launch testing it was found that the main contributors to measurement errors were a constant internal dipole and the magnetic torquer activation (Kolkmeier et al., 2008). Therefore a calibration is performed that accounts for both these elements, alongside a bias  $\mathbf{B}_B$  and scale factor  $S_E$ . That is, we assume the magnetometer readings  $\mathbf{B}_M$  are given by

$$\mathbf{B}_M = S_E \mathbf{B}_E + (A_C \boldsymbol{\mu}_C + \mathbf{B}_B) + A_T \boldsymbol{\mu}_T, \quad (2.3)$$

where  $A_C \boldsymbol{\mu}_C$  and  $A_T \boldsymbol{\mu}_T$  are the magnetic field due to a constant on-board dipole and the magnetic torquer activation, respectively. Note that Equation (2.3) is linear in the torquer dipole  $\boldsymbol{\mu}_T$ , as is the magnetic field it causes. Instead of modeling the magnetic field caused by the torquers at the magnetometer location, this relation is estimated and collected in the matrix  $A_T$ . Note also that the constant terms due to the constant dipole  $\boldsymbol{\mu}_C$  and the magnetometer bias (in brackets in Equation (2.3)) can not be estimated separately based on in-orbit measurements.

By performing a least squares fit in which  $\mathbf{B}_E$  is replaced by the IGRF model output, the three magnetometers are calibrated individually. The parameters are estimated for each day of the mission. A linear fit is estimated that describes every parameter as a linear drift in time from a starting value. On four occasions during the mission the back-up GPS receiver is switched on, resulting in a different on-board dipole. As this directly affects the magnetometer bias, these episodes are treated separately from the rest of the mission for that calibration parameter. The switches are also observed in some of the scale factors. These jumps in scale factors are however considered too small relative to the nominal scale factor variation to be taken into account. The result of the calibration procedure is shown in Figure 2.3 for one of the magnetometers. The magnetic torquer factors show a yearly oscillation around the linear trend. As the amplitude of this error increases over the mission, it is likely linked to the larger torquer activation later in the mission. As the magnetic disturbance is linearly related to the magnetic dipole of the torquers, this non-linearity is considered a calibration error.

The calibration matrices for each magnetometer are obtained from the linear relations. Then the calibrated signals from each magnetometer are combined into one measurement in each direction by a weighted sum, with the inverse of the remaining root mean square error (RMSE, taken over one full month) between the signal and the IGRF as weights.

In the plots of the control torque  $\vec{T}_T$  in Figure 2.2 we can distinguish what seem to be periods of strong attitude correction in pitch. These consist of smooth peaks just after passing the ascending and descending nodes, at the start and halfway through the plotted time window respectively. It is unclear whether these maneuvers are caused by external disturbances or the internal control algorithm.

An uncertainty in the range from 0% to +10% is reported for the maximum dipole of each magnetic torquer (Kolkmeier et al., 2008). As the residual shows some similarity

to the control torque throughout the mission, we have assumed this uncertainty holds throughout the linear control range. This scale factor is estimated along with the payload dipoles, as described in section 2.3.6.

### 2.3.2. AERODYNAMICS

At the low altitude of GOCE, aerodynamic effects cause the main linear disturbance, especially as drag in the direction of flight. In terms of angular disturbances, the aerodynamic effects are especially clear in yaw, where they form the main cause of torque. This is partly due to the loose control in this direction, allowing GOCE to behave like a weather vane.

To model the aerodynamic torque the standard model

$$\bar{\mathbf{T}}_A = (\mathbf{C}_{M,A} l_{ref} + (\mathbf{r}_{ref} - \mathbf{r}_{com}) \times \mathbf{C}_{F,A}) \frac{1}{2} \rho |\mathbf{v}|^2 A_{ref} \quad (2.4)$$

is used, where  $(\mathbf{r}_{ref} - \mathbf{r}_{com})$  is the arm from the reference point in the aerodynamic model to the center of mass of the satellite,  $\rho$  is the atmospheric neutral density, and  $\mathbf{v}$  is the total flow velocity. The moment coefficients  $\mathbf{C}_{M,A} = (C_l, C_m, C_n)^\top$  and force coefficients  $\mathbf{C}_{F,A} = (C_X, C_Y, C_Z)^\top$  are obtained from a Monte-Carlo simulation in the Analysis of Non-Gravitational Accelerations due to Radiation and Aerodynamics (ANGARA) software (*Fritsche and Klinkrad, 2004*). All coefficients are given as a function of angle of attack  $\alpha_A$ , angle of sideslip  $\beta_A$  and speed ratio  $S$  in a data table. This table is interpolated linearly. Because the speed ratio differs per atmospheric constituent, the contributions are interpolated individually and weighted with their respective density ratio (*Doornbos, 2011*). Reference area  $A_{ref}$  and length  $l_{ref}$  were set to one within the ANGARA software. ANGARA provides coefficients for incoming and for outgoing particles, which are combined using the square root of the ratio of wall temperature to atmospheric temperature.

The velocity of incoming particles  $\mathbf{v}$  not only scales the torque, but it also sets the parameters used to interpolate the ANGARA coefficients. It is assumed to consist of three parts, being the orbital velocity  $\mathbf{v}_O$ , the velocity due to co-rotation of the atmosphere with the Earth  $\mathbf{v}_C$ , and thermospheric wind velocities  $\mathbf{v}_W$ . In GPS measurements however, the velocity is measured with respect to the Earth's surface, providing  $\mathbf{v}_O + \mathbf{v}_C$  directly. As stated in section 2.2 the wind and density measurements stem from the linear accelerations of GOCE, whereas the number densities per constituent and the local temperature are found through NRLMSISE-00.

In Figure 2.2 the aerodynamic torque is plotted for one orbit. It is evident that the controller is more dominant in roll and pitch than it is in yaw. Low amplitude high frequency signals occurring near the pole crossings at 15:45 and 16:30, are observed in the control torque in roll and pitch, but in the aerodynamic torque in yaw. This implies that these signals are aerodynamic in nature, and are controlling the yaw axis, whereas they are canceled by the controller in the other directions of rotation.

Because of the change of the center of mass location due to fuel consumption, the offset between the interpolated center of mass and the ANGARA reference point needs to be taken into account. In total this causes a change in torque of less than 4%. Using the beginning-of-life or end-of-life values for  $\mathbf{r}_{com}$  results in a spread in torque of approximately 1%.

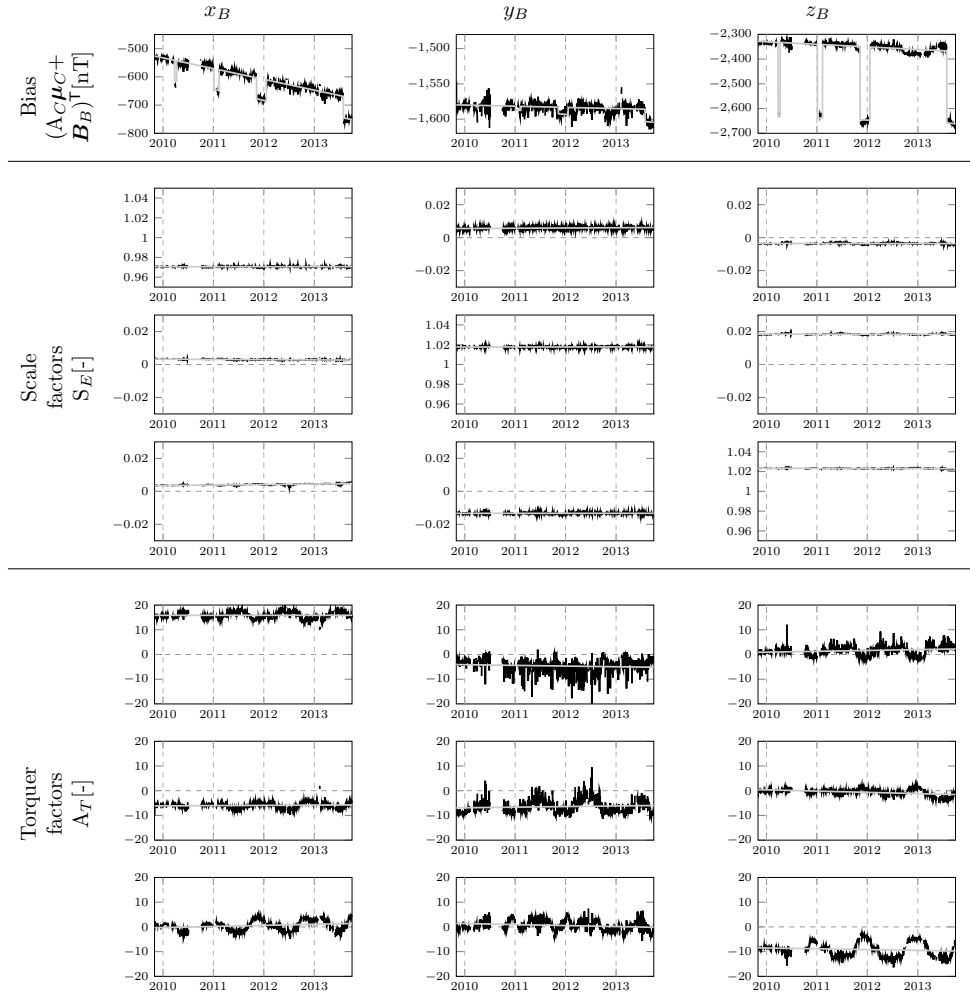


Figure 2.3: Daily magnetometer bias, scale factors, and magnetic torquer factors estimates (black) and the fitted linear trends (gray).

A more important uncertainty lies in the physical properties of the aerodynamic model. Currently we use a fully diffusive model with full energy accommodation. A more simple panel model provided by ThalesAlenia Space, which is described by *Dumontel (2010)*, is evaluated for different levels of accommodation in the range 0.8 to 1, to find that the aerodynamic yaw torque is insensitive to this change within 1%. In roll and pitch the torque coefficient reduces linearly with accommodation to 87% and 84% respectively for an accommodation coefficient of 0.8. The model is therefore deemed very sensitive to this parameter, which makes it an important aspect in explaining the residual in section 2.4. No specular aerodynamic model was investigated.

### 2.3.3. GRAVITY GRADIENT

A difference in gravitational pull at two ends of a satellite causes a torque. In general this gravity gradient torque works to rotate the satellite such, that the longest dimension becomes vertical. In the case of GOCE this is unwanted, as the longest dimension is supposed to point in the direction of flight to minimize drag.

A simple model for this torque, assuming a spherical Earth, is well known from the literature (e.g. *Wie, 2008*). Less well known and used are the extensions to this model due to zonal harmonics, as presented by *Roithmayr (1991)*. Adding only the  $J_2$  term to the basic (spherical) expression, we obtain

$$\begin{aligned} \bar{\mathbf{T}}_G = & \frac{3\mu}{r^3} \mathbf{u}_r \times \mathbf{J} \mathbf{u}_r + \\ & \frac{\mu J_2 R_E^2}{2r^5} \left( 30(\mathbf{u}_r \cdot \mathbf{u}_n)(\mathbf{u}_n \times \mathbf{J} \mathbf{u}_r + \mathbf{u}_r \times \mathbf{J} \mathbf{u}_n) + \right. \\ & \left. (15 - 105(\mathbf{u}_r \cdot \mathbf{u}_n)^2) \mathbf{u}_r \times \mathbf{J} \mathbf{u}_r + 6\mathbf{u}_n \times \mathbf{J} \mathbf{u}_n \right) \end{aligned} \quad (2.5)$$

where  $\mathbf{u}_r$  is the unit vector pointing from the satellite center of mass towards the Earth's center of mass and  $\mathbf{u}_n$  is the unit vector along the rotation axis of the Earth, both expressed in the body frame.  $\mathbf{J}$  is the inertia tensor,  $r$  the radial distance between GOCE and the Earth's center,  $\mu$  the Earth's gravitational parameter, and  $R_E$  is the Earth radius.

The modeled gravity gradient torque only plays a significant role in the roll and pitch direction, as can be concluded from Figure 2.2. In roll it causes an offset, in pitch it peaks at the occurrence of high Euler angles.

The  $J_2$ -term results in a significant contribution to the total torque. This is especially the case for the yaw axis, in which the extra term is approximately a factor 5 larger than the spherical term. The  $J_3$ -term (also available through *Roithmayr (1991)*) is at least two orders of magnitude smaller than the  $J_2$ -term, and therefore neglected. We assume that the same holds for tesseral and sectoral contributions.

### 2.3.4. SOLAR RADIATION

Although the solar radiation causes a significant disturbance force, the resulting torque on GOCE is very small. The dusk-dawn orbit results in a constant torque about the yaw axis.

The model for solar radiation pressure torques is similar in structure to the aerodynamic model of Equation (2.4), namely

$$\vec{T}_S = (C_{M,S} l_{ref} + (\mathbf{r}_{ref} - \mathbf{r}_{com}) \times \mathbf{C}_{F,S}) A_{ref} \frac{\Phi}{2c}, \quad (2.6)$$

where  $\Phi$  is the solar flux at the location of GOCE and  $c$  is the speed of light.  $C_{M,S}$  and  $C_{F,S}$  are the solar radiation coefficients for forces and torques respectively, again obtained from the ANGARA software. Contrary to the aerodynamic coefficients, they only depend on the incidence angles  $\alpha_S$  and  $\beta_S$  (defined in the same way as their aerodynamic counterparts). Again, the reference area and length are set equal to one. In the validation process the roll coefficient from ANGARA was found to be wrong, and was therefore replaced by a simpler panel model (see section 2.4.4). A simple model is implemented to detect and account for eclipses (Doornbos, 2011).

The Earth's infrared radiation and albedo are also taken into account, for the sake of completeness. In the model, adopted from Doornbos *et al.* (2009), the Earth surface is subdivided in one degree longitude by one degree latitude quadrilaterals. For all elements it is decided whether they are visible from GOCE and, for the albedo model, from the Sun. Then Lambert's law is applied to the incoming sunlight, the outgoing reflected sunlight, and the outgoing infrared radiation. The resulting fluxes are multiplied with the monthly-mean top-of-atmosphere all-sky albedo and longwave flux respectively, obtained from the CERES SYN1deg product (Edition 3A). The resulting torque is added to the direct solar radiation torque.

The model output is shown in Figure 2.2 for one orbit. Solar radiation mainly causes an offset in the yaw torque when GOCE is not in eclipse.

Varying the location of the center of mass over the range of possible values results in a range of torques differing by less than 4%. Even in the most extreme case no significant contribution to the total torque is thus to be expected.

### 2.3.5. ION THRUSTER

To compensate for drag, GOCE is equipped with an ion thruster. When the thrust does not point directly through the center of mass, it causes a torque. Therefore the thruster is pointed such that it aims in the center of mass range. Over the course of the mission the center of mass will shift due to fuel consumption, causing a slowly changing misalignment torque.

The model for the torque due to thruster misalignment, denoted by  $\vec{T}_I$ , is simply the cross product between the arm from the thruster position  $\mathbf{r}_T$  to the center of mass of the satellite  $\mathbf{r}_{com}$  and the thrust vector  $\mathbf{F}_I$ .

$$\vec{T}_I = (\mathbf{r}_T - \mathbf{r}_{com}) \times \mathbf{F}_I. \quad (2.7)$$

The thruster position and thrust direction were obtained from Cometto (2007).

The misalignment torque is plotted for one orbit in Figure 2.2. The misalignment causes a significant offset in the yaw torque, but shows no great influence in the other directions. The change in altitude over the orbit causes a change in density and therefore in thruster activation, which is directly introduced into the torque (visible as a dip in Figure 2.2 around 16:30).

Changing the location of the center of mass over the specified mission range does not significantly affect  $\vec{T}_I$ . The direction of  $\mathbf{F}_I$  is a more sensitive parameter. A sen-

sitivity analysis proved that an alignment error of  $0.1^\circ$  around the  $y_B$ -axis may already increase this torque by a factor of 3.5. Similar results are obtained in roll and yaw direction when rotating the torque around the  $z_B$ -axis instead. The reported error margin of  $0.90^\circ$  half-cone angle around the  $y_B$ -axis and  $0.05^\circ$  around the  $z_B$ -axis (Kolkmeier et al., 2008) therefore leaves a wide range of possible model outputs.

The ion thruster assembly includes a large electromagnet. The dipole of this magnet,  $\boldsymbol{\mu}_I$ , is modeled as a linear function of the current running through it (Kolkmeier et al., 2008), and a term for the product of torquer and thruster magnet current, as

$$\boldsymbol{\mu}_I = (\boldsymbol{\mu}_{I,H} + M_{I,S} \mathbf{I}_T) I_I. \quad (2.8)$$

Here  $\boldsymbol{\mu}_{I,H}$  is the hard magnetic part induced by the electromagnet in the ion thruster,  $M_{I,S}$  is a  $3 \times 3$  matrix representing the soft magnetic part depending on the torquer activation, and  $\mathbf{I}_T$  and  $I_I$  are the three torquer currents and the thruster current respectively. Note that the sign of the documented dipole was found to be wrong (as discussed in section 2.4.5) and therefore changed.

The thruster magnet current is filtered to remove sampling noise caused by the on-board down-sampling from 100Hz to 1/8Hz in the housekeeping data. It was observed that the most noisy periods coincide with episodes of high noise in the recorded thrust. Therefore an exponential moving average filter is used that is locally adapted with the difference between the commanded and recorded thrust. The filter, with a width of 9 data points, takes the form

$$I_I = \frac{\sum_{i=-4}^4 I_I^{\text{unfiltered}} \exp\left(\frac{-0.01|i|}{v}\right)}{\sum_{i=-4}^4 \exp\left(\frac{-0.01|i|}{v}\right)}, \quad (2.9)$$

where  $v$  is the triangular mean square error between commanded and recorded thrust in the filter window.

The magnetic torque from the ion thruster is plotted separately in Figure 2.2. The torque is dominated by a trend comparable to that of the constant dipoles (discussed hereafter), but a high frequency signal can be seen in pitch at locations near the magnetic poles where strong wind and density variations are expected.

### 2.3.6. CONSTANT DIPOLES OF SPACECRAFT BUS AND PAYLOAD

The magnetic dipoles of equipment on GOCE play an important role in modeling the total torque. Currently information is only available for dipoles caused by the spacecraft bus. The magnetic dipoles caused by the payload have to be estimated.

The constant bus dipoles can be subdivided in two categories. The first are due to long term, hard magnetic effects  $\boldsymbol{\mu}_{B,H}$  in the fuel tanks and latch valves. These cause the main part of the total magnetic torque on the spacecraft. When electric components of the bus, such as valves, are switched on or off, the hard magnetic dipole can suddenly change. During nominal operations no such events were observed. Soft magnetic dipoles form the second category. Contrary to hard magnetic effects, these dipoles are induced by a local magnetic field. In this case the dipole is assumed to depend linearly

on the local Earth's magnetic field strength (through matrix  $M_{B,S}$ ) and the torquer currents (through  $M_{B,T}$ ). Combined these contributions result in a magnetic torque (*Kolkmeier et al., 2008*)

$$\bar{\mathbf{T}}_{D,B} = (\boldsymbol{\mu}_{B,H} + (M_{B,S} + M_{B,T}|\mathbf{I}_T|)\mathbf{B}_E) \times \mathbf{B}_E, \quad (2.10)$$

with  $|\mathbf{I}_T|$  the  $L^2$ -norm of the currents to the magnetic torquers, and  $\mathbf{B}_E$  the Earth's magnetic field obtained from the calibrated magnetometer measurements.

The magnetic torque  $\bar{\mathbf{T}}_{D,B}$  only includes magnetic effects from the spacecraft bus. For the dipoles of the payload (gradiometer and GPS system), no data is available. Calculating the residual torque as described in the next section, it is found that these missing magnetic dipoles have a significant influence on the model quality. In the remainder of this section the procedure to estimate the dipoles is described, as well as the model result.

First of all the residual, unmodeled torque is obtained by reducing the measured torque by all model outputs described before. The result reveals a periodic signal that repeats every 10.5 minutes ( $1.59 \times 10^{-3}$  Hz). This is not a higher mode of the orbital frequency or a contribution from any of the models, and is therefore considered an artifact of the data processing. As the signal is most prominent in the roll and pitch axes, and it was to our knowledge not observed in the linear accelerations before, this signal most likely stems from the attitude determination and control system. The signal is removed from the residual by a series of seven notch filters centered at the central frequency and the closest two lower and four higher modes.

Second of all it must be decided what types of dipoles are to be fitted. From the earlier discussion it is clear that we can distinguish between constant and variable dipoles on one hand, and hard magnetic and soft magnetic dipoles on the other. To prevent fitting to the control algorithm or aerodynamic signals, no variable dipoles are estimated. The constant hard magnetic dipole  $\boldsymbol{\mu}_{P,H}$  is simply a three element vector, whereas the soft magnetic dipole is assumed to be linearly dependent on the Earth magnetic field through a  $3 \times 3$ -matrix  $M_{P,S}$ . As discussed in section 2.3.1 a full  $3 \times 3$  scale matrix  $S_T$  for the control dipoles is estimated alongside above mentioned dipoles. To prevent overfitting to for example a remaining bias in the measured torque, or an error in the aerodynamic model, a three element offset vector  $\mathbf{T}_{off}$  is estimated alongside the dipoles. Combining the above contributions, we assume that the measured torque can be written as

$$\begin{aligned} \mathbf{T} &= \bar{\mathbf{T}} + \bar{\mathbf{T}}_{D,P} + \mathbf{T}_{off} + \boldsymbol{\varepsilon} \\ &= \bar{\mathbf{T}} + (\boldsymbol{\mu}_{P,H} + M_{P,S}\mathbf{B}_E + S_T\boldsymbol{\mu}_T) \times \mathbf{B}_E + \mathbf{T}_{off} + \boldsymbol{\varepsilon}, \end{aligned} \quad (2.11)$$

with  $\boldsymbol{\varepsilon}$  a random error. Note that contrary to the definition of  $\bar{\mathbf{T}}$  in Equation (2.1) we exclude  $\bar{\mathbf{T}}_{D,P}$  from the total model here and explicitly add it as a term in the equations.

Third of all the elements of  $\boldsymbol{\mu}_{P,H}$ ,  $M_{P,S}$ ,  $S_T$ , and  $\mathbf{T}_{off}$  are estimated by minimizing the weighted square error

$$\min \boldsymbol{\varepsilon}^T \mathbf{W}^2 \boldsymbol{\varepsilon}, \quad (2.12)$$

where the diagonal weight matrix  $W$  is constructed using a local central estimation scheme. In this scheme Equation (2.12) is solved using ordinary least squares at each time instant, based on the closest 47 data points (23 both forward and backward in time). The local weight is then defined as the inverse of the root mean square error between the local fit and the residual torque over the full range of 47 data points.

To solve the minimization problem in Equation (2.12) the estimated torque in Equation (2.11) is rewritten to

$$\hat{\mathbf{T}}_{D,P} = -\mathbf{B}_{E,H}\boldsymbol{\mu}_{P,H} - \mathbf{B}_{E,S}\mathbf{M}_{P,S} - \mathbf{B}_{E,T}\mathbf{S}_T, \quad (2.13)$$

where  $\mathbf{B}_{E,H}$  is the cross-product matrix with the elements of  $\mathbf{B}_E$ . The vector  $\mathbf{M}_{P,S}$  is the vectorization of  $\mathbf{M}_{P,S}^T$ , and the  $3 \times 9$ -matrix  $\mathbf{B}_{E,S}$  is defined as

$$\mathbf{B}_{E,S} = \begin{bmatrix} \mathbf{0} & -\mathbf{B}_E^T \mathbf{B}_{E,z} & \mathbf{B}_E^T \mathbf{B}_{E,y} \\ \mathbf{B}_E^T \mathbf{B}_{E,z} & \mathbf{0} & -\mathbf{B}_E^T \mathbf{B}_{E,x} \\ -\mathbf{B}_E^T \mathbf{B}_{E,y} & \mathbf{B}_E^T \mathbf{B}_{E,x} & \mathbf{0} \end{bmatrix}. \quad (2.14)$$

Similarly,  $\mathbf{S}_T$  is the vectorization of  $\mathbf{S}_T^T$  and the  $3 \times 9$ -matrix  $\mathbf{B}_{E,T}$  is obtained from Equation (2.14) by replacing all occurrences of the magnetic field vector  $\mathbf{B}_E^T$  by the torquer dipole  $\boldsymbol{\mu}_T^T$ .

By collecting  $\boldsymbol{\mu}_{P,H}$ ,  $\mathbf{M}_{P,S}$ , and  $\mathbf{S}_T$  in a single column vector, and combining the matrices accordingly, the dipoles and scale factors can be fitted simultaneously. The offset  $\mathbf{T}_{off}$  is included in the estimation by adding a  $3 \times 3$  identity matrix  $\mathbf{I}_3$ . Setting  $\hat{\mathbf{T}}_{D,P} = \mathbf{T} - \hat{\mathbf{T}}$ , filling in  $\mathbf{B}_E = [-\mathbf{B}_{E,H}, -\mathbf{B}_{E,S}, -\mathbf{B}_{E,T}, \mathbf{I}_3]$ , and collecting these over the measurements 1 up to  $n$ , we may solve for the dipole estimate (indicated with a hat) as

$$\begin{pmatrix} \hat{\boldsymbol{\mu}}_{P,H} \\ \hat{\mathbf{M}}_{P,S} \\ \hat{\mathbf{M}}_T \\ \hat{\mathbf{T}}_{off} \end{pmatrix} = \left( \mathbf{W} \begin{bmatrix} (\mathbf{B}_E)_1 \\ \vdots \\ (\mathbf{B}_E)_n \end{bmatrix} \right)^+ \mathbf{W} \begin{pmatrix} (\mathbf{T} - \hat{\mathbf{T}})_1 \\ \vdots \\ (\mathbf{T} - \hat{\mathbf{T}})_n \end{pmatrix}. \quad (2.15)$$

The cross product in Equation (2.11) is not invertible due to the soft magnetic part  $\mathbf{M}_{P,S}$ . This is best illustrated by writing the dipole matrix as  $\mathbf{M}_{P,S} = \mathbf{M} + m\mathbf{I}_3$ . Filling this into Equation (2.11) and writing out the cross product, we find the term  $m\mathbf{I}_3 \mathbf{B}_E \times \mathbf{B}_E$ , which is zero, independent of  $m$ . This diagonal value is thus arbitrary, leaving one degree of freedom unresolved. Therefore the Moore-Penrose pseudo-inverse ( $^+$ ) is used.

Daily estimates of the payload dipoles are computed for the whole mission (see Figure 2.4). A linear fit is made for each element, to allow for ageing of satellite components. For the hard magnetic dipole  $\hat{\boldsymbol{\mu}}_{P,H}$  two separate linear fits are made, one for when the redundant GPS receiver is off (the nominal case), and one for when it is turned on (the highlighted periods in the top row of Figure 2.4). It is assumed that the other dipole elements are not affected by this receiver. The parameters of the linear trends can be found in Table 2.4.

Finally the estimated torque becomes

$$\hat{\mathbf{T}}_{D,P} = (\hat{\boldsymbol{\mu}}_{P,H} + \hat{\mathbf{M}}_{P,S}\mathbf{B}_E + \hat{\mathbf{S}}_T\boldsymbol{\mu}_T) \times \mathbf{B}_E. \quad (2.16)$$

Table 2.4: Parameters of the linear fits of the daily dipole estimates. Time  $t$  is expressed in days since the start of the science phase of the mission (November 1, 2009).

| Dipole  | $x_B$                             | $y_B$                             | $z_B$                             |
|---|-----------------------------------|-----------------------------------|-----------------------------------|
| Hard dipole $\hat{\mu}_{RH}^T$ (SSTI-B off) [ $\text{Am}^2$ ] | $-0.85 + 5.11 \times 10^{-5} t$   | $0.70 - 5.46 \times 10^{-5} t$    | $-1.68 + 1.36 \times 10^{-4} t$   |
| Hard dipole $\hat{\mu}_{RH}^T$ (SSTI-B on) [ $\text{Am}^2$ ]  | $-0.89 + 2.29 \times 10^{-4} t$   | $0.83 - 1.39 \times 10^{-4} t$    | $-1.69 + 2.27 \times 10^{-4} t$   |
| Soft dipole $\hat{M}_{PS}$ [ $\text{mAm}^2/\text{nT}$ ]       | $-0.0155 + 1.80 \times 10^{-6} t$ | $0.0006 + 8.39 \times 10^{-6} t$  | $-0.0011 + 3.63 \times 10^{-6} t$ |
|   | $0.0096 - 2.22 \times 10^{-7} t$  | $0.0154 - 1.81 \times 10^{-6} t$  | $-0.0058 + 1.88 \times 10^{-7} t$ |
|   | $0.0047 - 5.52 \times 10^{-7} t$  | $-0.0009 + 1.49 \times 10^{-6} t$ | $0.0001 + 6.15 \times 10^{-9} t$  |
| Torquer scale factors $\hat{S}_r$ [-]                         | $0.0844 - 1.05 \times 10^{-9} t$  | $-0.0197 + 2.55 \times 10^{-5} t$ | $0.0105 + 4.39 \times 10^{-6} t$  |
|   | $0.0105 - 3.55 \times 10^{-7} t$  | $0.0755 - 1.36 \times 10^{-5} t$  | $0.0036 + 1.73 \times 10^{-6} t$  |
|   | $0.0005 - 5.38 \times 10^{-6} t$  | $-0.0209 + 2.51 \times 10^{-5} t$ | $0.0555 - 4.16 \times 10^{-6} t$  |
| Offset $\hat{t}_{o/f}^T$ [mNm]                                | $-848.2 + 5.11 \times 10^{-2} t$  | $701.8 - 5.46 \times 10^{-2} t$   | $-1679.9 + 1.36 \times 10^{-1} t$ |

In Figure 2.2 the constant bus and payload dipole torques are plotted together. The constant magnetic dipoles cause the largest disturbance torques in roll and pitch, and with that dictate the low frequency trend in the control torque.

It is unclear up to what extent the reported bus dipoles are correct. For some contributions an indeterministic part is given in the documentation, which in a few cases implies an error margin of 10% (Kolkmeier *et al.*, 2008). Most of these errors are expected to be eliminated by the estimation of the payload dipoles.

## 2.4. VALIDATION

Combining the models of section 2.3 we find a total modeled torque  $\bar{\mathbf{T}}$ . To compare this to the measurements, the measured angular acceleration is combined with the angular rate to find a measured torque  $\mathbf{T}$ . This is done using the well-known relation

$$\mathbf{T} = \mathbf{J}\boldsymbol{\alpha} + \boldsymbol{\omega} \times \mathbf{J}\boldsymbol{\omega}. \quad (2.17)$$

Here  $\mathbf{J}$  is the interpolated inertia tensor,  $\boldsymbol{\alpha}$  is the measured angular acceleration, and  $\boldsymbol{\omega}$  is the measured angular rate of the satellite body.

The angular acceleration product EGG\_CGA is not fully calibrated. A bias from the expected zero-mean can be observed, that drifts over the mission. Therefore a calibration effort was performed similar to the one described for the magnetometers in section 2.3.1. In this case the mean angular acceleration was calculated for each day. Then a cubic polynomial was estimated to catch the drifting trend. The resulting bias is shown in Figure 2.5. Note that the accelerometers were calibrated regularly during the mission, causing the need for several cubic fits over parts of the mission. The bias in pitch acceleration was very small overall. To prevent overfitting to the noise in the daily means, linear fits were made for this component.

By taking the difference between the measured torque  $\mathbf{T}$  (plotted for May 19 to 31, 2011 in Figure 2.6) and the total modeled torque  $\bar{\mathbf{T}}$  (where  $\bar{\mathbf{T}}_{D,P}$  is replaced by the estimate  $\hat{\mathbf{T}}_{D,P}$ , plotted in Figure 2.7) the quality of the models can be evaluated. For May 19 to 31, 2011, this residual torque is plotted in Figure 2.8. In the remainder of this section several individual torque models are validated by investigating the residual torque during special events.

### 2.4.1. MAGNETIC CONTROL TORQUE

Throughout the mission the torquer activation is regularly enhanced significantly by a periodic signal in the frequency range above 15 times per orbit. A similar oscillation was observed before in the magnetic torquer activity on GRACE by Bandikova *et al.* (2012), but the exact cause of this behavior remains unknown. On GOCE it occurs approximately once or twice each month and lasts from a few hours to several days. The activity is clearly present in the measured pitch signal, as in Figure 2.6b from May 21 to 25, 2011. Such activity allows for validating the torquer model and the estimated torquer scale factors  $\hat{S}_T$ , as it temporarily raises the control torque above the error level of other models over a fixed frequency range.

The episode under consideration here is a particularly short one, lasting only a few hours on May 5, 2011. All torques are filtered using a third-order high-pass Butterworth

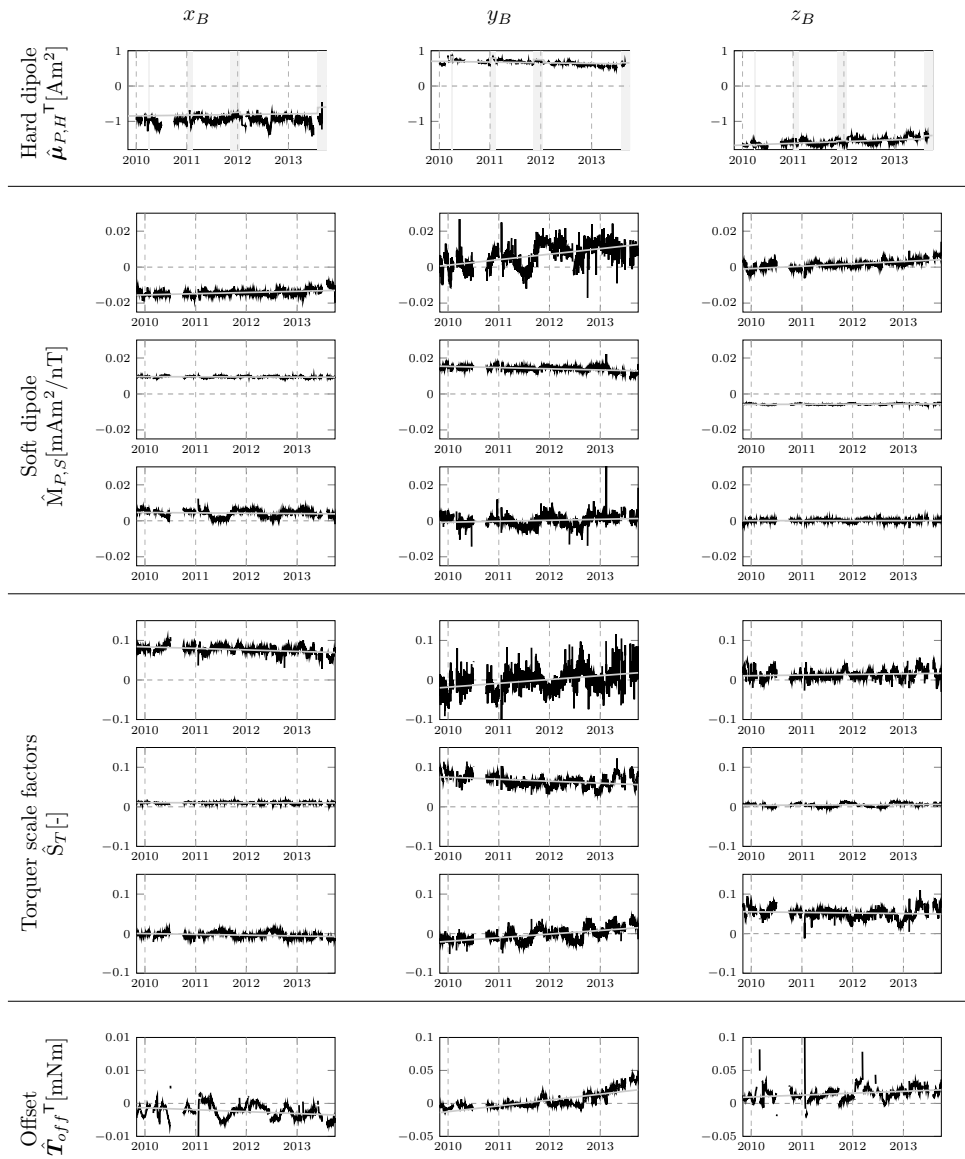


Figure 2.4: The daily estimates of payload dipoles, torquer scale factors, and torque offsets over the entire mission, with the linear fits in gray. In the top row the episodes when the redundant GPS system was turned on are highlighted in light gray.

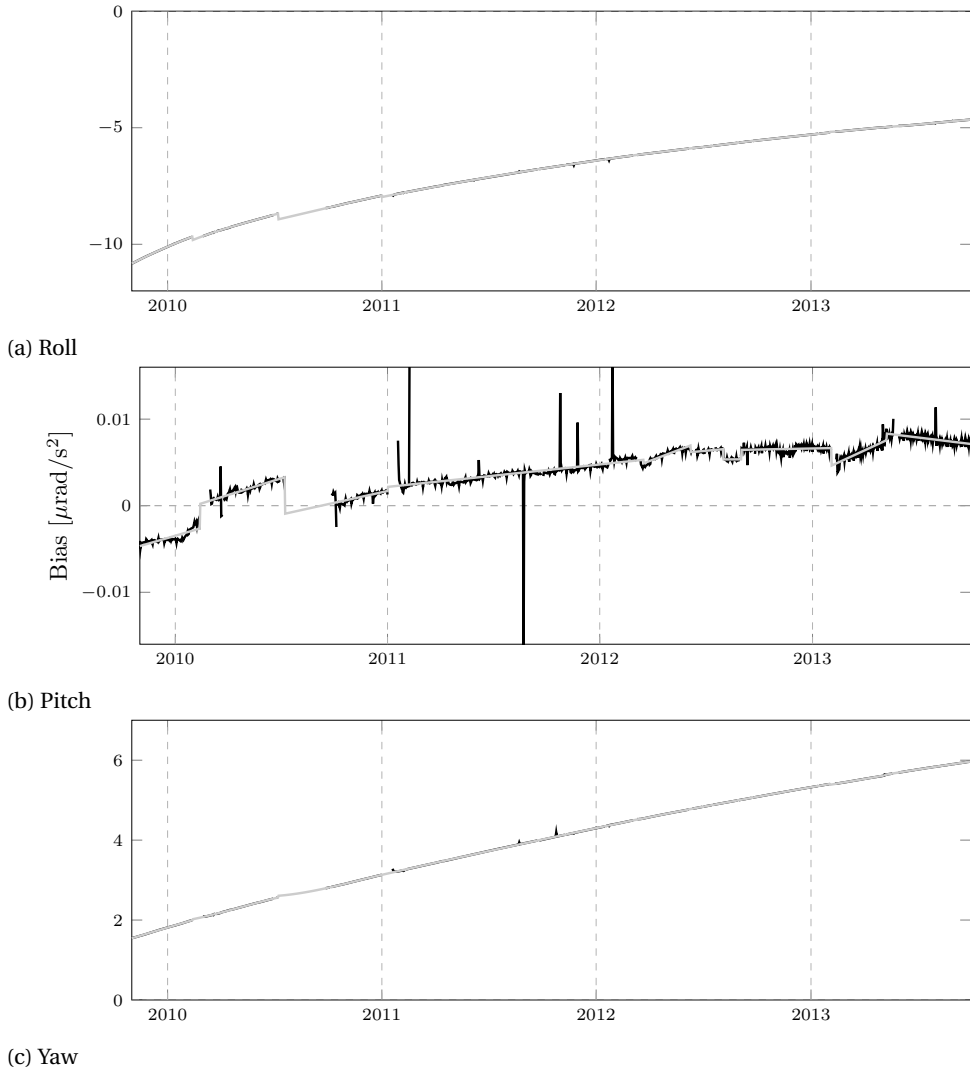


Figure 2.5: Bias of the three angular accelerations for the full mission, with the fitted polynomials in gray.

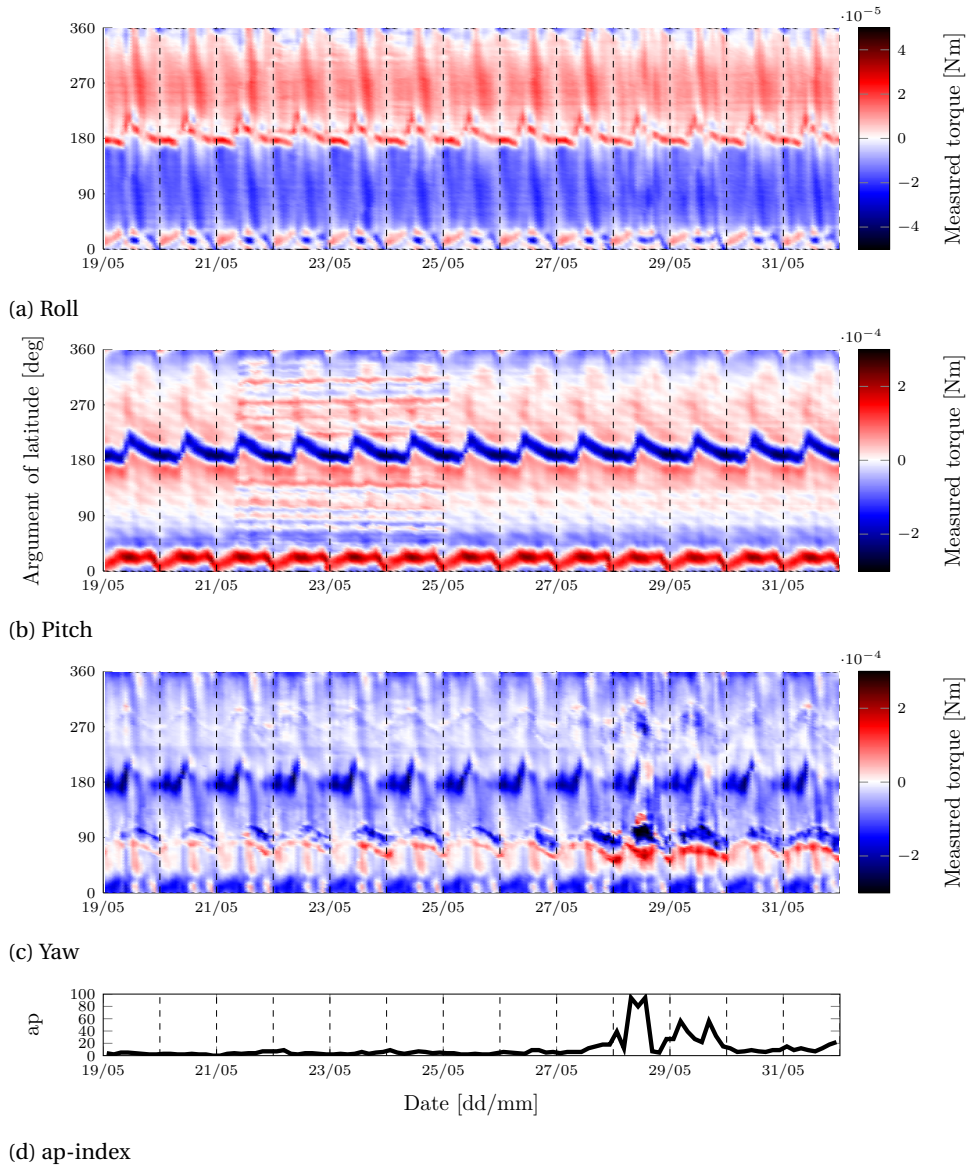


Figure 2.6: Measured torque between May 19 and 31, 2011.

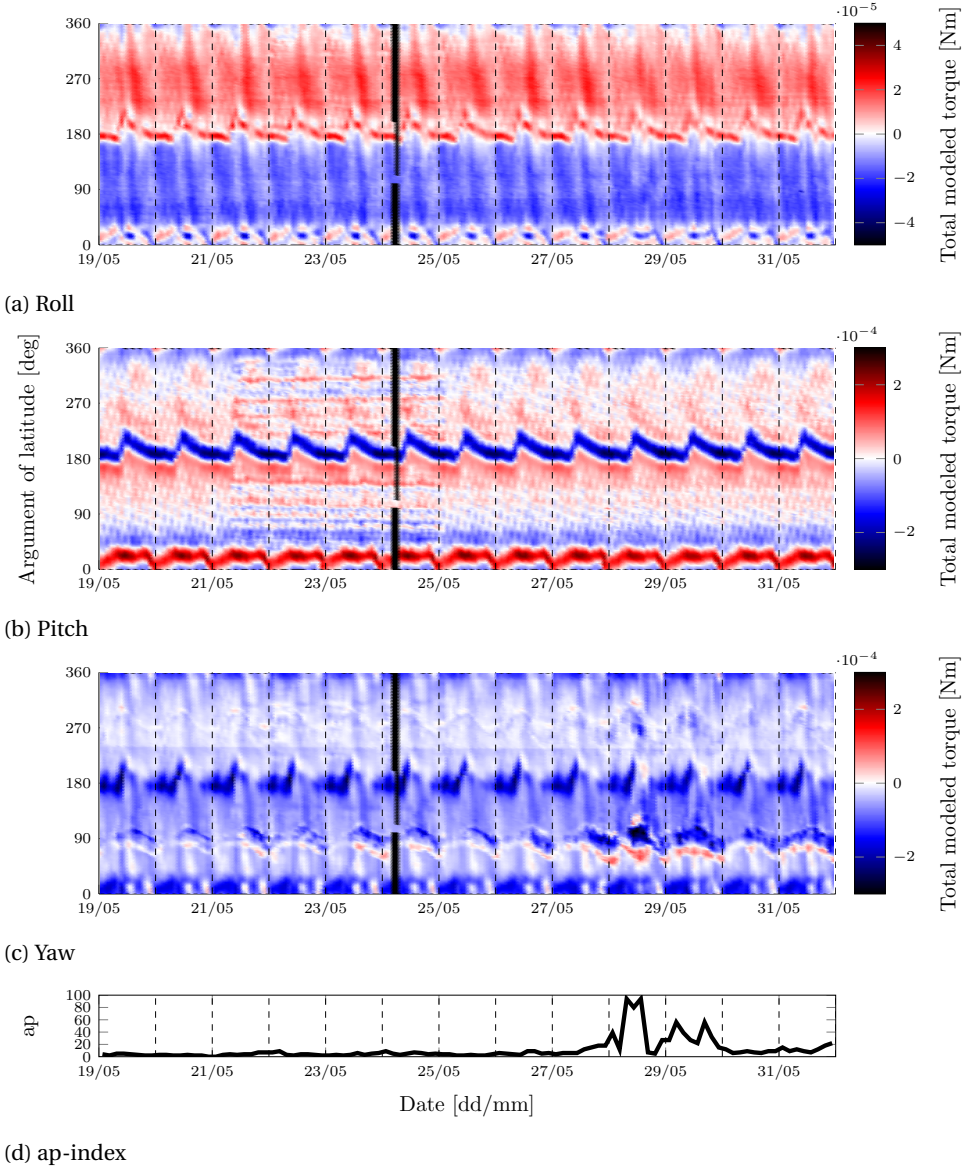


Figure 2.7: Total modeled torque between May 19 and 31, 2011, including estimated magnetic contributions.

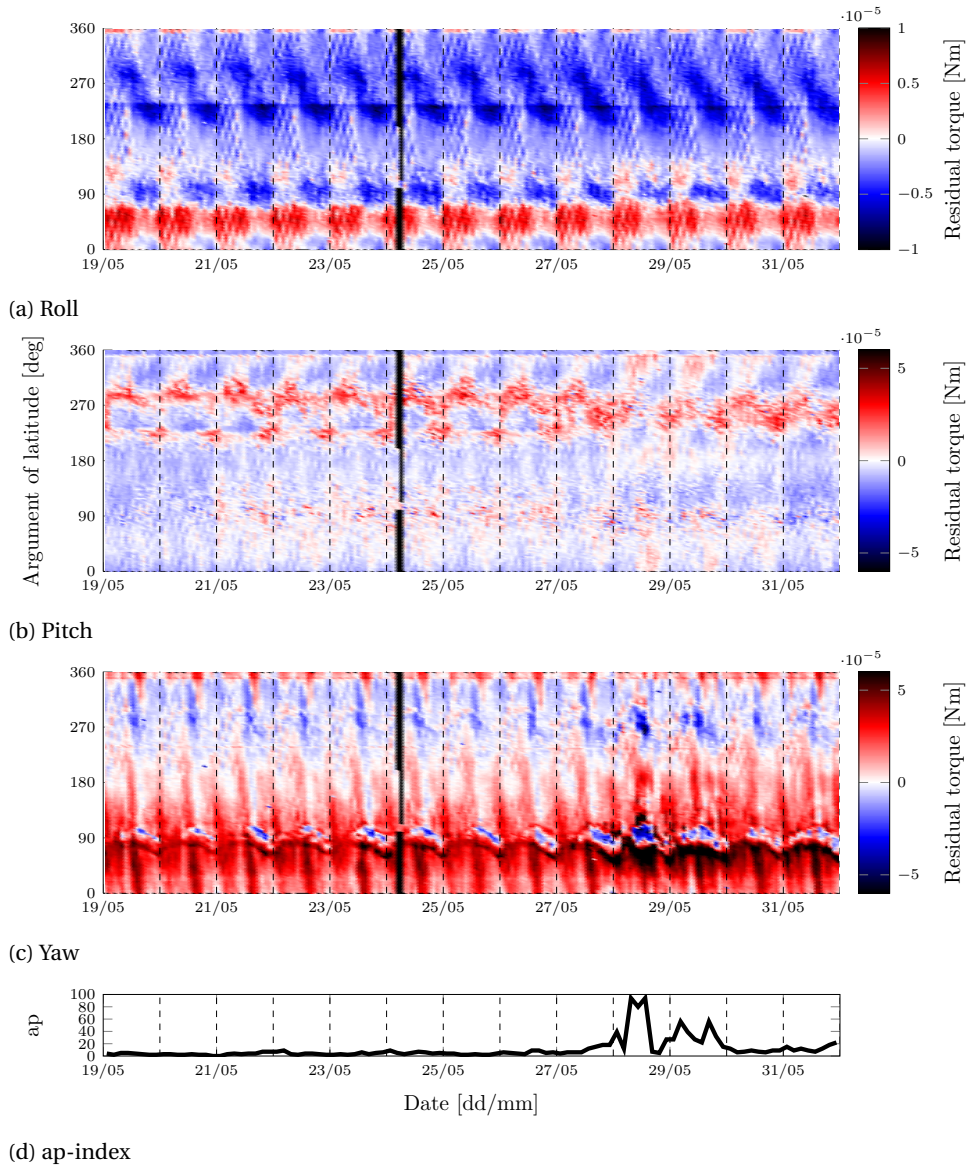


Figure 2.8: Residual torque between May 19 and 31, 2011, including estimated magnetic contributions. (Note different scale than 2.6.)

filter with a cut-off frequency corresponding to 15 times per orbit. The filtered residual torque  $\mathbf{T} - \tilde{\mathbf{T}}$  is then compared to the filtered control torque  $\tilde{\mathbf{T}}_T$  by calculating Pearson's correlation coefficient. This coefficient is expected to increase if the increased torquer activation also affects the residual, i.e. the coefficient should respond only if the torquer model is incorrect. A time series is constructed by calculating the correlation coefficient over a moving central window of one orbital period. This procedure is repeated for the comparison of the residual torque before and after including the estimated torquer scale factors  $\hat{\mathbf{S}}_T$  on the one hand, and the (documented) control torque on the other hand. The result is shown as a time series of the correlation coefficients in Figure 2.9. First of all, the correlation between measured torque and modeled control torque (dashed black line) shows the importance of the control torque in the frequency range of interest. Only in yaw the correlation deviates significantly from one, indicating again the reliance on GOCE's passive aerodynamic stability in that axis. Over the highlighted episode of increased control (light gray box) the correlation between measured and control torque in pitch approaches one, while roll and yaw show no such response. The correlation between the control and the residual (solid black line) in pitch increases significantly. The inclusion of the estimated scale factors (7.5% on the  $x_B$ -directed torquer, 6.5% on  $y_B$ , and 4.8% on  $z_B$ ; up to 1.5% off-diagonal) greatly reduces this response.

In Figure 2.4 the scale factor matrix elements are plotted over the full mission. The elements are approximated well by a linear trend, except for the off-diagonal elements pertaining to the  $y_B$ -directed torquer (in the second column). This torquer mostly controls the roll motion. The small scale of the torques in this direction may be the cause of this erratic behavior.

To test whether the torquer scale factors are within the documented error bounds, the  $3 \times 3$  matrix must be converted to one scale factor per torquer, and a misalignment angle. Writing the total control torque as

$$\tilde{\mathbf{T}}_T = (\mathbf{I}_3 + \hat{\mathbf{S}}_T) \boldsymbol{\mu}_T \times \mathbf{B}_E \quad (2.18)$$

we observe that the matrix  $(\mathbf{I}_3 + \hat{\mathbf{S}}_T)$  describes a scaling and rotation of the control dipole  $\boldsymbol{\mu}_T$  from the three magnetic torquers. The individual scale factor per magnetic torquer is then the norm of each column of this matrix. After normalizing each column, the diagonal elements represent the cosines of the misalignment angles. Following this process, we find that the estimated linear trends produce scale factors that are within the documented uncertainty bounds of 0 to +10% (*Kolkmeier et al., 2008*). The misalignment of the  $x_B$ - and  $z_B$ -directed torques stay within the maximum  $2^\circ$  half-cone angle (*Kolkmeier et al., 2008*) throughout the mission, while the  $y_B$ -directed torquer violates this bound starting March of 2013, to rise to  $2.4^\circ$  at the end of the science mission.

### 2.4.2. AERODYNAMICS

During geomagnetic storms the atmosphere is locally heated, causing it to expand. This expansion increases the neutral density in the thermosphere, as well as the wind speed at the satellite's orbital altitude. The effect on the (yaw) torque can be clearly seen in Figure 2.6 on May 28. The magnetic storm of April 5, 2010 is used to validate the aerodynamic torque. The same approach is taken as for the magnetic control torque. In this case the measured and residual torque are compared to the aerodynamic model. All torques are

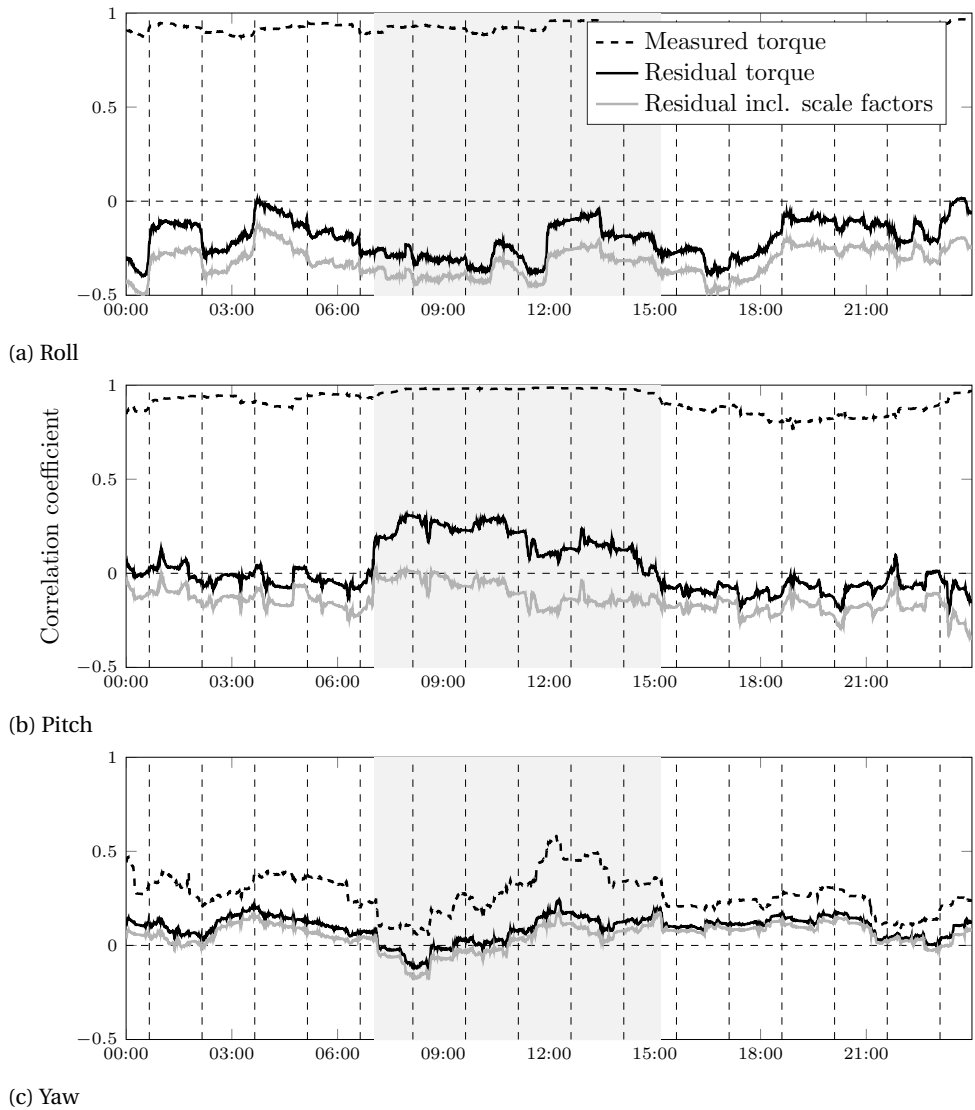


Figure 2.9: Correlation coefficients between high-pass filtered control torque on one hand, and the filtered measured torque, residual, or residual including torquer scale factors on the other hand for May 5, 2011. The highlight indicates the time of increased torquer activation.

filtered using a third-order high-pass Butterworth filter with a cut-off frequency at 1.5 times per orbit, as the aerodynamic model is most active at frequencies twice per orbit and higher.

The correlation coefficients are plotted over five days surrounding the storm in Figure 2.10. While the roll and pitch torques are mostly unaffected, the yaw torque residual clearly responds to the storm. The correlation between the residual and the aerodynamic model increases significantly at the start of the storm and takes on a more constant trend. The dip in correlation that occurs at the start of each day is almost entirely removed from the signal. The increased correlation between the residual and aerodynamic torque during the storm implies that the aerodynamic model represents the trend well, but fails to properly model the magnitude of the actual aerodynamic torque. Therefore we conclude that significant errors remain in the magnitudes of either the aerodynamic model coefficients or the thermospheric wind and density data.

### 2.4.3. GRAVITY GRADIENT

During its mission, GOCE has not made any extreme attitude maneuvers while in science mode, making it impossible to isolate a moment in time in which the gravity gradient is the major cause of a change in torque. Therefore the residual torque is compared for different orders of the gravity model in the frequency domain. In Figure 2.11 the comparison is shown for the cases with and without the  $J_2$ -term. From this comparison it was found that, as expected, the oblateness term is an important and non-negligible contribution to the total torque. In pitch this element introduces a significant peak in the PSD of the model, that reduces the peak in the residual at twice-per-orbit frequencies. In yaw its contribution is even a factor 5 larger than that of the basic spherical Earth model. This signifies the importance of the gravity gradient torque, but due to the lack of special maneuvers no further validation can be performed.

### 2.4.4. SOLAR RADIATION PRESSURE

Implementing the ANGARA model for all moment coefficients, it was found that the residual torque in roll strongly resembled the solar radiation pressure torque. Therefore the ANGARA coefficients were compared to a simplified fully specular 36-panel model (from Dumontel (2010), excluding the radiator). Assuming a reflectance of 0 for the solar panel-covered side and a reflectance of 0.8 for the radiator side, a close fit is found between the two models for all force and torque coefficients but the roll coefficient. It was therefore decided to use the several orders of magnitude smaller roll coefficient from the simplified model instead of the one obtained from the ANGARA software.

The eclipse transitions present an opportunity to validate the solar radiation pressure model using a superposed epoch analysis. In Figure 2.12 the residual torque (including the solar radiation pressure) is presented for April 12 to 22, 2011, for 300 seconds before and 500 seconds after the start of the (modeled) transitions out of eclipse. During the displayed period the eclipses grow longer, from partial eclipses at the start to full eclipses of 10 minutes at the end.

The residual shows two striking trends of different nature. The first is a line of roll torque peaks running from 320 at the start of the plotted period to 120 seconds after transition at the end. The same trend can be observed as a negative pitch torque, but

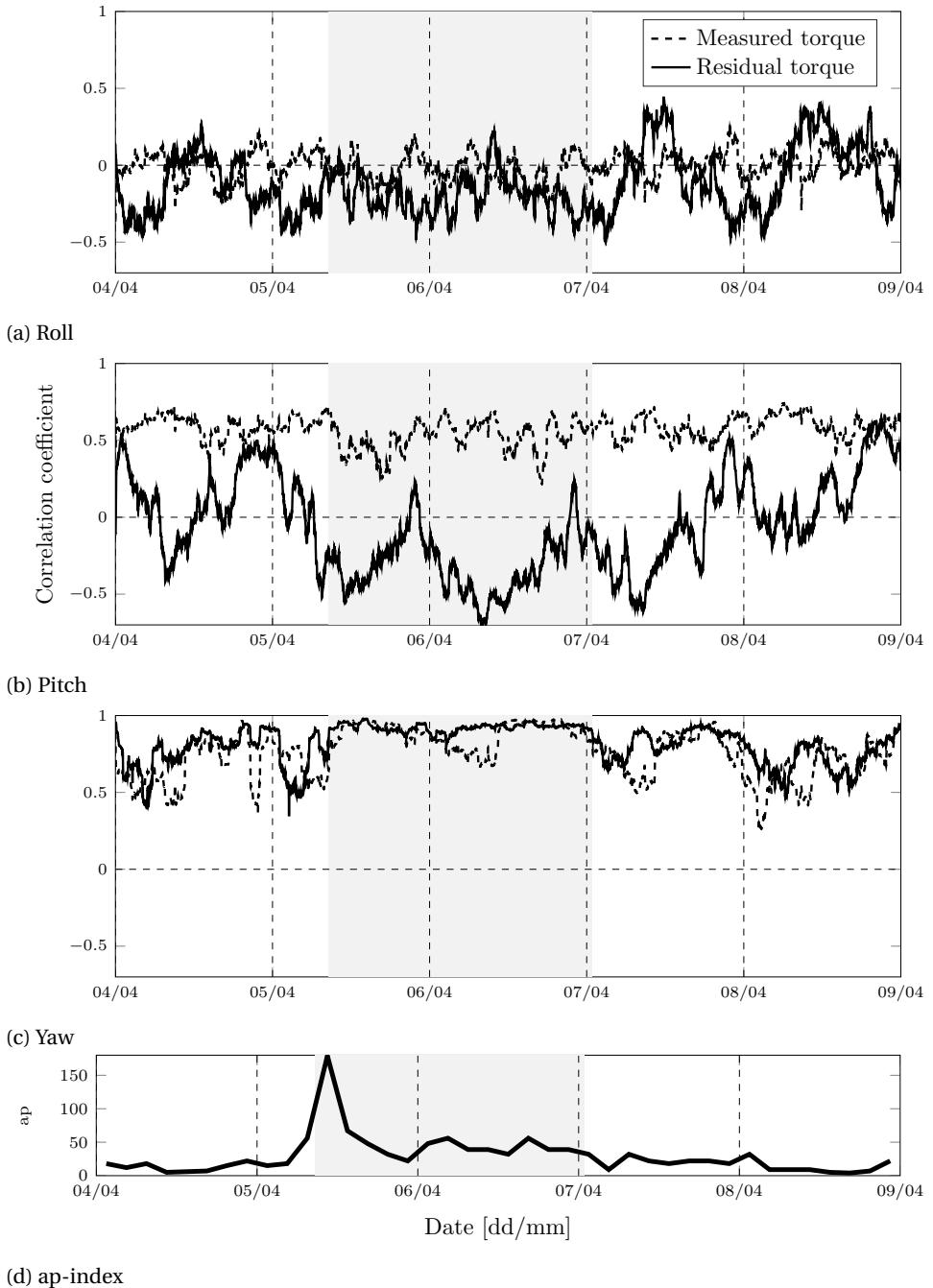


Figure 2.10: Correlation coefficients between high-pass filtered aerodynamic torque on one hand, and the filtered measured or residual torque on the other hand for five days in April 2010. The highlight indicates the time of increased ap-index values.

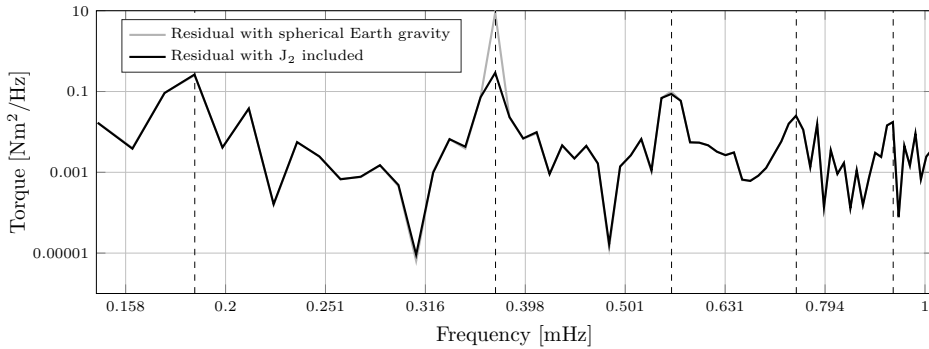


Figure 2.11: Frequency domain plot of the pitch torque residual when assuming gravity points radially down compared to the residual including the  $J_2$ -term. Dashed lines indicate one up to five times the orbit frequencies.

is not visible in the yaw direction. Because of the periodic nature of the line, showing intensity and direction fluctuations on a daily basis, it is hypothesized that this is a magnetic signal. In Figure 2.13 the residual roll torque is plotted alongside the magnetometer measurements and solar panel currents for a single transition out of eclipse. As the solar panel current increases, so does the on-board magnetic field that is registered by the magnetometers. It is possible that the satellite switches from battery to solar power just after the panels reach their maximum current, about 110 seconds after the start of the transition. A magnetic dipole caused by the rapid change in current flow through the satellite could explain the steep drop in both the on-board magnetic field and the roll torque. Attempts to estimate the dipole of the solar panels as a function of provided current did however not yield consistent results.

The second trend is a wider band of increased residual yaw torque, visible as a bright red horizontal band in Figure 2.12c. It runs just below the magnetic line described above, and spans approximately 100 to 150 seconds per orbit. Because of its location, closer to the start of the transition, it is expected that this is a product of the overly simplistic eclipse model. In Figure 2.14 a single transition is isolated, and the residual yaw torque is plotted against the time into transition to test this hypothesis. The eclipse transition in the solar radiation pressure model (dashed line) is clearly a factor two to three faster than the actual transition visible in the residual torque excluding the solar radiation pressure model ( $T - (\bar{T} - \bar{T}_S)$ , solid gray line). This mismatch is causing the residual (solid black line) to first rapidly increase as the model transitions, and then recover to a level close to zero as the actual eclipse transition takes place. The solar radiation pressure model as a whole thus correctly represents the magnitude of the radiation torque, but fails to properly portray the eclipse transition process. Because of the overall small significance of this torque, the simplistic transition model is kept. The roll and pitch radiation torque are too small to repeat this test for those axes.

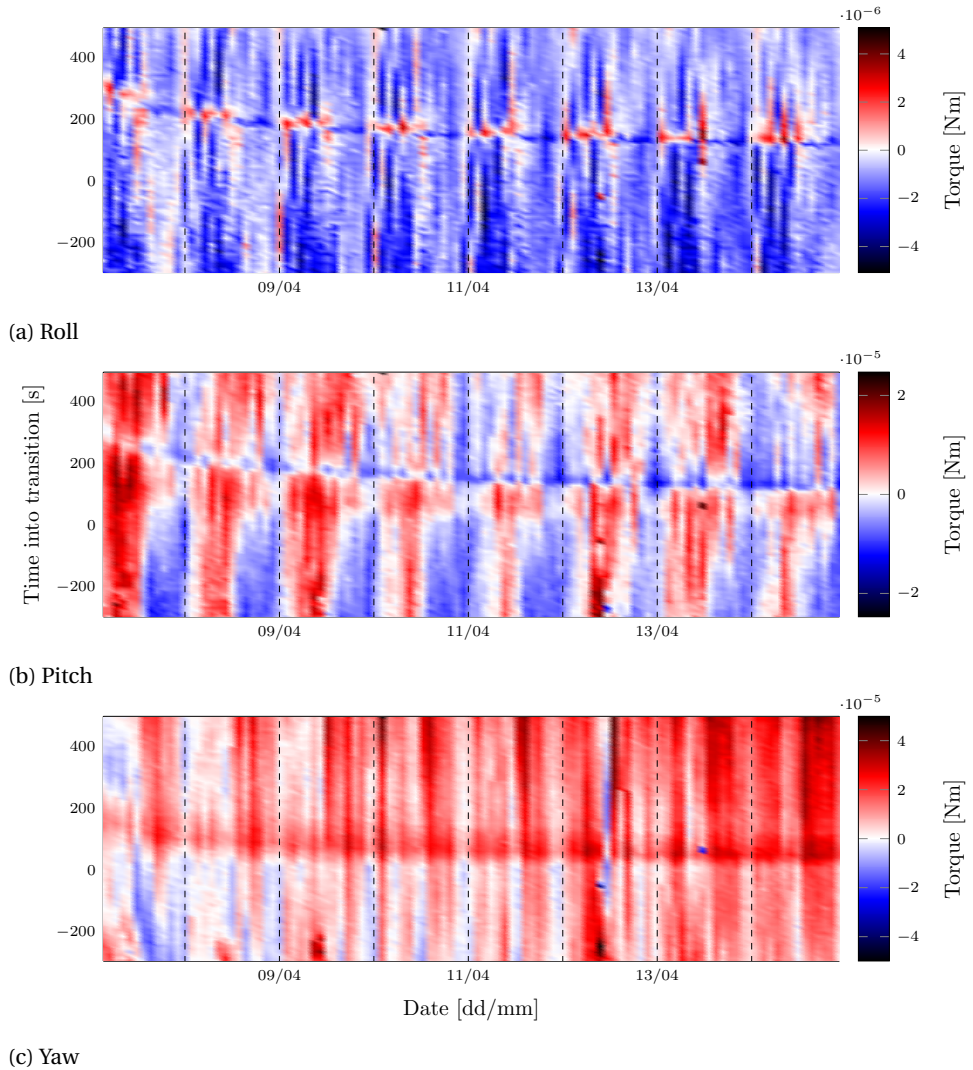


Figure 2.12: Residual torque during transitions out of eclipse over eight days in April 2011. The vertical axis represents the time in seconds since the start of the transition according to the solar radiation pressure model.

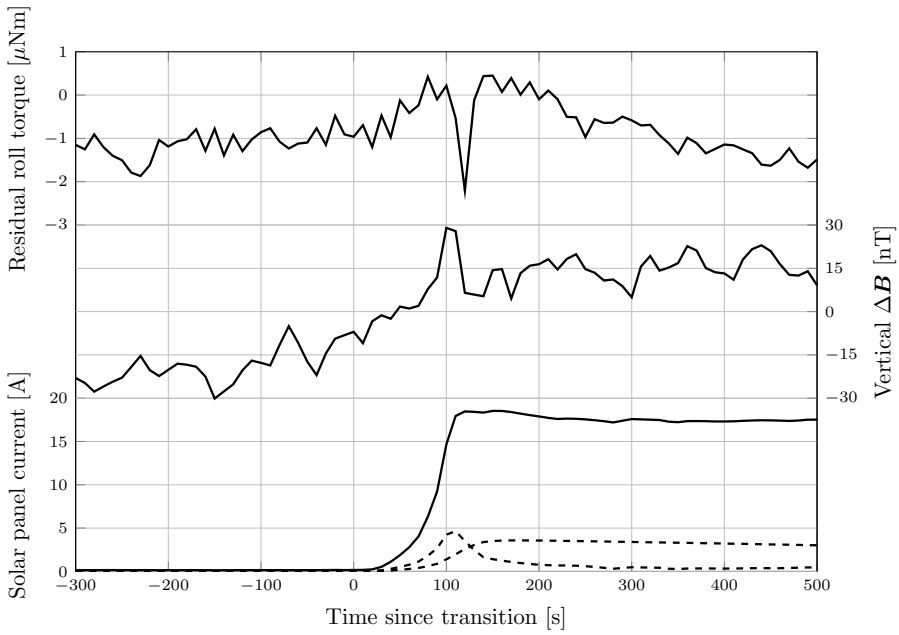


Figure 2.13: Residual roll torque, vertical magnetic field deviation from IGRF, and current from the solar panels (total (solid line) and two examples out of six panels (dashed lines)), as a function of the time since the transition out of eclipse on April 11, 2011, around 5:15 UTC.

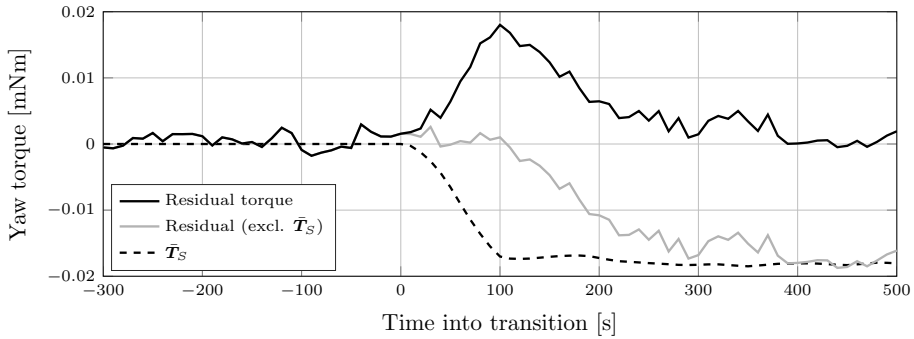


Figure 2.14: Residual yaw torque (black solid line), the residual excluding solar radiation pressure ( $T - (\bar{T} - \bar{T}_S)$ , gray solid line), and the solar radiation pressure model itself ( $\bar{T}_S$ , dashed line) versus the time into transition on the second orbit of April 8, 2011. The eclipse transition model is two to three times faster than the actual transition out of eclipse, causing a bump in the residual torque.

### 2.4.5. ION THRUSTER

In August 2012 GOCE's orbit was lowered by deducting a constant bias from the measured acceleration before computing the required thrust. The constant acceleration was large enough to command the minimum possible thrust over part of each orbit. This month therefore provides a good opportunity to validate the thruster related torques. At the moment of adding or removing the acceleration bias, a significant change in both the residual torque and the current through the ion thruster magnet occurs. The change in thrust on the other hand is relatively small. This suggests an error exists in the thruster dipole model. Therefore a dipole with the same model structure as in Equation (2.8) was estimated along with  $\bar{\mathbf{T}}_{D,P}$  on each day of August 2012.

The estimated hard magnetic part  $\hat{\boldsymbol{\mu}}_{I,H}$  is compared to the same element from the documented models in *Kolkmeier et al. (2008)* on scale and direction. The norm of the fitted dipole reduces over the month, from 99% of the documented one at the start to around 80% towards the end of August 2012. The dot product between the unit vectors remains close to -1 all through the month, with a minimum at -0.998. This result implies that the documented dipole has the wrong sign. After inverting the documented model, we inspected all jumps in thrust due to maneuvers over the entire mission. Taking the 65 jumps for which all required data are available, a linear fit is estimated between the modeled and observed jump in both force and torque. For the observation the difference between the measurement and all other models ( $\mathbf{T} - (\bar{\mathbf{T}} - \bar{\mathbf{T}}_I)$ ) is used. A good fit is found for force in the  $x_B$ - and  $z_B$ -direction (coefficient of determination ( $R^2$ ) above 0.99), with a linear term of 1.038 and 1.022 respectively. This implies that the error in the commanded thrust that is used in the model is indeed within the documented 5% (*Kolkmeier et al., 2008*). For the pitch and yaw torques linear terms of 0.21 and 0.52 are found respectively ( $R^2$  around 0.84). This mismatch can be explained by a combination of a rotation and repositioning of the thruster, but may also be affected by an error in the thruster dipole model. This process has many solutions within the documented error constraints, so no conclusion can be drawn regarding the actual position and orientation of the thruster. Therefore the model is kept as documented.

In the residual pitch torque a band of large errors is found around the South pole in the local winter months and other situations where the thermosphere neutral density is very low. At those instances the thrust level passes through a band around 2mN in which the thruster noise is significantly larger at around 5% (*Wallace et al., 2011*). In the case of the pitch torque it is not the thruster itself, but its main magnet that is causing the error. Attempts to estimate a scale factor for this dipole as was done for the torquers (described in section 2.3.6) have however not given consistent, reliable results. Therefore the thruster dipole torque is only considered validated for thrust levels above 3mN. Given GOCE's orbit, with the apogee over the South pole, thrust levels below this threshold occur mostly over the South pole during local winter, but have also been observed over the North pole. In the last year of the mission, when solar activity increases and the orbit is lower, the thrust remains above the threshold under nominal conditions.

### 2.4.6. CONSTANT DIPOLES OF SPACECRAFT BUS AND PAYLOAD

As not all dipoles are known, it is impossible to validate the torque they cause. Instead the trend of the fitted dipoles over time is investigated. As only constant dipoles were

Table 2.5: The root mean square error with respect to the linear fit of each estimated parameter, as a percentage of the maximum  $L^2$ -norm of the vector or matrix it is an element of.

|  | $x_B$ | $y_B$ | $z_B$ |
|--|-------|-------|-------|
| Hard dipole $\hat{\boldsymbol{\mu}}_{P,H}^T$ | 4.5%  | 2.1%  | 2.8%  |
|  | 6.0%  | 23.4% | 6.9%  |
| Soft dipole $\hat{M}_{P,S}$                  | 1.8%  | 5.2%  | 1.4%  |
|  | 7.9%  | 12.9% | 3.0%  |
| Torquer factors $\hat{S}_T$                  | 10.4% | 31.5% | 13.8% |
|  | 2.2%  | 15.8% | 4.6%  |
| Torque offset $\hat{T}_{off}^T$              | 6.8%  | 15.7% | 15.9% |
|  | 3.6%  | 34.4% | 41.3% |

estimated, they should not vary more than can be explained by aging or hardware being switched on or off. The downside of comparing dipoles is that the estimation process in Equation (2.15) does not have a unique solution. A different dipole therefore does not always imply a different torque. This effect is eliminated for most parameters by estimating a single set of dipoles using one full day of torque data. Only the diagonal components of the soft magnetic dipole do not have a unique solution, as explained in section 2.3.6.

In Figure 2.4 the daily estimates of hard and soft magnetic dipoles are plotted for the full mission. The hard magnetic dipole is similar in scale and opposite in sign to the bus dipole in the  $y_B$  and  $z_B$  axes (Kolkmeier et al., 2008, cf.). In  $x_B$  the sign is the same, but the estimated dipole is approximately five times as small as the bus dipole. All elements remain mostly constant over the first three years of the mission. The linear fit predicts a decrease in magnitude of  $0.05 \text{ Am}^2$  per year with a small overall prediction error (see Table 2.5). In the last year the  $x_B$  and  $z_B$  components show a stronger increasing trend, which can also be observed in some elements of the soft magnetic dipole, the magnetic torquer factors, and the estimated offsets. This episode starts with the end of the orbit-lowering maneuver of August 2012, but the cause of this behavior is unclear.

The hard magnetic dipole that is estimated for episodes in which both GPS receivers are turned on (highlighted in light gray in the top row of Figure 2.4) shows a stronger linear trend than the nominal estimated dipole. As this linear fit is dominated by a large set of data in the last months of the mission, this confirms the observed increasing trend in the hard magnetic dipole described above.

The diagonal soft magnetic elements (row 2–4 of Figure 2.4) are of similar scale as those reported for the spacecraft bus, while documented off-diagonal elements are generally two orders of magnitude smaller. They display similar consistency as the hard magnetic dipoles (see Table 2.5), except for those related to the cross-track component of the magnetic field (middle column). This can be explained by the fact that this component of the field is generally small throughout the (near-polar) orbit, leading to a high parameter variance.

The co-estimated offsets in the torques, plotted at the bottom of Figure 2.4, oscillate around the linear trend in the roll and yaw axes. In pitch the offset assumes a more profound increasing trend after the orbit maneuver in August 2012. This behavior explains the large error in the linear fit reported in Table 2.5.

Table 2.6: Standard deviation (STD) and bias of the residual torque over the period plotted in Figure 2.8, both absolute and relative (Rel.) to the STD of the control torque about the same axis.

|       | STD [mNm]             | Rel. STD [%] | Bias [mNm]             | Rel. bias [%] |
|-------|-----------------------|--------------|------------------------|---------------|
| roll  | $2.51 \times 10^{-3}$ | 15.6         | $-1.51 \times 10^{-3}$ | -9.4          |
| pitch | $7.25 \times 10^{-3}$ | 2.1          | $-1.14 \times 10^{-3}$ | -0.3          |
| yaw   | $1.67 \times 10^{-2}$ | 30.5         | $1.09 \times 10^{-2}$  | 19.9          |

### 2.4.7. COMPLETE MODEL

To evaluate the validity of the complete model, the residual is analyzed for the period in May 2011 plotted in Figure 2.8. In Table 2.6 the standard deviation (STD) of the residual is provided. To make a fair comparison with the actual torque acting on the satellite around each principle axis, the values are divided by the STD of the control torque acting on the satellite around that axis. This results in the relative standard deviation. To complete the table a column is added for the mean value of the residual, or the overall bias of the models. This value is again normalized with the STD of the control torque to find the relative bias.

From the table we find that the yaw residual has the largest relative value. Given the large aerodynamic signal in this direction, this result implies that especially the aerodynamic model requires improvement. The small residual in pitch indicates that the magnetic dipole models are performing well.

An error in the star camera alignment may cause part of the residual through the aerodynamic, gravity gradient, and radiation pressure models. For the EGG\_IAQ attitude product an error with standard deviation  $3''$  is to be expected around all axes (Stummer, 2012). A random normal noise signal with this standard deviation is added to the attitude (in case of the gravity gradient torque) or incidence angles to obtain the maximum expected error in the torque around each axis. The root mean square (RMS) of this difference does not exceed  $1 \times 10^{-6}$  mNm in roll,  $2 \times 10^{-4}$  mNm in pitch, and  $3 \times 10^{-5}$  mNm in yaw. Comparing these RMS values to the STD values reported in Table 2.6, we find that the effect of uncertainty in the attitude on the residual torque is negligible.

## 2.5. DISCUSSION AND CONCLUSION

In this chapter a set of models was presented that together predict the torque acting on the GOCE satellite, based on its full state (spatial and rotational), the local magnetic field, the currents running through the thruster magnet and magnetic torquers, and the applied thrust force. The accuracy of the result depends heavily on the accuracy of the dominant torque, which is different around each body axis.

In the roll direction errors of 15% are to be expected (in terms of the relative standard deviation, see Table 2.6). The residual torque, as displayed in Figure 2.8a, shows clear periodic patterns that resemble magnetic torques. It is possible that the weighting scheme for the payload dipole estimation (see section 2.3.6) prioritizes the residuals in pitch and yaw torque, because of their larger overall scale.

In pitch the expected errors are smallest, at around 2%. This low number is partially due to the large control torque in this direction, which is meant to balance the (mostly constant) residual dipole of the bus and payloads. The dominant trend in the residual

is caused by an error or noise signal in the current running through the thruster main magnet when thrust is close to the 2mN level. This generally occurs in low density conditions, i.e. early in the mission, mostly over the South Pole in local winter conditions.

The yaw error is largest of the three, with relative standard deviation running up to and over 30%. Throughout the mission the yaw residual is positive over the Northern hemisphere, and negative over the Southern hemisphere. This suggests an error in the neutral density, as the perigee of the (near-circular) orbit lies close to the North Pole. At the same time the North and South magnetic poles show up as bands of large residuals, that increase in magnitude during magnetic storms. This implies that the (effect of) wind is not modeled properly. Together the above two observations leave us to conclude that a mismatch exists between the aerodynamic model from ANGARA and the thermospheric density and wind data derived using a panel model. The errors in the aerodynamic model and thermospheric data together cause most of the residual in the yaw direction.

The current study shows that it is vitally important to have a complete model of the magnetic properties of a satellite, in addition to the aerodynamic models, in order to fully characterize the torques it is subject to. To improve the torque models beyond the level presented here, one would for instance require the magnetic dipole caused by electric currents from the solar panels. Parameters of such a model can be estimated in post processing, as described in section 2.3.6, but a full magnetic characterization before launch would most likely reduce the uncertainty levels. Such a characterization would certainly be needed for future missions that would use both force and torque analyses for the investigation of satellite aerodynamics and thermosphere dynamics, and the absence of such a characterization would be problematic in applying data from current or past missions for this purpose.

We expect that the effect that causes the largest errors in the torque models largely depends on the satellite and mission design. Most LEO satellites are in a significantly higher orbit than GOCE was, reducing the aerodynamic torque and therefore its relevance as an error source. Therefore the magnetic model errors are expected to dominate the residual torque on satellites like GRACE and CHAMP. Both carry magnetic torquers that may have uncertainty margins like those installed on GOCE (see section 2.3.1). As is the case for GOCE, electric currents from solar panels or towards equipment with a high current demand will most likely also show up in the residual torque. For a mission like Swarm, where the satellites are designed to be magnetically clean and there is no continuous thrusting like on GOCE, the solar radiation pressure model could be the main error source. Because of its low sensitivity to model errors, it is unlikely that the gravity gradient torque is a significant source of error for any LEO satellite.

Returning our attention to the GOCE analysis, the aerodynamic signals in the yaw residuals provide an opportunity to improve the aerodynamic model and the thermospheric horizontal wind data. Moreover, comparing Figure 2.8b and 2.8c we observe that a similar signal is present around the North magnetic pole in the pitch residual. This signal may well provide vertical wind data. Our goal for chapter 3 is to extract these wind signals from the residual torque and combine the result with that obtained from the linear accelerations to find a consistent wind data set, and subsequently consistent aerodynamic model parameters in chapter 5.

Recent efforts to obtain angular accelerations from the star tracker attitude quaternions only, so without making use of GOCE's accelerometers, show promising results. In the angular acceleration data derived from the star trackers, the large-scale wind patterns can be observed. Therefore we are considering a similar torque modeling and wind extraction effort for the Swarm satellites, and it would be worth investigating the feasibility of applying such a thermosphere wind extraction processing approach as well to much simpler mission concepts, such as star-tracker carrying CubeSats.

## ACKNOWLEDGEMENTS

The authors would like to thank Rune Floberghagen, Björn Frommknecht and Michael Fehringer at ESA for their help in accessing the GOCE data (access may be requested at <https://earth.esa.int/web/guest/-/goce-data-access-7219>) and documentation (available upon personal request to ESA) used for this research. We also thank NASA's Langley Research Center for maintaining the CERES data, available at <https://ceres.larc.nasa.gov/products.php?product=SYN1deg>.

# 3

## HORIZONTAL AND VERTICAL THERMOSPHERIC CROSS-WIND FROM GOCE LINEAR AND ANGULAR ACCELERATIONS

**T. VISSER, G. MARCH, E. DOORNBOS, C. DE VISSER, and  
P. VISSER**

*Thermospheric wind measurements obtained from linear non-gravitational accelerations of the Gravity field and steady-state Ocean Circulation Explorer (GOCE) satellite show discrepancies when compared to ground-based measurements. In this chapter the cross-wind is derived from both the linear and the angular accelerations using a newly developed iterative algorithm. The two resulting data sets are compared to test the validity of wind derived from angular accelerations and quantify the uncertainty in accelerometer-derived wind data. In general the difference is found to be less than 50 m/s vertically after high-pass filtering, and 100 m/s horizontally. A sensitivity analysis reveals that continuous thrusting is a major source of uncertainty in the torque-derived wind, as are the magnetic properties of the satellite. The energy accommodation coefficient is identified as a particularly promising parameter for improving the consistency of thermospheric cross-wind data sets in the future. The algorithm may be applied to obtain density and cross-wind from other satellite missions that lack accelerometer data, provided the attitude and orbit are known with sufficient accuracy.*

---

This chapter has been published as a paper in *Advances in Space Research* **63**, 10 (2019) ([Visser et al., 2019a](#)).

### 3.1. INTRODUCTION

The purpose of this chapter is to test the possibility of obtaining in situ horizontal and vertical cross-wind estimates from satellite angular accelerations. We do so by presenting a new algorithm that extracts cross-wind from linear or angular accelerations, and applying it to measurements of the Gravity field and steady-state Ocean Circulation Explorer (GOCE). The wind measurements derived from linear and angular accelerations are compared and their sensitivity to model parameters is evaluated.

Although accelerations are an intuitive source for in situ wind observations, it has proven to be difficult to align such measurements with existing knowledge and models, as well as with remote observations such as Fabry–Perot Interferometry (FPI) (*Dhadly et al., 2017, 2018*). Instead of tuning the aerodynamic model of GOCE to match the ground-based observations directly, we may first find a set of model parameters for which the linear and angular acceleration data is internally consistent. This chapter serves to quantify what level of accuracy can be expected from this approach, and to identify the most sensitive model parameters.

The concept of simultaneous atmospheric observations using linear and angular motion of satellites was first adopted in the paddlewheel satellite concept (*Moe, 1966; Pilinski et al., 2011*). For those studies the goal was to measure the absolute thermospheric density. The paddlewheel shape of the satellites ensured that aerodynamic loads would both affect the orbital and the spin motion of the body. In recent years, a number of accelerometer missions have been operated, that presented an opportunity to obtain high resolution density data (*Bruinsma et al., 2004; Doornbos, 2011; Falin et al., 1981; March et al., 2019a; Mehta et al., 2017; Siemes et al., 2016*). The availability of cross-track accelerations has subsequently led to a large amount of horizontal cross-wind data (*Cheng et al., 2008; Doornbos et al., 2010; Sutton et al., 2005*), while the vertical acceleration was generally assumed too small to obtain reliable wind measurements. The horizontal wind data have been used to improve existing models (*Drob et al., 2015*) and to characterize thermospheric waves (*Garcia et al., 2014; Gasperini et al., 2015*) and wind jets (*Liu et al., 2016*). Although an attitude-based algorithm has been proposed by *Virgili-Llop et al. (2018)*, all accelerometer-derived wind measurements have so far been obtained from linear accelerations.

In this work we apply the concept of simultaneous observation of linear and angular motion to a new accelerometer-based method of deriving horizontal and vertical thermospheric cross-wind. In short the approach is as follows. The measured accelerations are used to calculate a ‘measured’ net force and torque acting on the satellite. Models, measurements, and housekeeping data are used to estimate forces and torques caused by solar and Earth radiation pressure and the ion thruster, and torques caused by the gravity gradient, magnetic attitude control, and other magnetic equipment in the satellite. These models for disturbance forces and torques are described extensively by *Doornbos (2011)* and in chapter 2 respectively, and are shown to reflect all significant non-aerodynamic disturbances. The residual force and torque, obtained by subtracting the total model output from the measurement, is therefore assumed to be aerodynamic. An aerodynamic model is made to match this residual by iteratively changing the direction of the incoming flow. The wind is defined as the difference between this new flow direction and the original aerodynamic velocity. The result is a pair of separate wind

data sets, one force-derived and one torque-derived. The difference between these data sets is dominated by an offset. Therefore a second overarching algorithm is used to remove the offset by iteratively changing the thruster misalignment angles and the vertical acceleration bias.

The algorithm presented in this chapter can be applied to any mission for which detailed knowledge is available of either the linear or angular accelerations, or an appropriate combination thereof. It can therefore, in itself, contribute to an increase in the amount of missions deemed suitable for wind estimation. For example, the angular accelerations may be obtained from precise attitude measurements and the along-track acceleration from the orbital motion. In the GOCE case the algorithm results in two separate cross-wind data sets, one derived from linear accelerations (force-derived), the other from angular accelerations (torque-derived). By comparing the two, we identify the major error sources in accelerometer-derived wind, and quantify their impact on the wind measurements. We formulate recommendations for ground testing campaigns, operations, and documentation of future low-Earth-orbiting, accelerometer-carrying satellite missions to improve the consistency of future wind data sets.

The chapter is structured as follows. First, in section 3.2, we present the data sets used as inputs and highlight the changes that were made to earlier (published) versions of the force and torque models. Then the methodology is presented in section 3.3. The majority of this section is dedicated to the explanation of the algorithm with which the cross-wind is obtained from residual forces and torques. In section 3.4, the resulting data sets are presented and compared, and their sensitivity to measurement errors and model parameters is evaluated in section 3.5. Finally, in section 3.6, conclusions are drawn regarding the consistency of accelerometer-derived cross-wind data and the value of simultaneous wind estimation from linear and angular accelerations.

## 3.2. GOCE FORCE AND TORQUE MODELS

The goal of the European Space Agency (ESA) GOCE mission was to map Earth's gravity field in unprecedented spatial detail. The satellite was in a near-Sun-synchronous, near-circular dusk-dawn orbit with an inclination of  $96.7^\circ$ . Starting at a mean altitude of 260 km at the start of the science mission in November 2009, the orbit was gradually lowered from August 2012 onwards to 229 km at the end of the mission in November 2013. An ion engine providing continuous thrust was used to create a drag-free measurement environment.

To achieve its mission objective, GOCE was equipped with a gradiometer consisting of six accelerometers positioned on the three principle axes of the satellite body, each measuring the linear acceleration along all three principle axes. The resulting 18 accelerations can be combined in specific ways to obtain the gravity gradients. By taking different combinations of the individual acceleration measurements, the linear and angular non-gravitational accelerations of the satellite body are found (*Siemes et al., 2012; Stummer, 2012*). The resulting data products are used in this work to derive the in situ thermospheric wind. The low orbit required for the mission results in a large aerodynamic signal. We will show in section 3.4 that this even allows for vertical wind measurements on the heavily controlled pitch axis.

Even though the aerodynamic signal is large, accurate models of all other major dis-

turbance forces and torques are required. In terms of forces this amounts to modeling the thrust, and solar, Earth albedo, and infrared radiation pressure. The first is provided as part of the housekeeping data in terms of the commanded thrust. We use the thrust command instead of the achieved thrust as it is more smooth ([Wallace et al., 2011](#)), making it more representative of the ten second intervals at which we sample the data. The latter is derived from the position of the Sun and Earth with respect to the satellite, and using ANGARA force coefficients ([Doornbos \(2011\)](#) or chapter 2 of this thesis). The sum of the models is compared to the ‘measured’ force, defined as the product of the interpolated mass of the satellite, and calibrated linear accelerations obtained through the method of [Visser and van den IJssel \(2016\)](#).

In terms of the torques a total of five different disturbances are modeled, namely the thruster misalignment, solar, Earth albedo and infrared radiation pressure (using ANGARA torque coefficients), gravity gradient, attitude control, and magnetic torques. These models are described and validated in chapter 2. The ‘measured’ torque, eclipse transition model, and the aerodynamic model have however been updated. First, instead of calibrating the EGG\_CGA (Electrostatic Gravity Gradiometer - Calibrated Gradiometer Angular accelerations) product, the ‘measured’ torque is calculated entirely from the EGG\_GAR (Gradiometer Angular Rate) product ([Stummer, 2012](#), section 6.2). The angular acceleration is derived from this product by taking the eight point central difference of the original 1Hz signal. The result is interpolated on a 0.1Hz signal, as are all other data. Second, we replaced the geometric eclipse model by a parametrization of the physics-based SOLAARS model of [Robertson et al. \(2015\)](#). The parametrization, described in detail in section 3.7 of [Robertson \(2015\)](#), assumes a standard atmosphere, global average cloud top height, and fixed aerosol profile. Third, we use NRLMSISE-00 densities ([Picone et al., 2002](#)) and no wind data or model to calculate the initial aerodynamic torque, to completely decouple linear and angular accelerations. Only the payload magnetic dipoles are affected by this change, as they are re-estimated using the new set of models. Fourth, the aerodynamic coefficients are obtained from a new high-fidelity geometry and aerodynamic model of GOCE using the rarefied gas simulator SPARTA ([Gallis et al., 2014](#)). This model is described in detail and compared to other existing models by [March et al. \(2019a\)](#). We assume fully diffusive reflection with energy accommodation coefficient 0.93, in line with [Sutton \(2009\)](#). The energy accommodation coefficient  $\alpha_E$  is defined e.g. in Equation (2) of [March et al. \(2019a\)](#), as a function of incoming and re-emitted particle temperatures, and satellite wall temperature. The proper value of the accommodation coefficient is the subject of ongoing research (e.g., [Mehta et al. \(2013\)](#); [Moe and Moe \(2005\)](#); [Pilinski et al. \(2010, 2013\)](#); [Walker et al. \(2014a,b\)](#)). The influence of this parameter on the wind data is elaborated on in section 3.5, and more extensively in chapter 5.

Since the publication of the GOCE torque models, the scientific data of the mission have been reprocessed to account for the quadratic calibration term of the accelerometers ([Siemes, 2018](#)). This reprocessing had no significant effect on the measured and modeled forces and torques. Only small changes were found in magnetometer calibration parameters and estimated magnetic dipoles. The reprocessed data is used for all results shown in this chapter.

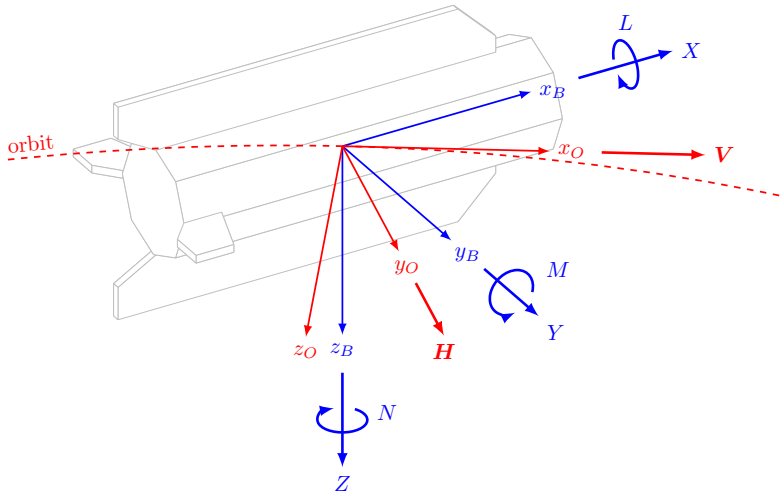


Figure 3.1: Definition of the force and torque components in the body (B) frame, and of the local orbit (O) frame based on the inertial velocity  $V$  and orbital angular momentum  $H$ .

### 3.3. METHODOLOGY

In this section we present a new algorithm that can be used to derive both horizontal and vertical cross-wind from both linear and angular accelerations. Because torques are more intuitive to work with than angular accelerations, the algorithm is set up to work with forces and torques instead. Describing forces and torques as vectors, any combination of force and torque components can be used as input. The components are defined in the body (B) frame, as displayed in Figure 3.1. In our experience, the horizontal cross-wind is observed both in the lateral body force ( $Y$ ) and the yaw torque ( $N$ ); the vertical wind affects both the vertical force ( $Z$ ) and the pitch torque ( $M$ ); the density primarily affects the longitudinal force ( $X$ ). In roll ( $L$ ) the aerodynamic torques are too small to yield a valuable wind or density measurement. In the remainder of this chapter we mean by torque-derived wind, wind derived from longitudinal force, and pitch and yaw torques ( $X, M, N$ ).

The residual forces and torques are obtained by reducing the measured forces and torques by modeled disturbances, as discussed in section 3.2. It was found that when forces and torques are mixed, scaling of the residuals is required to prevent a bias towards the force residual. Based on the mean and standard deviation of the force and torque residuals, a scale of 10 was selected to increase the weight of the torque residual. In the remainder of this section we discuss the algorithm in terms of torques only. The process is exactly the same for forces.

The algorithm is an implementation of Newton's root-finding method using numerical derivatives, and generalizes the algorithm of [Doornbos et al. \(2010\)](#) to the full-dimensional case. Each iteration consists of six steps, as presented in Figure 3.2 and outlined below. It is initialized with the orbital velocity including co-rotation of the atmosphere and densities obtained from NRLMSISE-00.

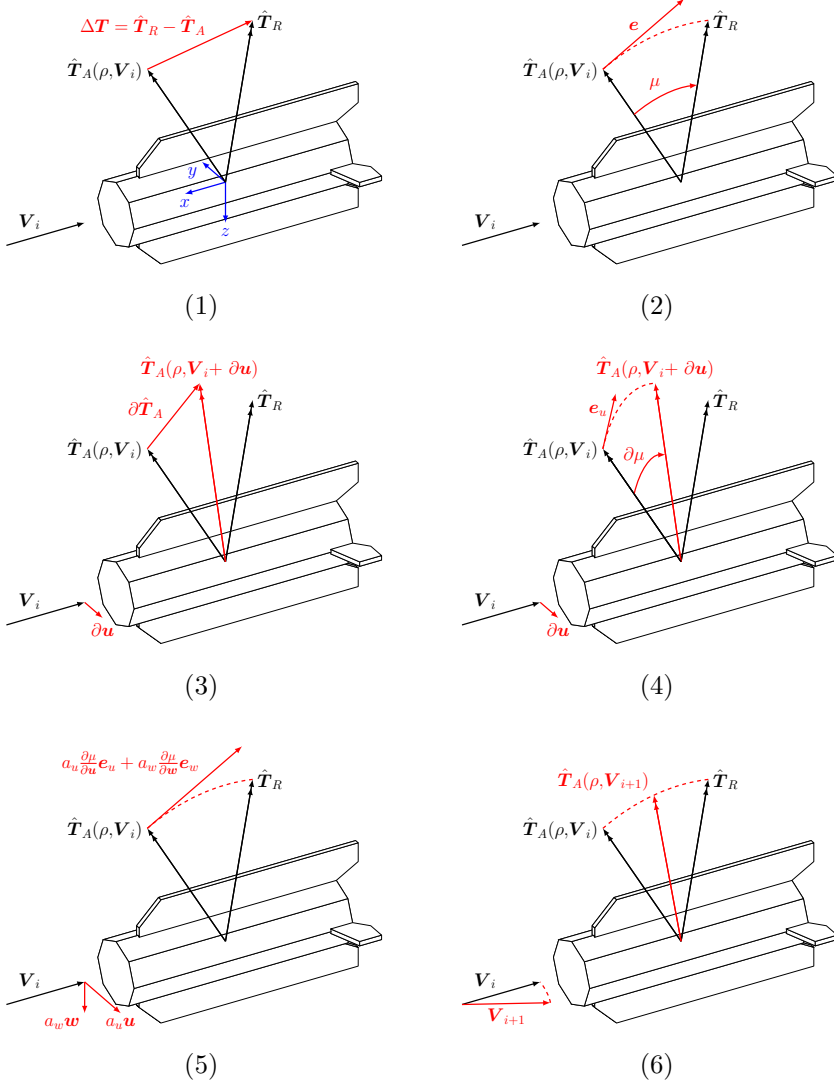


Figure 3.2: Schematic overview of the six steps of the algorithm to determine the wind from the torque measurements and models. The same algorithm is applied to derive wind from measured and modeled force. Note that direction vectors  $e$  and normalized torques (indicated with a hat) are drawn with different lengths to improve the clarity of the figure.

1. Based on the (initial) aerodynamic velocity  $V_i$  the aerodynamic torque is calculated using Equation (2.4) (or Equation (3.6) of *Doornbos (2011)* for the force equivalent). Both the aerodynamic  $T_A$  and residual torque  $T_R$  are normalized to  $\hat{T}_A$  and  $\hat{T}_R$ , and the error  $\Delta T$  between the two is found.
2. The direction error is converted to an angle  $\mu$  between the two torques, and the direction vector  $\mathbf{e}$ . The latter is defined as the vector perpendicular to  $\hat{T}_A$ , tangential to the great circle through  $\hat{T}_A$  and  $\hat{T}_R$ , centered at the center of mass of the satellite.
3. Using the Gram–Schmidt method, two directions  $\mathbf{u}$  and  $\mathbf{w}$  perpendicular to the current aerodynamic velocity are found. Small perturbations are made to the velocity in those directions (only drawn for  $\mathbf{u}$  in Figure 3.2) and the aerodynamic torque is recalculated and normalized.
4. The changes in aerodynamic torque direction  $\partial\hat{T}_A$  due to these velocity variations are decomposed into an angle  $\partial\mu$  and the tangential  $\mathbf{e}_u$  along the great circle through the old and new aerodynamic torque. Dividing the angle increment by the change in velocity we find approximate derivatives of these angles.
5. The derivatives are collected in a Jacobian matrix, after which the linearized system

$$\mu\mathbf{e} = \begin{bmatrix} \frac{\partial\mu}{\partial\mathbf{u}}\mathbf{e}_u & \frac{\partial\mu}{\partial\mathbf{w}}\mathbf{e}_w \end{bmatrix} \begin{pmatrix} a_u \\ a_w \end{pmatrix} \quad (3.1)$$

is solved for the velocity components  $a_u$  and  $a_w$  in a weighted least squares sense. The weights are chosen to be the inverse standard deviation of the measured torque components.

6. The velocity updates  $a_u$  and  $a_w$  are scaled with a learning rate  $\gamma_i$  before they are applied to their respective velocity update vectors  $\mathbf{u}$  and  $\mathbf{w}$ . The learning rate gradually increases as  $\gamma_i = \min\{0.1 + i/10, 0.9\}$ , with  $i$  the iteration counter. The velocity is normalized to its original magnitude.

The algorithm normally converges in 10 iterations, using a maximum angle error  $\max(\mu) < 1''$  as the stopping criterion. The wind is defined as the difference between the final aerodynamic velocity and the initial (orbital plus co-rotation) velocity. After convergence, a separate scale factor is calculated for the density at each time instant, by taking the ratio of the magnitudes of the aerodynamic and residual torque vectors.

The total (three-dimensional) wind measurements are rotated from the body (B) frame (in which they are derived, defined in blue in Figure 3.1) to the local orbit (O) frame (red in Figure 3.1). The horizontal cross-wind is thus defined along the orbital angular momentum vector, and the vertical wind in the nadir direction perpendicular to both the inertial velocity and orbital angular momentum vectors. The differences between the O- and B-frame are minimal, except for a rotation of  $180^\circ$  around the longitudinal axis. This ensures that positive vertical wind is upward. The combination of the dusk–dawn orbit configuration and the flow from the day- to the night-side of the Earth results in a predominantly negative horizontal wind in this frame.

The algorithm can only provide us with the direction of the incoming flow, not its magnitude. This implies that the wind component in the direction of the incoming flow

cannot be isolated from the density estimate. By studying the wind in the orbit frame we reduce one component of the wind estimate (along-track in this case) to a minimum, while at the same time being independent of the wind direction or satellite attitude for its definition. In theory the algorithm could estimate the magnitude of the incoming flow if four or more force and torque components are combined. In practice, however, the aerodynamic force and torque models are not linearly independent in their response to flow incidence angles.

Applying the above algorithm to the entire GOCE mission, we found a strong bias towards upward wind, and an offset between cross-wind components derived from forces and those derived from torques. From the sensitivity analysis (discussed in detail in section 3.5) it was concluded that both could be explained by a small adjustment of both the vertical acceleration bias and the thruster misalignment angles. Therefore these parameters were estimated with an overarching algorithm. First, the partial derivatives of the force-derived and torque-derived wind with respect to the parameters is found from the forward difference. Then, assuming the wind is linear in the parameters, we solve for the bias and thruster angles. Finally, we estimate a single value for the bias and thruster angles for a full day of data, such that the force-derived vertical wind and the difference between force-derived and torque-derived wind (both horizontal and vertical) are minimized in a least squares sense. The influence of the energy accommodation coefficient on these estimates will be the subject of chapter 5.

The thrust angles are defined as displayed in Figure 3.3, such that the unit thrust vector  $\hat{F}_T$  is found as

$$\hat{F}_T = \begin{pmatrix} \cos \alpha \cos \beta \\ \sin \beta \\ \sin \alpha \cos \beta \end{pmatrix} \quad (3.2)$$

in the body frame. The algorithm is run for each day resulting in the daily estimates of the angles plotted in Figure 3.4. While the  $\alpha$  estimates are centered around the documented value, the  $\beta$  estimates assume an opposing sign. This is most likely due to the fact that the spacecraft layout had to be inverted, to match the change in the target orbit orientation when the launch was postponed. The documentation may be describing the initially intended spacecraft configuration, rather than the one that was flown. Four linear trends have been estimated for the thrust angles as a function of mean thrust level, in accordance with the documentation (*Kolkmeier et al., 2008*, see Table 6.6-2). They are plotted in the same figure, and listed in Table 3.1. The episodes were chosen based on visual inspection of Figure 3.4, and constitute the time before and after August 2012 respectively, as well as the months August and November of 2012. These two months deviate from the nominal mission because of significant orbit lowering operations (*GOCE Flight Control Team (HSO-OEG), 2014*). To remove outliers, the weighted sum of the square distance from the fit in  $\alpha$  (unit weight) and  $\beta$  (weighted ten to account for larger spread in the  $\alpha$  estimates) was calculated. The data point with the highest sum was removed, after which the linear fits were re-estimated. This process was repeated 20 times for the first nominal mission phase, four times for the second, and two times for both maneuvers, resulting in a total of 28 outliers being removed. The values in Table 3.1 and lines in Figure 3.4 reflect the final result. Although the parameterization is based on the

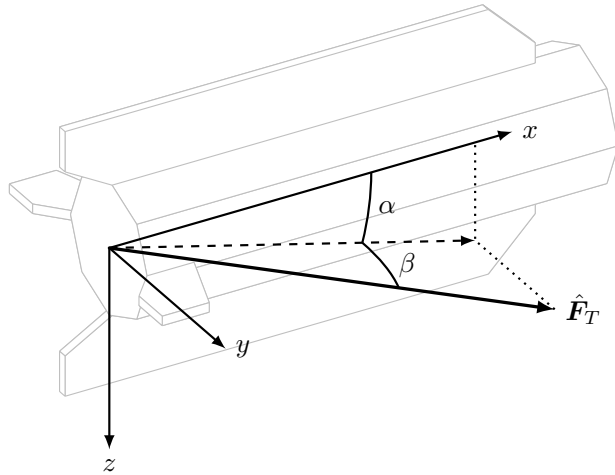


Figure 3.3: Definition of the thrust angles  $\alpha$  and  $\beta$  for the unit thrust vector  $\hat{\mathbf{F}}_T$  in the satellite body frame (translated to the thrust application point for clarity), with  $z$  nadir pointing.

Table 3.1: Linear parameterizations of the thrust angles  $\alpha$  and  $\beta$  in terms of the thrust level.

| Time period                          | Thrust $\alpha$ [deg, deg/N] |        | Thrust $\beta$ [deg, deg/N] |         |
|--------------------------------------|------------------------------|--------|-----------------------------|---------|
|                                      | Constant                     | Linear | Constant                    | Linear  |
| 2009-11-01 – 2012-07-31              | -2.17                        | 26.14  | -0.01                       | 33.88   |
| 2012-08-01 – 2012-08-31              | -2.23                        | 63.04  | 0.64                        | -104.99 |
| 2012-09-01 – 2012-10-31 <sup>a</sup> | -2.07                        | 12.03  | 0.09                        | 11.83   |
| 2012-11-01 – 2012-12-02              | -2.13                        | 23.68  | 0.35                        | -12.90  |
| 2012-12-03 – 2013-09-30 <sup>a</sup> | -2.07                        | 12.03  | 0.09                        | 11.83   |

<sup>a</sup> These episodes were merged to find a single parameterization.

daily mean thrust level, the angles are calculated using the instantaneous thrust in the updated force and torque models.

The daily vertical acceleration bias estimates are plotted alongside the estimates from orbit determination (using the method of [Visser and van den IJssel \(2016\)](#) and the reprocessed GOCE data) in Figure 3.5, and the linear fit parameters are listed in Table 3.2. Note that the wind-based estimates are significantly more consistent than the orbit-based ones. Bias estimates below  $-43 \text{ nm/s}^2$  and above  $-20 \text{ nm/s}^2$  (17% of the data points, mostly days with a lack of data) are removed before four linear trends in time are estimated. Instead of isolating the November 2012 orbit maneuver, the early part of the mission (before the summer 2010 anomaly ([GOCE Flight Control Team \(HSO-OEG\), 2014](#))) is treated separately. The spread in the bias is larger for this part of the mission because of low solar activity and the resulting small aerodynamic force and torque, allowing for errors in other models to become more dominant in the derived wind.

Using the linear parameterizations for the thruster angles and the acceleration bias, the thrust force and moment and the measured force are recalculated. Then the residual torque and the payload dipole estimates are updated. The updated models serve as

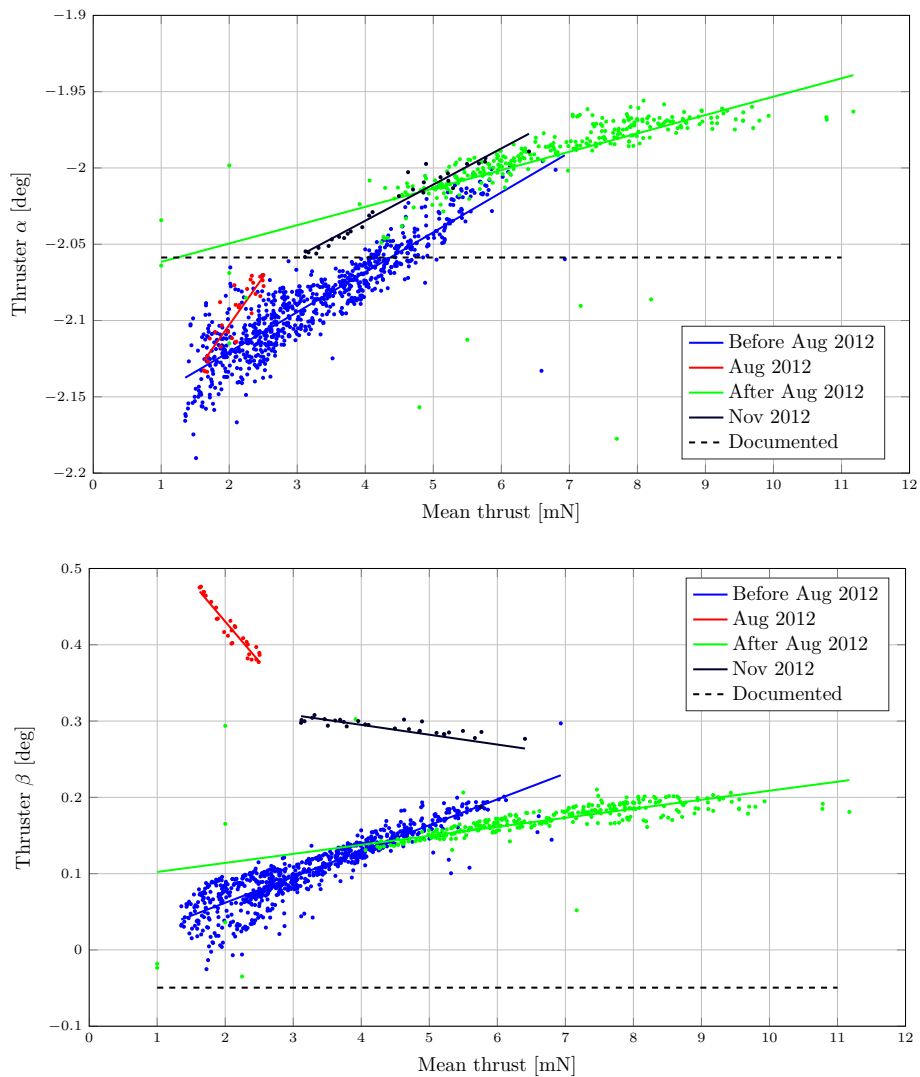


Figure 3.4: Daily thrust  $\alpha$  (top) and  $\beta$  (bottom) estimates as a function of daily mean thrust.

Table 3.2: Linear parameterizations of the wind-derived vertical acceleration bias as a function of time. Time is measured in days since the start of the episode.

| Time period             | Constant [nm/s <sup>2</sup> ] | Linear [nm/s <sup>2</sup> /day] |
|-------------------------|-------------------------------|---------------------------------|
| 2009-11-01 – 2010-07-31 | -36.48                        | -0.0066                         |
| 2010-08-01 – 2012-07-31 | -34.86                        | 0.0037                          |
| 2012-08-01 – 2012-08-31 | -35.63                        | 0.0591                          |
| 2012-09-01 – 2013-09-30 | -31.18                        | 0.0169                          |

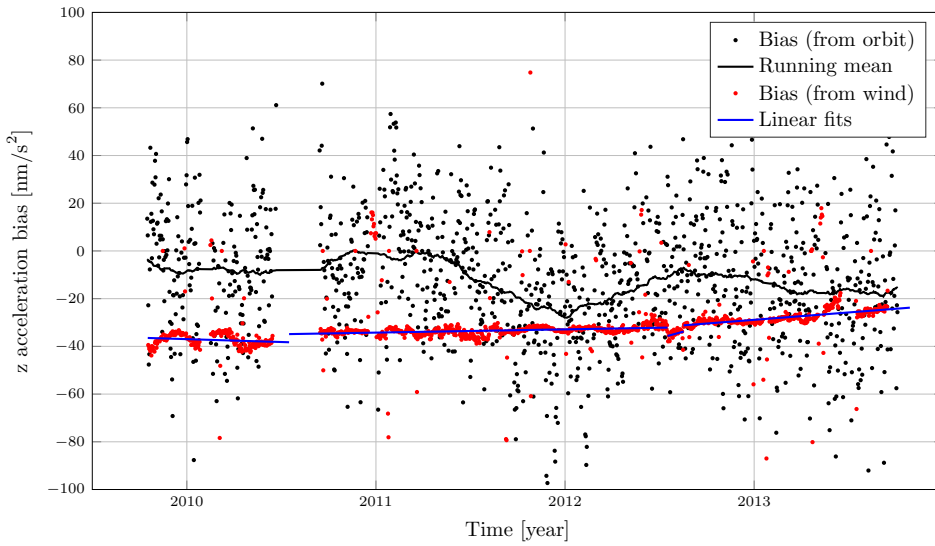


Figure 3.5: Daily wind-derived vertical acceleration bias estimates as a function of time along with the linear parameterizations, compared to orbit-derived biases.

inputs to the wind algorithm described above to obtain the force-derived and torque-derived cross-wind data sets.

### 3.4. RESULTS

A total of four data sets result from the aforementioned approach: horizontal and vertical cross-wind derived from forces or torques. Because force modeling is significantly less complex than torque modeling, we take the force-derived wind as reference. This assumption allows us to evaluate the quality of the torque-derived wind. The validity of the horizontal force-derived wind is discussed by *Dhadly et al. (2017, 2018)* in a comparison with other wind observations.

A complete mission overview of the horizontal wind is plotted in Figure 3.6. It shows the dependence of the horizontal wind on the argument of latitude, i.e. the progress through the orbit in degrees starting from the ascending node. The areas around the magnetic poles (around  $90^\circ$  argument of latitude for the North pole and  $270^\circ$  for the South pole) are visible as regions of increased wind and wind reversal. The dominant negative sign of the horizontal wind indicates a net flow from the day to the night side of the Earth, as should be expected. A seasonal trend is observed in the form of increased wind magnitude in the dawn sector ( $90^\circ$  to  $270^\circ$  argument of latitude) of the summer hemisphere and the dusk sector of the winter hemisphere. Finally, combining the wind plots with the eclipse function in Figure 3.7, a decrease in wind activity is revealed in the polar regions during eclipse, as compared to full sunlit conditions.

The difference between the two data sets, plotted in the bottom panel of Figure 3.6, reveals two main patterns. First is a difference between the two hemispheres. This pat-

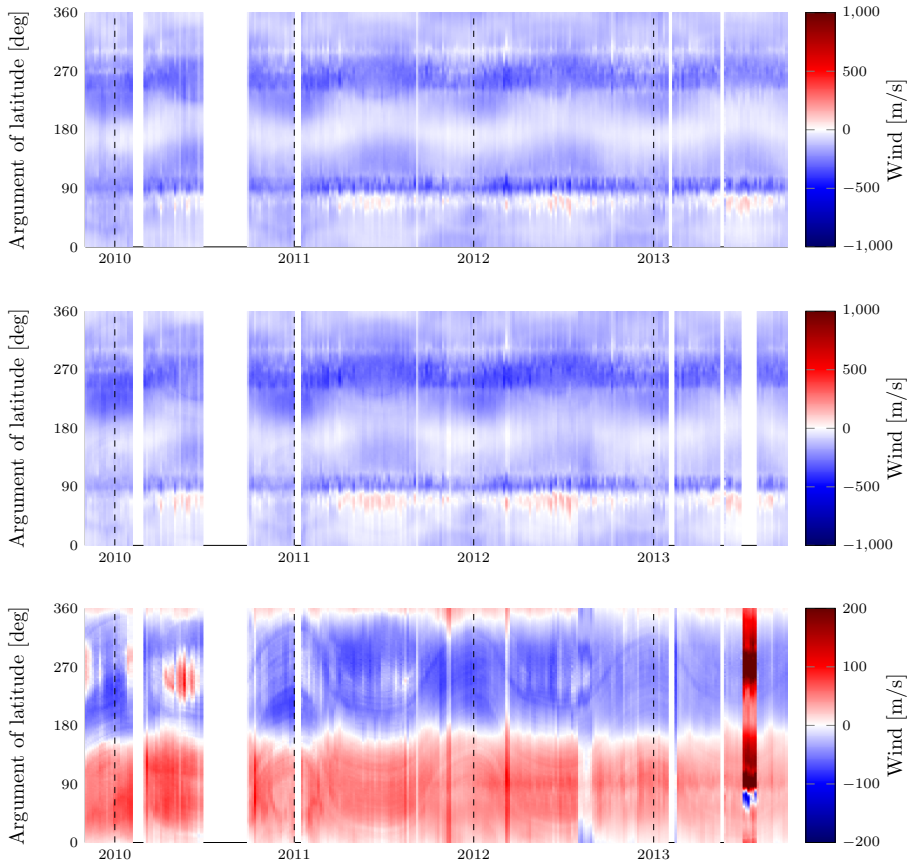


Figure 3.6: Horizontal wind derived from forces (top) and torques (middle), and the difference between the two (bottom), for the full mission. Note the difference in color scales.

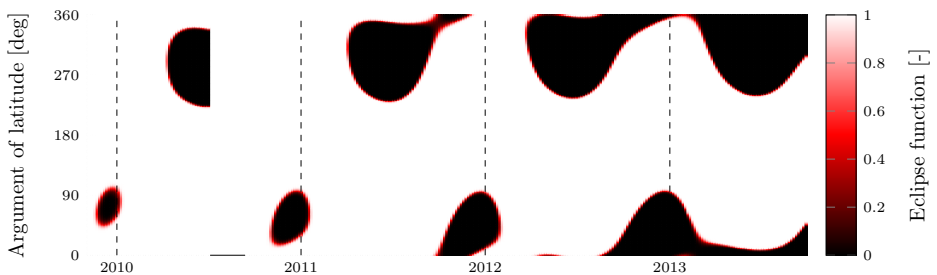


Figure 3.7: Eclipse function (0 in eclipse, 1 in full sunlight) for the full mission, as a function of time and argument of latitude.

Table 3.3: Mean ( $\mu$ ) and standard deviation ( $\sigma$ ) of force- and torque-derived wind, and of the difference between the two.

|                | Horizontal [m/s]     | Vertical [m/s]    |
|----------------|----------------------|-------------------|
|                | $\mu \pm \sigma$     | $\mu \pm \sigma$  |
| Force-derived  | $-128.81 \pm 103.24$ | $1.91 \pm 11.56$  |
| Torque-derived | $-127.35 \pm 112.15$ | $12.13 \pm 70.04$ |
| Difference     | $1.48 \pm 49.69$     | $10.21 \pm 67.85$ |

tern closely follows the vertical component of the Earth's magnetic field. It could be explained by an electric dipole on the satellite in the order of  $10^{-5}$  Cm, but no source for a sufficiently large charge has been identified so far. The second pattern takes the form of a group of once per year oscillations in argument of latitude. It follows the eclipse pattern observed in Figure 3.7, implying a relation with the sunlight incidence angle. The pattern disappears inside eclipse. This error may be caused by errors in the solar radiation pressure modeling or by the unmodeled magnetic effect of currents from the solar panels, but no complete explanation has been found so far. The horizontal cross-wind data sets are compared in terms of their mean and standard deviation in Table 3.3. The difference between the two data sets is generally smaller than 100 m/s.

The same overview is plotted for the vertical wind in Figure 3.8. The force-derived vertical wind (top panel) reveals a small consistent upward wind on the Northern hemisphere, and a small downward wind on the Southern hemisphere. The main feature however is a large amount of short-lived, small-scale peaks in the auroral zones and over the polar caps. This is consistent with previous vertical wind observations (*Innis and Conde, 2002; Smith, 1998*). A detailed comparison with other satellite observations will be the subject of chapter 4.

The discrepancy between the two vertical wind data sets is significantly larger. This is illustrated by the similarity of the torque-derived data (middle panel) to the difference (bottom panel), which is also reflected in the mean and standard deviation in Table 3.3. The largest errors in the torque-derived wind are found around the South pole (apogee) in local winter, especially early in the mission (at low solar activity); i.e. when density is low. These errors are caused by erratic behavior of the thruster at low thrust levels that is lost in the down-sampling of the data. Despite our efforts to remove any bias from the vertical wind, the mean value over the first half of 2010 remains 9 m/s upward. This may be explained by the low quality of the linear fit to the acceleration bias in Figure 3.5 in this time frame. The eclipse transition patterns of Figure 3.7 are clearly visible in the torque-derived vertical wind, confirming the errors related to solar radiation or solar panel currents mentioned above.

As vertical wind is generally characterized by short-lived, small-scale peaks, it is worthwhile to compare the two data sets in terms of their high frequencies only. Through trial and error we found that at frequencies above ten times orbital frequency (periods shorter than 9 minutes, spatial scales smaller than 4000 km), the two data sets show striking similarities. This is shown in Figure 3.9, where the two data sets and their difference are plotted from 11:25 to 11:50 UTC on 17 March 2013, after passing them through a high-pass third-order Butterworth filter rejecting frequencies below ten times the orbital frequency. The difference is reduced to less than 50 m/s for wind values up to 200 m/s,

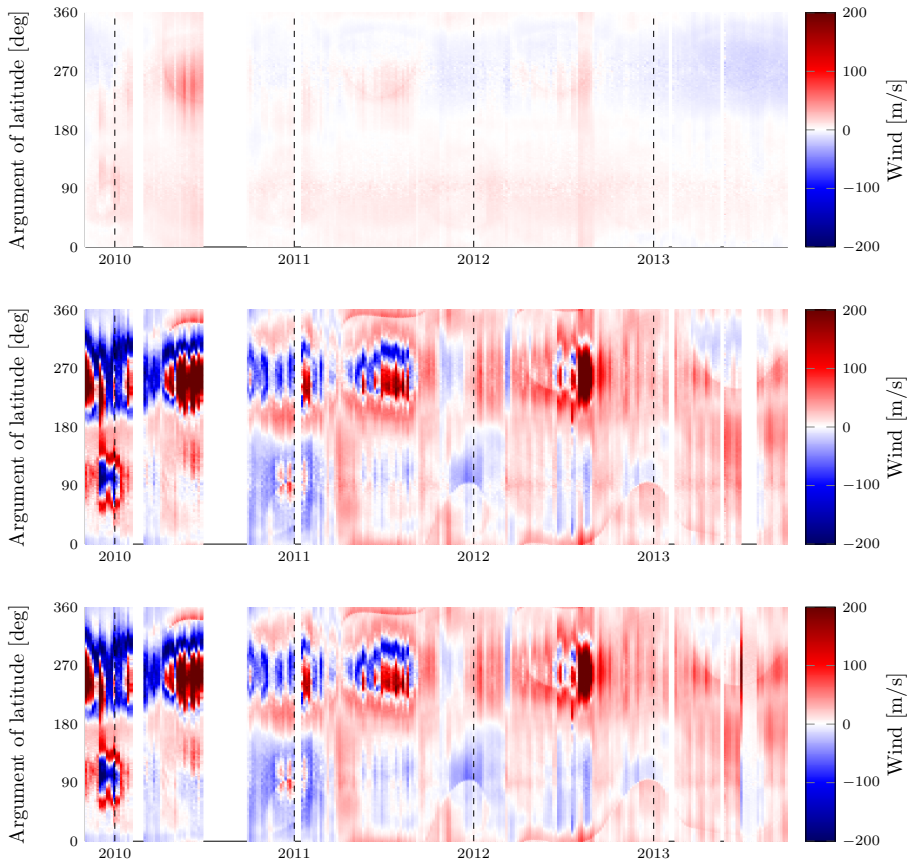


Figure 3.8: Vertical wind derived from forces (top) and torques (middle), and the difference between the two (bottom), for the full mission.

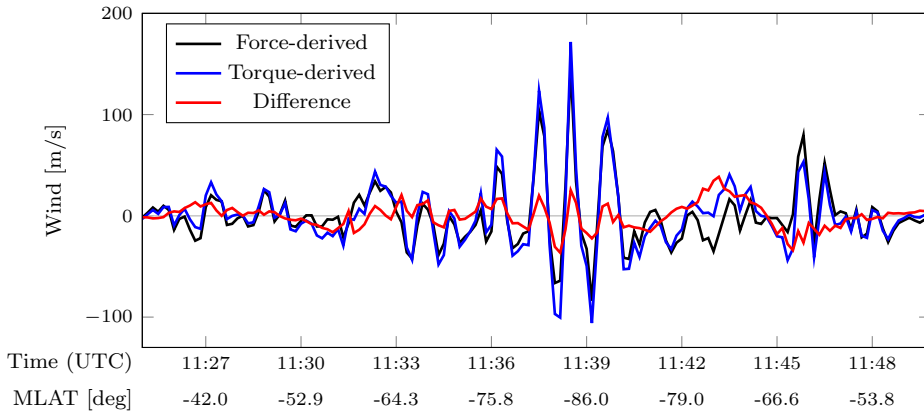


Figure 3.9: Time series of strong vertical wind peaks on 17 March 2013 over the South pole. Both force- and torque-derived wind are high-pass filtered to reveal their similarity above ten times the orbital frequency. Magnetic latitude (MLAT) is added for reference.

and a strong correlation is revealed between the force- and torque-derived data.

### 3.5. SENSITIVITY ANALYSIS

As the algorithm output is affected by model parameters and measurement errors, the sensitivity of the wind data is evaluated for both. Uncertainty values are applied as constant positive offsets from the nominal case, except for the accommodation coefficient, which replaces the default value of 0.93. Using the new parameter value the modeled and measured force and torque are calculated anew for March 2013. This month is representative of the complete data set, but because of the lower altitude, medium-high solar activity, and equinox conditions, it lacks many of the systematic errors described in the previous section. Note that the affected torque replaces the old version in the notch-filtered residual torque (as per the terminology and methodology used in chapter 2) without applying the notch filter to the new residual or estimating the payload dipoles again. The newly found residual force and torque are used as inputs to the wind algorithm in section 3.3 (Figure 3.2) to find the new thermospheric wind. The sensitivity is expressed as the mean ( $\mu$ ) and standard deviation ( $\sigma$ ) of the difference between the newly derived and the nominal wind. These values are calculated per wind direction (horizontal and vertical) and source data (forces  $F$  or torques  $T$ ). Parameters that constitute a full  $3 \times 3$  matrix (moment of inertia, magnetometer scale factor, control dipole scale factor, soft magnetic dipole) are only changed along the diagonal.

All measurements considered here are listed in Table 3.4. The uncertainty levels of the mass, inertia, and center of mass (CoM) are taken from the numerical precision in the GOCE Mass Properties file. For the vertical acceleration we use the root mean square error of the fit in Figure 3.5 instead of the standard deviation of the orbit-derived estimates. The uncertainty in angular acceleration is obtained from the bias estimates of chapter 2, even though we no longer use those accelerations, and our current error is

Table 3.4: Sensitivity of force-derived ( $F$ ) and torque-derived ( $T$ ) cross-wind to measurement errors, in terms of the mean ( $\mu$ ) and standard deviation ( $\sigma$ ) of the change in wind in response to those errors, evaluated for March 2013.

| Parameter                          | Value               | Horizontal [m/s]     |                      | Vertical [m/s]       |                      |
|------------------------------------|---------------------|----------------------|----------------------|----------------------|----------------------|
|                                    |                     | $\mu_F \pm \sigma_F$ | $\mu_T \pm \sigma_T$ | $\mu_F \pm \sigma_F$ | $\mu_T \pm \sigma_T$ |
| CoM shift x [mm]                   | 0.5 <sup>a</sup>    | (-)±(-)              | 0.12±0.19            | (-)±(-)              | -0.34±0.05           |
| CoM shift y [mm]                   | 0.5 <sup>a</sup>    | (-)±(-)              | -0.00±0.00           | (-)±(-)              | -0.00±0.00           |
| CoM shift z [mm]                   | 0.5 <sup>a</sup>    | (-)±(-)              | 0.00±0.00            | (-)±(-)              | -0.00±0.00           |
| Roll bias [arcsec]                 | 3 <sup>b</sup>      | -0.00±0.00           | 0.00±0.01            | 0.00±0.00            | 0.00±0.00            |
| Pitch bias [arcsec]                | 3 <sup>b</sup>      | -0.00±0.00           | -0.00±0.00           | -0.11±0.00           | 0.31±0.15            |
| Yaw bias [arcsec]                  | 3 <sup>b</sup>      | 0.11±0.00            | 0.11±0.00            | -0.00±0.00           | 0.00±0.00            |
| Inertia x [kgm <sup>2</sup> ]      | 0.05 <sup>a</sup>   | (-)±(-)              | 0.00±0.00            | (-)±(-)              | -0.00±0.00           |
| Inertia y [kgm <sup>2</sup> ]      | 0.05 <sup>a</sup>   | (-)±(-)              | -0.00±0.00           | (-)±(-)              | -0.00±0.00           |
| Inertia z [kgm <sup>2</sup> ]      | 0.05 <sup>a</sup>   | (-)±(-)              | 0.00±0.01            | (-)±(-)              | 0.00±0.00            |
| Mass [kg]                          | 0.0005 <sup>a</sup> | -0.00±0.00           | (-)±(-)              | 0.00±0.00            | (-)±(-)              |
| Lin. acc. x [nm/s <sup>2</sup> ]   | 0.3 <sup>c</sup>    | -0.00±0.01           | (-)±(-)              | 0.00±0.00            | (-)±(-)              |
| Lin. acc. y [nm/s <sup>2</sup> ]   | 7 <sup>c</sup>      | -4.31±1.46           | (-)±(-)              | 0.02±0.03            | (-)±(-)              |
| Lin. acc. z [nm/s <sup>2</sup> ]   | 3 <sup>d</sup>      | -0.01±0.02           | (-)±(-)              | -2.79±0.93           | (-)±(-)              |
| Ang. rate x [nrad/s]               | 10 <sup>b</sup>     | (-)±(-)              | -0.05±0.02           | (-)±(-)              | 0.00±0.00            |
| Ang. rate y [nrad/s]               | 10 <sup>b</sup>     | (-)±(-)              | 0.00±0.00            | (-)±(-)              | -0.00±0.00           |
| Ang. rate z [nrad/s]               | 10 <sup>b</sup>     | (-)±(-)              | -0.00±0.00           | (-)±(-)              | 0.00±0.00            |
| Ang. acc. x [nrad/s <sup>2</sup> ] | 4.2 <sup>e</sup>    | (-)±(-)              | -0.01±0.01           | (-)±(-)              | -0.24±0.08           |
| Ang. acc. y [nrad/s <sup>2</sup> ] | 0.29 <sup>e</sup>   | (-)±(-)              | 0.00±0.02            | (-)±(-)              | -2.23±0.77           |
| Ang. acc. z [nrad/s <sup>2</sup> ] | 4 <sup>e</sup>      | (-)±(-)              | 18.91±6.50           | (-)±(-)              | -0.49±0.34           |
| Magn. scale x [%]                  | 0.1 <sup>e</sup>    | (-)±(-)              | -0.00±0.03           | (-)±(-)              | -0.02±0.15           |
| Magn. scale y [%]                  | 0.1 <sup>e</sup>    | (-)±(-)              | -0.00±0.06           | (-)±(-)              | 0.00±0.01            |
| Magn. scale z [%]                  | 0.1 <sup>e</sup>    | (-)±(-)              | 0.00±0.00            | (-)±(-)              | -0.01±0.46           |

<sup>a</sup> Numerical precision in GOCE Mass Properties file.

<sup>b</sup> [Stummer \(2012\)](#).

<sup>c</sup> [Visser and van den IJssel \(2016\)](#).

<sup>d</sup> Root mean square error of fit, this chapter.

<sup>e</sup> Root mean square error of fit, chapter 2.

likely smaller. The root mean square error of the fit to the magnetometer scale factor estimates in Figure 2.3 is used as the magnetic field error.

For the model parameter uncertainties in Table 3.5 we extensively use the root mean square error of linear fits, either presented in this chapter or in chapter 2. Exceptions are the thrust offset and thrust level that were taken from documentation, and the aerodynamic parameters (accommodation coefficients, specular fraction, atmospheric and wall temperature, and flow speed) that were chosen based on existing knowledge. A wide range of accommodation coefficients is considered, as its value is widely debated. The specular fraction is generally expected to be small, in the order of a few percent ([Gregory and Peters, 1987](#)). The temperature deviations were chosen significantly larger than to be expected. With flow speed we mean the magnitude of the velocity vector. Since this magnitude is kept constant in the cross-wind algorithm, this effectively reflects a constant along-track (meridional) head-wind of 200 m/s.

More than half of the parameters listed in Tables 3.4 and 3.5 affect only the torque-derived wind. On top of that the thrust angles produce significantly larger offsets in torque-derived wind than in their force-derived counterparts. This confirms our hy-

Table 3.5: Sensitivity of force-derived ( $F$ ) and torque-derived ( $T$ ) cross-wind to model parameters, in terms of the mean ( $\mu$ ) and standard deviation ( $\sigma$ ) of the change in wind in response to changing those parameters, evaluated for March 2013.

| Parameter                          | Value              | Horizontal [m/s]     |                      | Vertical [m/s]       |                      |
|------------------------------------|--------------------|----------------------|----------------------|----------------------|----------------------|
|                                    |                    | $\mu_F \pm \sigma_F$ | $\mu_T \pm \sigma_T$ | $\mu_F \pm \sigma_F$ | $\mu_T \pm \sigma_T$ |
| Thrust offset x [mm]               | 1.6 <sup>a</sup>   | (-)±(-)              | -0.05±0.01           | (-)±(-)              | 0.96±0.03            |
| Thrust offset y [mm]               | 1.6 <sup>a</sup>   | (-)±(-)              | 17.05±0.59           | (-)±(-)              | -0.44±0.23           |
| Thrust offset z [mm]               | 1.6 <sup>a</sup>   | (-)±(-)              | -0.03±0.18           | (-)±(-)              | 27.50±0.70           |
| Thrust angle $\alpha$ [deg]        | 0.02 <sup>b</sup>  | 0.00±0.01            | -0.02±0.10           | 1.99±0.01            | 15.61±0.40           |
| Thrust angle $\beta$ [deg]         | 0.02 <sup>b</sup>  | -1.31±0.04           | -9.68±0.35           | 0.00±0.01            | 0.25±0.13            |
| Thrust level [%]                   | 1 <sup>c</sup>     | 0.55±1.27            | 0.70±1.21            | -2.08±0.24           | 0.61±0.39            |
| Dipole x [Am <sup>2</sup> ]        | 0.13 <sup>d</sup>  | (-)±(-)              | -0.72±1.61           | (-)±(-)              | 2.24±15.02           |
| Dipole y [Am <sup>2</sup> ]        | 0.043 <sup>d</sup> | (-)±(-)              | -0.01±1.21           | (-)±(-)              | 0.01±0.04            |
| Dipole z [Am <sup>2</sup> ]        | 0.051 <sup>d</sup> | (-)±(-)              | -0.00±0.01           | (-)±(-)              | -0.02±2.33           |
| Control dipole x [%]               | 0.96 <sup>d</sup>  | (-)±(-)              | -0.32±1.07           | (-)±(-)              | 0.92±10.16           |
| Control dipole y [%]               | 1.93 <sup>d</sup>  | (-)±(-)              | -0.16±0.52           | (-)±(-)              | 0.00±0.02            |
| Control dipole z [%]               | 1.72 <sup>d</sup>  | (-)±(-)              | 0.00±0.02            | (-)±(-)              | -0.22±2.57           |
| Soft dipole x [Am <sup>2</sup> /T] | 1338 <sup>d</sup>  | (-)±(-)              | -0.02±0.24           | (-)±(-)              | -0.04±1.88           |
| Soft dipole y [Am <sup>2</sup> /T] | 1096 <sup>d</sup>  | (-)±(-)              | 0.02±0.20            | (-)±(-)              | 0.00±0.01            |
| Soft dipole z [Am <sup>2</sup> /T] | 683 <sup>d</sup>   | (-)±(-)              | 0.00±0.01            | (-)±(-)              | 0.02±0.96            |
| Accommodation [-]                  | 0.6                | 13.13±34.80          | 0.37±32.01           | -2.54±4.18           | 1.95±2.13            |
| Accommodation [-]                  | 0.8                | 7.85±20.86           | 0.28±19.06           | -1.42±2.35           | 1.05±1.19            |
| Accommodation [-]                  | 0.9                | 2.57±6.85            | 0.11±6.22            | -0.44±0.73           | 0.31±0.37            |
| Accommodation [-]                  | 1                  | -14.01±38.77         | -0.88±33.81          | 1.94±6.49            | -1.36±1.68           |
| Specular frac. [-]                 | 0.01               | -0.11±0.30           | 1.31±0.46            | 0.06±0.10            | 0.16±0.25            |
| Specular frac. [-]                 | 0.02               | -0.23±0.60           | 2.61±0.92            | 0.12±0.21            | 0.32±0.51            |
| Specular frac. [-]                 | 0.03               | -0.34±0.90           | 3.90±1.37            | 0.18±0.32            | 0.48±0.78            |
| Atmospheric temp. [K]              | 200                | -0.45±0.63           | -1.53±1.45           | 0.06±0.13            | 0.65±0.65            |
| Wall temp. [K]                     | 200                | 0.49±1.30            | -0.00±1.18           | -0.09±0.14           | 0.06±0.07            |
| Flow speed [m/s]                   | 200                | -3.10±2.76           | -2.80±2.60           | -0.07±0.27           | 0.24±0.60            |

<sup>a</sup> *Kolkmeier et al. (2008)*.

<sup>b</sup> Root mean square error of fit, this chapter.

<sup>c</sup> *Wallace et al. (2011)*.

<sup>d</sup> Root mean square error of fit, chapter 2.

pothesis that force modeling is less error-prone, and the force-derived wind is thus likely closer to the true wind. We discuss the four most prominent parameters in more detail below. Their effect on the wind data is plotted against magnetic latitude in Figure 3.10.

First and foremost, the thruster misalignment plays a central role. From Table 3.5 and Figure 3.10, we conclude that thrust angle  $\alpha$  causes almost purely an offset in vertical wind, and thrust angle  $\beta$  in horizontal wind. The large discrepancy in sensitivity of the two data sets makes this an ideal parameter to improve their consistency. Note that the mean and standard deviation in Table 3.5 are computed for an error of  $0.02^\circ$  (the maximum root mean square error of the fits in Figure 3.4), whereas a maximum error of  $0.9^\circ$  is reported by *Kolkmeier et al. (2008)*. For such values of thruster misalignment the wind offsets reach values in excess of 1000 m/s. An offset in the thrust application point has a similar effect on the torque-derived wind, but its maximum magnitude is much smaller.

Second, the longitudinal component of the spacecraft magnetic dipole has a significant influence on the torque-derived wind. The vertical wind is affected the most, because of the large influence of magnetic torques on the pitch axis (see chapter 2). The difference is the largest at the magnetic poles, due to the orientation of the magnetic field.

Third, the energy accommodation coefficient is changed. Note that we choose a small change of only 0.03 in Figure 3.10 to compare it to the specular fraction hereafter. The parameter has by far the strongest impact of all parameters on the force-derived horizontal wind, and a large impact on the torque-derived horizontal wind. Comparing the trend in the nominal wind and the difference, we may conclude that the accommodation coefficient primarily scales the horizontal wind. This specific pattern was also observed by *Dhadly et al. (2018)* (see Figure 2), who assumed it was a latitude-dependent offset. The vertical wind is less sensitive to the accommodation coefficient. Chapter 5 will focus on the effect of accommodation on the consistency of estimated parameters and the GOCE wind data.

Finally the specular fraction of the particle–surface interaction is investigated. The increase from 0 to 3% causes a change in horizontal wind seven times smaller than a similar adaptation of energy accommodation (from 0.93 to 0.9), judging from the standard deviations in Table 3.5. On top of that, it causes a slight offset in torque-derived horizontal wind, which is not observed in the force-derived wind. The overall trend of the difference is similar to that of the nominal wind. The difference in sensitivity between specular fraction and accommodation coefficient can at least in part be explained by the non-linear relation between these parameters and the aerodynamic model coefficients. At higher values of accommodation, the change in force and moment coefficients is more steep, eventually resulting in a steeper change in wind.

### 3.6. CONCLUSION

Comparing the cross-wind data sets presented in this chapter, taking into account the required effort to arrive at the current model fidelity, we conclude that although it is possible to obtain cross-wind from angular acceleration measurements, it is highly impractical. In the specific case of GOCE the most problematic model parameter is the thruster misalignment. The extreme sensitivity to these angles forces us to use the force-derived

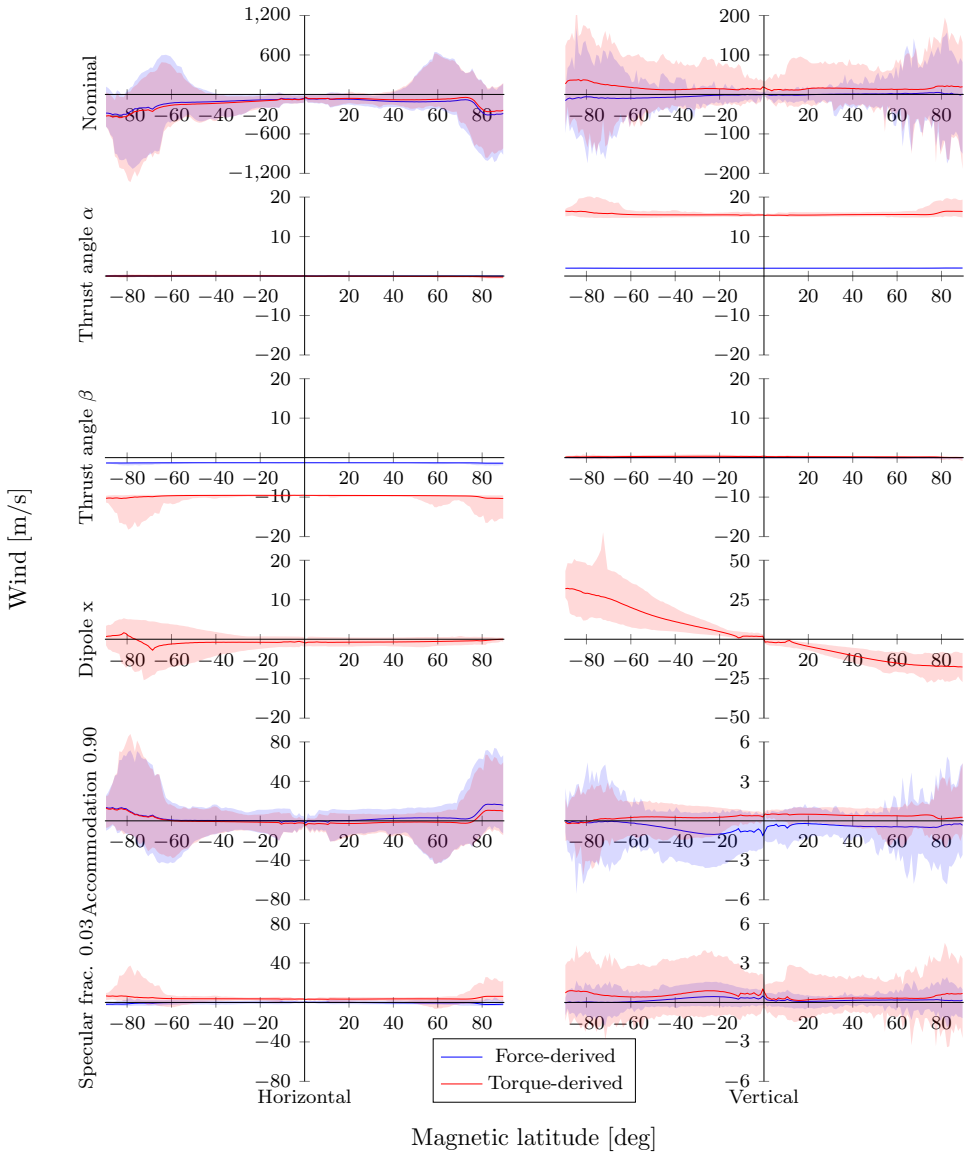


Figure 3.10: Horizontal (left) and vertical (right) wind difference from nominal due to a selection of model parameters from Table 3.5, in terms of min-mean-max over one degree magnetic latitude bins for March 2013. Note the different limits on the vertical axes.

wind measurements to tune the torque-derived ones. This fact implies that satellites that use continuous thrusting are not suitable for deriving wind purely from attitude motion. More generally for low-Earth-orbiting accelerometer missions currently in use, the knowledge of the magnetic properties of the satellite is likely insufficient to do without a dipole estimation procedure like the one of section 2.3.6. Although these estimates have greatly improved the result, the similarity of the difference between the two wind data sets to the vertical component of the Earth's magnetic field implies that some interaction between the magnetic field and the satellite remains unmodeled. This implies that we still lack knowledge of the magnetic and electronic properties of GOCE. Note that we have not been able to obtain magnetic properties as a function of large internal currents for GOCE in chapter 2. Later attempts to explain the difference by satellite charging, or static charges in the ion engine, have failed because the required charges were several orders of magnitude higher than anticipated. We conclude that if accurate data is to be obtained from the attitude motion of future satellites, a complete magnetic dipole budget is required, including current loops and electrically charged elements.

The difficulties described above mostly pertain to the lower frequencies. These are also the frequencies at which the estimation of magnetic dipoles, thruster misalignment angles, and acceleration bias have their primary effect. Horizontal wind errors are dominated by a once-per-orbit signal, and at frequencies above ten times orbital frequency the force- and torque-derived vertical cross-winds show a strong correlation. We may conclude that the force-derived wind is thus internally validated at frequencies above ten times orbital frequency by the torque-derived data. At the same time the mean vertical wind cannot be determined from the GOCE accelerometer data alone.

This form of internal validation of the force-derived wind is also the true value of simultaneous wind observations from linear and angular accelerations. The total set of estimated model parameters provides us with the opportunity to test the consistency of wind measurements without the need for other measurement sources. Instead of tuning aerodynamic model parameters (such as the energy accommodation coefficient) to match other models and observations, we may look for parameters that provide the most consistent estimates of magnetic, thruster, and calibration parameters, as well as consistency between force- and torque-derived wind. From the sensitivity analysis we have strong indications that lowering the accommodation coefficient from its current value of 0.93 will improve at least the latter.

A similar simultaneous estimation of the density using GOCE linear and angular acceleration data is impossible. Due to the satellite's geometric design the aerodynamic response in roll is insufficient to be used in the presented algorithm, reducing the number of independent measurements to five. Horizontal wind can be obtained from the lateral force or the yaw moment, vertical wind from the vertical force or the pitch moment, neutral density only from the longitudinal force. If a simultaneous density estimation is desired in a future mission, the paddlewheel concept could be applied to the GOCE design by rotating the fins accordingly.

Taking into account above-mentioned limitations, one particularly interesting application for the presented algorithm is the Swarm constellation. Due to limited reliability of the accelerometer data of these satellites, horizontal wind data may not be obtained from the linear accelerations (*Siemes et al., 2016*). However, assuming that the yaw rate

and acceleration can be obtained from the precise attitude data of the star cameras, the yaw torque may replace side force as a potential source for horizontal wind data. As the Swarm satellites are intended for high-accuracy measurements of the Earth's magnetic field, the magnetic properties of these satellites are well known and documented. On top of that, the Swarm satellites do not use continuous thrusting, removing the largest uncertainties from the torque modeling process. A detailed investigation into the house-keeping data and attitude motion of the Swarm satellites is required to test this hypothesis.

### ACKNOWLEDGEMENTS

The authors would like to thank ESA, and specifically Micheal Fehringer, Björn Fromknecht, and Rune Floberghagen, for their support in navigating the data (access may be requested at <https://earth.esa.int/web/guest/-/goce-data-access-7219>; the GOCE Mass Properties file is available at <https://earth.esa.int/web/guest/-/goce-mass-property-file-8276>) and documentation (available through personal communication) required for this study. We also thank Robbie Robertson for kindly providing his parametrized eclipse transition model.



# 4

## CHARACTERIZATION OF THERMOSPHERIC VERTICAL WIND ACTIVITY AT 225- TO 295-KM ALTITUDE USING GOCE DATA AND VALIDATION AGAINST EXPLORER MISSIONS

**T. VISSER, G. MARCH, E. DOORNBOS, C. DE VISSER, and  
P. VISSER**

*In chapter 3, the horizontal and vertical cross-wind at 225–295 km altitude were derived from linear acceleration measurements of the Gravity field and steady-state Ocean Circulation Explorer (GOCE) satellite. The vertical component of these wind data is compared to wind data derived from the mass spectrometers of the Atmosphere Explorer C (AE-C) and E (AE-E), and Dynamics Explorer 2 (DE-2) satellites. From a statistical analysis of the 120-second moving-window standard deviation of the vertical wind ( $\sigma(V_z)$ ), no consistent discrepancy is found between the accelerometer-derived and the mass spectrometer-derived data. The validated GOCE data is then used to investigate the influence of several parameters and indices on the vertical wind activity. To this end, the probability distribution of  $\sigma(V_z)$  is plotted after distributing the data over bins of the parameter under investigation. The vertical wind is found to respond strongly to geomagnetic activity at high*

This chapter has been published as a paper in JGR: Space Physics **124**, 6 (2019) ([Visser et al., 2019b](#)).

*latitudes, although the response settles around a maximum standard deviation of 50 m/s at an Auroral Electrojet index of 800. The dependence on magnetic local time changes with magnetic latitude, peaking around 4:30 over the polar cap and around 01:30 and 13:30 in the auroral oval. Seasonal effects only become visible at low- to mid-latitudes, revealing a peak wind in both local summer and winter. The vertical wind is not affected by the solar activity level.*

## 4.1. INTRODUCTION

The purpose of this chapter is to identify and characterize the drivers of vertical wind activity in the thermosphere at 225–295 km altitude, from a dusk–dawn orbit that covers all magnetic latitudes. We do so by introducing, validating, and analyzing a new vertical wind data set derived from linear acceleration data of the Gravity field and steady-state Ocean Circulation Explorer (GOCE) satellite (*Floberghagen et al., 2011*). The detailed discussion of the vertical wind response to a range of parameters, namely magnetic latitude (MLAT), geomagnetic activity, local time, season, and solar activity, may aid atmosphere modelers in their efforts to capture the behavior of the thermosphere.

Vertical wind in the thermosphere is characterized by peaks in the auroral oval and polar cap regions, sometimes exceeding 100 m/s (*Innis et al., 1999; Smith and Hernandez, 1995*, e.g.). They are concentrated in the midnight–dawn sector in terms of magnetic local time (*Innis and Conde, 2002*). On top of that, local vertical velocity enhancements have been observed of 10–50 m/s, not limited to the high-latitude regions (*Anderson et al., 2012; Larsen and Meriwether, 2012*). These enhancements may persist for several hours and have been linked to local time, being predominantly downward during the day and upward around midnight (*Sipler et al., 1995; Smith and Hernandez, 1995*).

Currently the primary source of vertical wind measurements in the F-region is ground-based Fabry–Perot Interferometry (FPI) (*Anderson et al., 2012*). These wind measurements are inferred from the Doppler shift in the night-time emission at specific wavelengths. Downsides of this method include the limited spatial distribution of measurement stations and the requirement of night-time clear-sky conditions. On top of that, FPI depends on a choice for a zero Doppler baseline (*Anderson et al., 2012; Aruliah and Rees, 1995; Larsen and Meriwether, 2012*). It has been suggested by *Harding et al. (2017)* that, combining all measurements errors, large wind measurements may be up to 100% uncertain. The major secondary source of vertical wind data is in situ mass spectrometry. These data were collected by the Atmosphere Explorer C (AE-C) and E (AE-E) (*Spencer et al., 1973b*), and Dynamics Explorer 2 (DE-2) satellites (*Hoffman, 1980*). Depending on the orbit, satellites can provide global coverage at arbitrary local times. The AE-C mission was designed to focus on auroral latitudes, leading to a better understanding of aurora-induced gravity waves (*Knutson et al., 1977; Spencer et al., 1976*). The AE-E satellite on the other hand had an equatorial orbit. Finally, DE-2 provided global coverage of vertical wind data for the first time, which led to the statistical analysis of *Innis and Conde (2002)* that we have adopted for this work as well.

The new vertical wind data presented in this paper were obtained from the GOCE linear accelerations, which were used to produce thermospheric horizontal wind and neutral density data (*Doornbos, 2016*) and to investigate thermospheric wave activity (*Garcia et al., 2013; Trinh et al., 2018*) in the past. The way of deriving these data is described in detail in chapter 3. In this chapter we closely follow the statistical analysis of *Innis and Conde (2002)* to compare the accelerometer-derived data from GOCE to the spectrometer-derived data from the three aforementioned missions. First we calculate the moving-window standard deviation of the vertical wind  $\sigma(V_z)$  for all data sets. The GOCE data are validated against the other satellite measurements by comparing the probability distributions of this parameter under specific, fixed conditions. Finally we take advantage of the size of the new data set to analyze how the vertical wind ac-

tivity changes with some key parameters and indices. In this process the data are first distributed over bins of a vertical wind driver (such as the Auroral Electrojet (AE) geomagnetic index (*Neil Davis and Sugiura, 1966*)), before calculating the probability distribution of the  $\sigma(V_z)$  parameter in each bin. The resulting plot is used to characterize the response of the vertical wind to the driving parameter.

Because of its high data rate (currently interpolated at 0.1 Hz) and continuous four year operation (resulting in 1100 full days of 16 orbits and another 170 days of partial operation), GOCE single-handedly provides 26 times as many thermospheric vertical wind data as the three aforementioned Explorer missions combined. Merely the size of the data set may therefore spark new investigations into this component of thermosphere research. In the results of our analysis we observe evidence of an upper limit to the vertical wind activity due to geomagnetic storms. The existence, value, and criteria for occurrence of this upper limit can contribute to the understanding of atmospheric damping, and the subsequent modeling of these effects in whole atmosphere models. The most prominent vertical wind features are short-lived, local wavelets with amplitudes up to 150 m/s near the auroral oval and over the polar cap. Especially these signals have the potential to support research into the occurrence and origins of gravity waves.

The chapter is structured as follows. The data used in this work are presented in section 4.2, and their distribution over several driving parameters is discussed. Then, in section 4.3, the data processing is described, as well as the definition of the main plots in this work. The GOCE vertical wind measurements are compared to those from the other satellites in section 4.4. The results are then discussed in section 4.5, in which the dependence of vertical wind activity on several parameters is shown. Finally, in section 4.6 the conclusions of this work are drawn.

## 4.2. DATA

All data used in this work are taken from satellite missions. The first three, AE-C, AE-E, and DE-2, were dedicated atmospheric research missions, whereas GOCE was initially intended for gravity field and ocean circulation studies only. In this section, we describe the data sets in terms of the required processing steps and their distribution over time, altitude, latitude, and solar and geomagnetic activity.

In Table 4.1, some key characteristics of the data sets are listed. Although the Atmosphere Explorers had a high apogee, around 4000 km, no data was gathered by these two missions above 600 km. Instead, the eccentricity of the orbit was meant to allow a deep dip into the atmosphere, which is especially clear for AE-C. The DE-2 orbit was polar, resulting in global coverage, both geographically and in local time. GOCE, on the other hand, was in a near-polar, sun-synchronous orbit, resulting in near-global geographic coverage and dusk-dawn coverage in local time. The offset of the magnetic poles from the Earth's rotation axis does however result in a sufficient variation in magnetic local time to allow a comparison with DE-2 in section 4.4.

AE-C, AE-E, and DE-2 used mass spectrometers to measure the vertical wind. The Neutral-Atmosphere Temperature Experiment (NATE, on the AE satellites) and the Wind And Temperature Spectrometer (WATS) infer the wind from density measurements. As the density is being measured, a baffle moves past the orifice through which the atmospheric particles enter the measurement chamber. This creates a dip in the density as

Table 4.1: Orbit and data set characteristics of the four satellites used in this study.

| Mission | Years of data | Altitude [km] | Inclination [deg] | Instrument        | Reference                         |
|---------|---------------|---------------|-------------------|-------------------|-----------------------------------|
| AE-C    | 1973–1977     | 134–4000      | 68                | NATE <sup>a</sup> | <i>Spencer et al. (1973b)</i>     |
| AE-E    | 1975–1977     | 248–4000      | 19.7              | NATE <sup>a</sup> | <i>Spencer et al. (1973b)</i>     |
| DE-2    | 1981–1983     | 210–1012      | 89.99             | WATS <sup>b</sup> | <i>Hoffman (1980)</i>             |
| GOCE    | 2009–2013     | 225–295       | 96.7              | EGG <sup>c</sup>  | <i>Floberghagen et al. (2011)</i> |

<sup>a</sup> Neutral Atmosphere Temperature instrument: scanning neutral mass spectrometer.

<sup>b</sup> Wind And Temperature Spectrometer: scanning mass spectrometer.

<sup>c</sup> Electrostatic Gravity Gradiometer: three orthogonal pairs of three-axis accelerometers.

the baffle blocks the incoming particles from directly entering the chamber. The incoming flow direction is inferred from the baffle position that blocks most of the particles. Combined with the attitude and orbital velocity information this flow direction results in a wind measurement (*Spencer et al., 1976, 1982*).

The algorithm to obtain vertical wind from the linear accelerations of a satellite has been extensively described in chapter 3. In short, the solar radiation pressure and thrust force are modeled and deducted from the measured acceleration. Assuming the remaining signal is aerodynamic, the direction of the incoming flow can be derived by matching an aerodynamic model with the residual acceleration. The incoming flow vector is reduced by the orbital velocity, such that the wind remains. The total (three-dimensional) wind measurements obtained from GOCE are rotated from the satellite body frame (in which they are derived) to the local orbit frame. In this chapter, we focus solely on the vertical wind component in this frame. The data set spans four years of global and continuous operation at altitudes between 225 and 295 km. It includes quiet and disturbed times (up to Kp 8-), a wide range of solar activity (F10.7 from 68 to 182), but only a limited local time (equator crossings at 06:22–7:52 (descending) and 18:22–19:52 (ascending)). On top of that, the GOCE orbit is tilted a few degrees towards the Sun in the North and away from the Sun in the South, which leads to longer eclipses on the Southern hemisphere.

To obtain a more comprehensive overview of the data availability, the data density is plotted over latitude and altitude in Figure 4.1, over Kp and F10.7 in Figure 4.2, and over magnetic local time and day of year in Figure 4.3. The intensity of the color indicates the data density compared to the most densely packed bin for that satellite; the solid line indicates the contour of the convex hull of the data set. In Figure 4.1, we can clearly identify the limitations in latitude and altitude imposed by the orbit geometries. The Atmosphere Explorers are particularly limited in their latitude range by their inclination, while DE-2 and GOCE show a concentration of data at high latitudes. The distributions over Kp index (which is, contrary to the AE-index, available for AE-E) and F10.7 flux in Figure 4.2 show a clear distinction between the quiet GOCE mission and the active DE-2 mission. The Atmosphere Explorers were, like GOCE, operated during a solar minimum. Finally, the precession of the orbits over a year can be inferred from Figure 4.3. Most importantly, the GOCE orbit remains mostly fixed in local time throughout the year, thus preventing any cross-contamination between local time and seasonal variations. Note that the bulk of GOCE measurements are taken at dawn and dusk; the full range of local times is only available during polar passes. The measurements of AE-C however, are

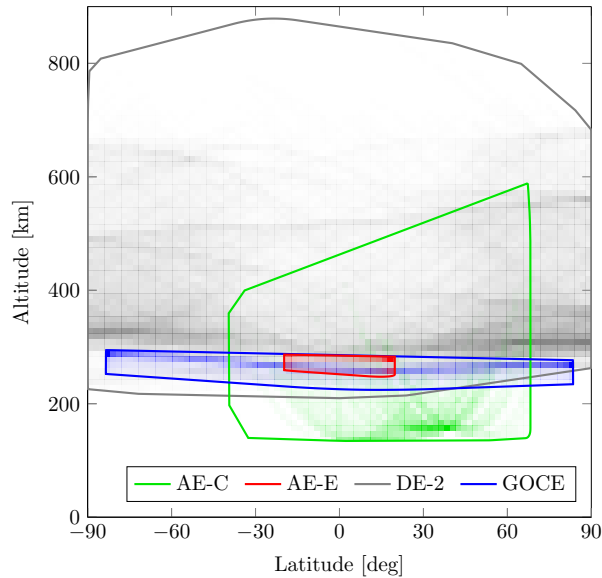


Figure 4.1: Distribution and convex hull of vertical wind data over latitude and altitude for all four satellites. The opacity indicates the data density as a percentage of the most densely packed bin per satellite.

concentrated along a few lines of local time and day of year. AE-E has only measured vertical wind during the Northern summer period.

The different data sets have different causes and levels of uncertainty. *Spencer et al. (1976)* analyzed the five main error sources for vertical wind measurements of the NATE instrument on AE-C. They found that the total error will not exceed 5 m/s. This error excludes the uncertainty in the spacecraft attitude measurement, which causes an estimated uncertainty of 20–30 m/s in the average vertical wind for DE-2 (*Spencer et al., 1982*). Assuming that the Atmosphere Explorers and DE-2 have similar characteristics, we conclude that the uncertainty in the mass spectrometer data is characterized by a maximum 30 m/s bias and maximum 5 m/s random error. The average wind level is also the largest uncertainty in the GOCE data. Judging from the sensitivity analysis of section 3.5, a bias of at least 3 m/s is possible. To arrive at the current GOCE vertical wind data, however, several parameters were estimated in that section such that the mean vertical wind was zero. Without such estimates, the (stable) bias in the mean wind exceeded 100 m/s. Even after parameter estimation, a systematic offset of 30–40 m/s exists between the Northern and Southern hemisphere. At the same time, the random error in the wind is expected to be much smaller, in the order of 3 m/s ( $3\sigma$ ). Additionally, the uncertainty in the energy accommodation coefficient may cause a scale factor error up to 20% (if the coefficient in the aerodynamic model would be lowered to 0.60, see section 3.5 for details).

The complete GOCE vertical wind data set is plotted in Figure 4.4 against time and argument of latitude (i.e. the angular progress through the orbit, starting from the Northward equator crossing). The main large-scale feature is the difference between the North-

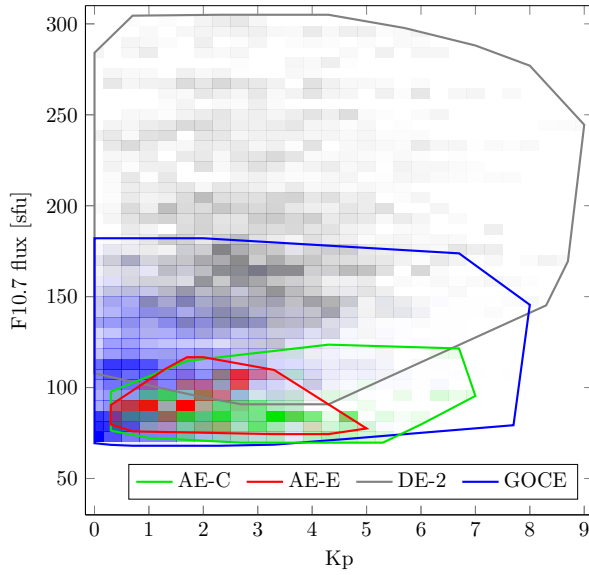


Figure 4.2: Distribution and convex hull of vertical wind data over Kp index and F10.7 daily observed flux for all four satellites. The opacity indicates the data density as a percentage of the most densely packed bin per satellite.

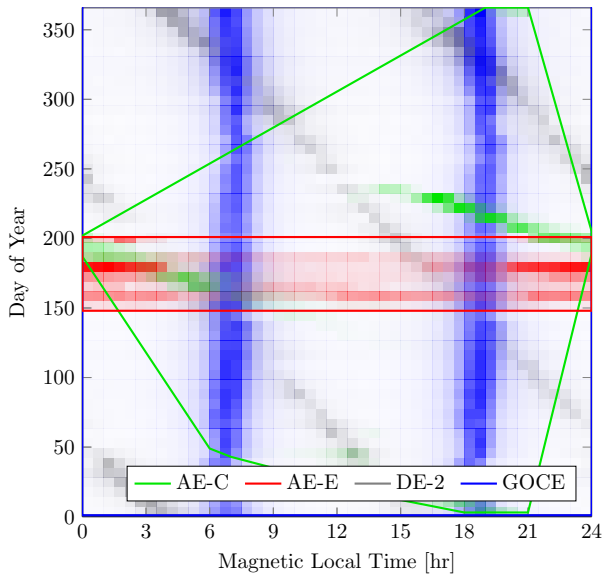


Figure 4.3: Distribution and convex hull of vertical wind data over magnetic local time and day of year for all four satellites. The opacity indicates the data density as a percentage of the most densely packed bin per satellite.

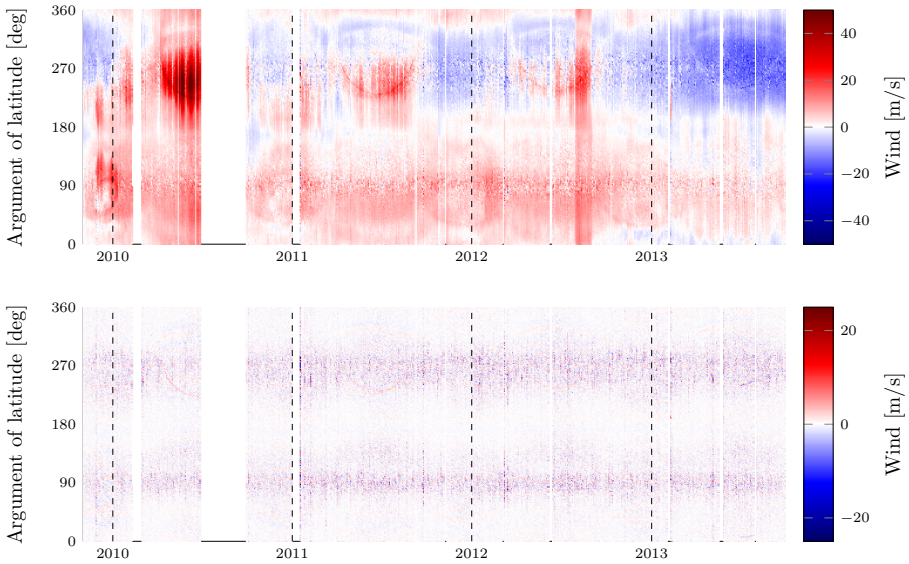


Figure 4.4: Vertical (upward) wind versus time and argument of latitude for the full GOCE mission (top panel), and the same data after high-pass filtering at 1/240 Hz (bottom). Note that the color scales are different in each panel.

ern (0–180° argument of latitude) and Southern hemisphere. Due to uncertainties in force and especially torque models, this low-frequency signal cannot be validated internally (see chapter 3), and further research is required to find its cause. Due to the uncertainties in the vertical acceleration bias, it is unclear whether the mean wind is up- or downward. A second large-scale feature are the arcs between 200° and 270° argument of latitude, observed between April and September of each year. These arcs overlap with eclipse transitions (cf. Figure 3.7), and are therefore attributed to an error in the transition model that was used to remove radiation pressure accelerations in the GOCE data processing. Similar arcs can be observed at different times and locations that do not align with eclipse transitions. The most important signal for the current discussion is the large amount of vertical wind peaks over the North (90°) and South pole (270°). This signal is more clearly visible in the bottom panel of Figure 4.4, for which the data were filtered using a second-order high-pass Butterworth filter with a cut-off frequency of 1/240 Hz. The magnitude of these peaks exceeds 150 m/s on roughly 240 separate occasions spread out over the four year mission.

### 4.3. METHODOLOGY

In order to compare our results directly with the related work of *Innis and Conde (2002)*, we calculate their  $\sigma(V_z)$  parameter for all satellite data sets. This is the standard deviation ( $\sigma$ ) of the vertical wind ( $V_z$ ) over a moving 120-second central window. This time interval corresponds to spatial scales of approximately 900–1000 km. The window is

moved by one data point at a time, to obtain a  $\sigma(V_z)$  value for each data point in the original set. Both the vertical wind and  $\sigma(V_z)$  are plotted for five representative passes in Figure 4.5. From visual inspection of the GOCE data we conclude that vertical wind peaks span 30–90 seconds, and most vertical wind activity takes the form of wavelets of several consecutive upward and downward peaks. This implies that high  $\sigma(V_z)$  values typically span one upward and one downward extremity. Signals that are significantly larger scale than the window (e.g. an offset due to the vertical acceleration bias uncertainty) will be filtered out automatically by the calculation of the standard deviation, so we do not high-pass filter the original data set first.

The standard deviation of the data in a window is a measure for the total power represented by that data. If the temporal resolution of the data is higher, higher frequencies are represented and the total power will increase. Within the current discussion, this will lead to an underestimation of  $\sigma(V_z)$  for the Explorer missions as compared to GOCE. Therefore we first note that while the GOCE accelerations are measured instantaneously (and the temporal resolution is therefore commensurate to the data rate), the baffle on the mass spectrometer takes about two seconds to perform a single sweep of  $\pm 24^\circ$  (Spencer *et al.*, 1973a). The worst case temporal resolution is therefore 18 s. At 8 km/s orbital speed however, a vertical wind of 150 m/s corresponds to an incidence angle of only  $1^\circ$ . Therefore we expect that the peak wind has generally been measured close to the middle of the sweep, and we assume the temporal resolution did not deviate much from the data rate. The underestimation of  $\sigma(V_z)$  can now be approximated for each pass in Figure 4.5 by integrating the periodogram between the Nyquist frequencies of the Explorer and GOCE data sets. Before integration, the periodograms are high-pass filtered using a second-order Butterworth filter with a cut-off frequency of 1/240 Hz, to simulate the effect of the moving 120-second window. The average  $\sigma(V_z)$  and its expected underestimation by the Explorers are indicated for each pass in the periodograms in Figure 4.5. The same procedure was repeated for all consecutive 15-minute time frames in March 2013. The results of this analysis are plotted against the mean magnetic latitude within the 15-minute frame in Figure 4.6, in terms of the 5<sup>th</sup> and 95<sup>th</sup> percentile and the median in each bin. From Figures 4.5 and 4.6 we conclude that underestimation of  $\sigma(V_z)$  by the Explorer missions is of the order of 1–2 m/s in the equatorial latitudes (where  $\sigma(V_z)$  is low), and increases with  $\sigma(V_z)$  towards higher latitudes. In particularly disturbed times, such as the pass on 1 March 2013 shown in Figure 4.5, the underestimation may surpass 20% of the value found for GOCE.

The second source of discrepancy between  $\sigma(V_z)$  data from GOCE and the Explorer missions is the difference in noise level. Since  $\sigma(V_z)$  reflects the total power in the measurements, it should ideally be corrected for the noise power (Chu *et al.*, 2018). The noise in the GOCE accelerometer data causes a vertical wind standard deviation below 1 m/s (see Table 4 of Visser *et al.* (2019a)), and is therefore ignored here. For the Explorer missions only the total error of the measurements is known, and the noise level can therefore not be corrected for.

Because of its definition as the standard deviation of the (centrally distributed) vertical wind,  $\sigma(V_z)$  is approximately Gamma-distributed. We find that the difference between data sets can be approximated by a single scale factor, defined as the ratio between the means. Assuming the vertical wind is zero mean, the scale factor of the standard de-

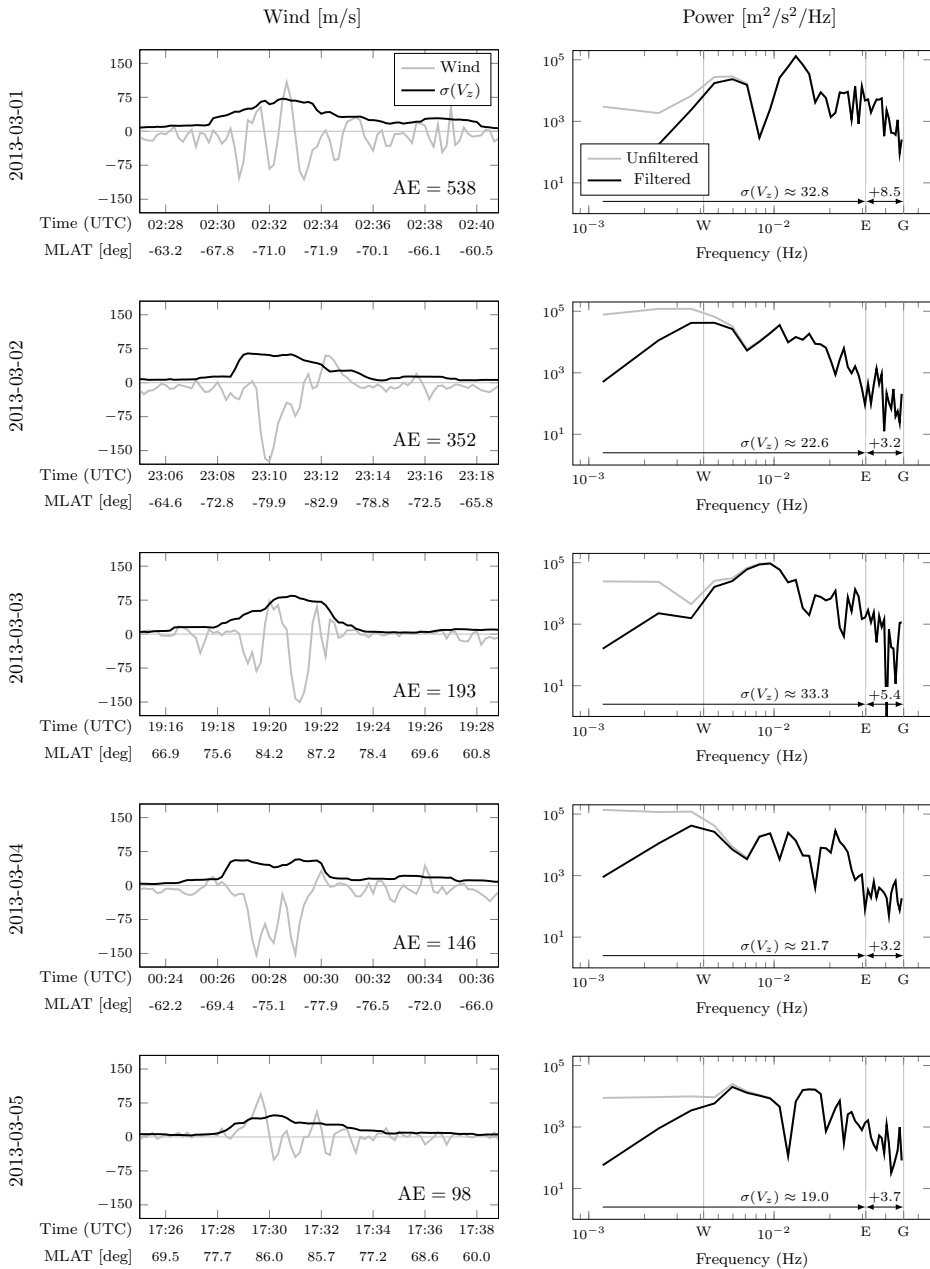


Figure 4.5: Time series (left) and periodograms (right) of vertical wind over the 14 minutes surrounding the largest peak of each of the first five days of March 2013. In the power spectra, the half-wave per  $\sigma(V_z)$  window ( $1/240$  Hz), and the Nyquist frequencies of the Explorer data ( $1/32$  Hz) and the GOCE data ( $1/20$  Hz) are indicated by the letters W, E, and G respectively. Based on the periodograms, an estimate is made of the average  $\sigma(V_z)$  value, and the underestimation of this parameter due to the difference in data rate between the missions.

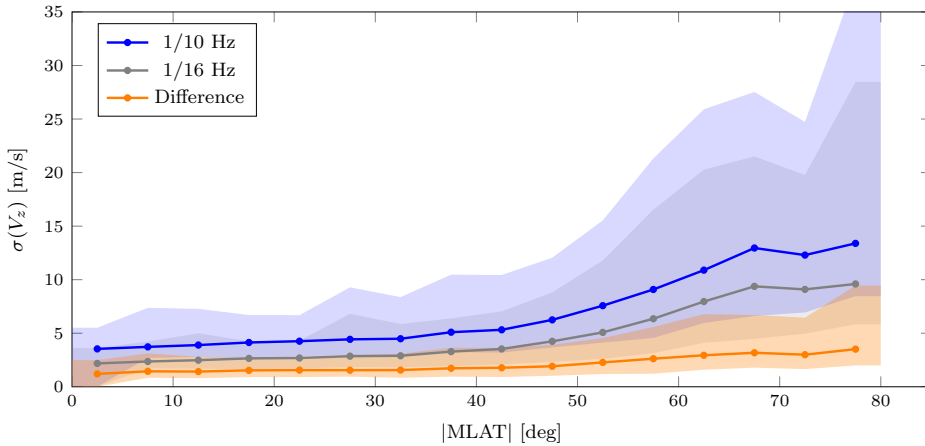


Figure 4.6: The average  $\sigma(V_z)$  parameter over 15 minute periods in March 2013, obtained for a data rate of 1/10 Hz, 1/16 Hz, and the difference between the two, in terms of the 5<sup>th</sup>, 50<sup>th</sup>, and 95<sup>th</sup> percentile in 5° magnetic latitude bins.

viation would directly apply to the vertical wind itself. This allows us to check whether the difference between accelerometer and spectrometer data can be explained by a single scale factor, such as is caused by a different choice of accommodation coefficient within the GOCE wind processing (see chapter 3).

The different data sets are compared in terms of their probability densities. These values are calculated by binning the data over 0.5 or 1 m/s bins, and subsequently dividing the amount of data in each bin by the total amount of data points and the bin width. To evaluate the uncertainty of the density in each bin, a Monte Carlo method is applied. In this method, the process of calculating the probability density is repeated for subsets of the data. These subsets are selected by dividing the  $\sigma(V_z)$  time series into consecutive 120-second sections. From each section the first data point is selected (out of 12 for GOCE and 7 for the Explorer missions) to find the first probability density, then the second data point is selected to find the second distribution, and so on. This process results in 12 probability densities for GOCE or 7 for the Explorer missions. The maximum and minimum density in each bin from this set of distributions are used as the uncertainty bounds. The same approach is used to find the uncertainty in the ratio between the means. In that case however the maximum uncertainty is found by dividing the maximum and minimum means of one data set by the minimum and maximum of the other data set respectively. The largest deviation from the original ratio is used as the uncertainty.

Before comparing the different missions, we identify the driving parameters. From the literature and the GOCE data we can identify four such parameters: magnetic latitude, magnetic local time, season, and geomagnetic activity. To quantify the last we use the hourly Auroral Electrojet (AE) index by default. As the AE index is not available for the years 1976–1977, we use the Kp index when we compare GOCE to the Atmosphere

Explorers. In line with *Innis and Conde (2002)*, we impose a maximum measurement altitude of 450 km.

In each comparison, we select a specific range of all the above parameters. First and foremost, the magnetic latitude range is split in the low-latitude (0–30°), mid-latitude (30–60°), auroral latitude (60–80°), and polar cap latitude range (80–90°). Magnetic local time is either set manually, or selected automatically based on the GOCE orbit. In this process the magnetic local time is split in 48 half-hour bins, in which the lowest Northern and Southern magnetic latitude are found for which GOCE data are available. After distributing all satellite data over the mesh of magnetic local time, only those data are kept that lie within these magnetic latitude bounds in each bin. We will refer to the remaining data as being a member of the GOCE orbit geometry. To account for seasonal variations, we divide the year in four periods: December solstice (November–January), March equinox (February–April), June solstice (May–July), or September equinox (August – October). When studying seasonal variations, the Northern and Southern hemisphere are treated separately. Finally we use the bounds on the AE index that were selected by *Innis and Conde (2002)*, being low ( $AE \leq 250$ ), medium ( $250 < AE \leq 500$ ), and high activity ( $AE > 500$ ).

After validating the GOCE vertical wind activity data, we investigate the impact of certain parameters on the vertical wind activity in terms of  $\sigma(V_z)$ . First we distribute the data over preset bins of a parameter of interest. Then in each bin, the 5<sup>th</sup>, 25<sup>th</sup>, 50<sup>th</sup>, 75<sup>th</sup>, and 95<sup>th</sup> percentile of  $\sigma(V_z)$  are calculated and plotted. The number of data points in each bin serves to quantify the confidence level of the percentiles in that bin. To allow for a high resolution in the driving parameter, no further constraints are placed on other driving parameters, unless stated otherwise.

#### 4.4. VALIDATION

The force-derived vertical wind data set described in this chapter is extensively compared to torque-derived data in chapter 3. The latter are dominated by the effects of model errors, but a high-pass filtered version is shown to be consistent with the force-derived wind within 50 m/s. In this section, we compare the  $\sigma(V_z)$  data derived from forces acting on GOCE to those obtained from the other satellite missions listed in Table 4.1.

In Figure 4.7, the GOCE data are compared to the DE-2 data by plotting the probability density distributions of the  $\sigma(V_z)$  data in the auroral and polar cap regions, over three levels of geomagnetic activity. For all plots only data are used that lie in the GOCE orbit geometry (as defined in section 4.3) and at altitudes below 450 km. Seasonal effects are ignored, as they are insignificant (less than 5 m/s  $\sigma(V_z)$ ) at these high latitudes, and both GOCE and DE-2 provide uniform coverage of the seasons (see Figure 4.3).

Especially at the polar cap the similarity between the two data sets over the full range of geomagnetic activity is striking. This is confirmed by the ratio of the means, included in the legend of each plot, which is consistent within 5%. In the auroral region the differences are larger, starting from 21% at low geomagnetic activity levels, decreasing to 6% at high activity. From the spectral analysis however, an underestimation of  $\sigma(V_z)$  by DE-2 was expected. This discrepancy may be explained by the higher random error in the DE-2 data, or by a too low accommodation coefficient in the aerodynamic model of the

GOCE satellite. The results in chapter 3 have however indicated that the latter parameter should rather be reduced than increased to improve the consistency of the GOCE wind data.

Performing the same analysis at low- and mid-latitudes, we can include data from AE-E and AE-C respectively (see Figure 4.8). At (magnetic) latitudes below  $60^\circ$ , seasonal effects play an important role, whereas the effect of geomagnetic storms dies out. Therefore we limit our comparison to the solstice months, in which all AE-E and most of the AE-C data were gathered. At the same time, a wide range of Kp values is included, selecting all Kp levels for which data from all plotted satellites are available. As before, the comparison is limited to the GOCE orbit geometry and altitudes below 450 km. Although all AE-E data lie below  $20^\circ$  latitude, the magnetic latitude regularly peaks at  $30^\circ$ , allowing us to use this limit in this comparison.

In the low-latitude region, the GOCE data align very well with the AE-E data, while the DE-2 distribution is drawn to higher vertical wind levels. We do note however that the peaks of the distributions lie at or below the maximum expected random error for all satellites, and may therefore be significantly impacted by the power of the measurement noise. This complicates the validation of the GOCE data in this latitude range. On top of that, the amount of data that is left from the mass spectrometer missions is limited. For AE-E only 1295 data points remain after data selection. This may explain the high ratio of means between this satellite and GOCE, despite the visual resemblance between the lines.

In the mid-latitude range GOCE lines up with DE-2, as was the case at higher latitudes. The consistency with the AE-C data is rather poor, with significantly higher vertical wind activity. As was the case for AE-E, only a small amount of AE-C data (1640 points) remains after the selection procedure. Consequently a small amount of anomalous passes may bias the overall result, as is reflected by the wide and erratic uncertainty bounds.

Despite the discrepancies between the different satellites at low- and mid-latitudes, which still require an explanation, we observe that GOCE always lines up well with one of the other satellites. This is an important result, as it suggests that there is no inherent bias between the different measurement techniques.

## 4.5. RESULTS

The main feature of interest in vertical wind data is the collection of large extrema in the auroral zone and over the polar caps (around  $90^\circ$  and  $270^\circ$  argument of latitude). This is best illustrated by the  $\sigma(V_z)$  parameter, plotted in Figure 4.9 for the full mission. The highest activity is concentrated at high latitudes. Especially during local summer, this area expands towards the descending node ( $180^\circ$ ), which corresponds to the dawn sector of the orbit.

The extra vertical wind activity in the midnight–dawn sector and its response to increased geomagnetic activity reported by *Innis and Conde (2002)* is confirmed for the South pole by the data obtained from GOCE. This is illustrated by the polar plots in Figure 4.10, which correspond directly to Figures 6–8 of *Innis and Conde (2002)*. Note that this specific local time sector is out of GOCE's view over the North pole.

The size of the new GOCE data set allows us to look at the effect of different parame-

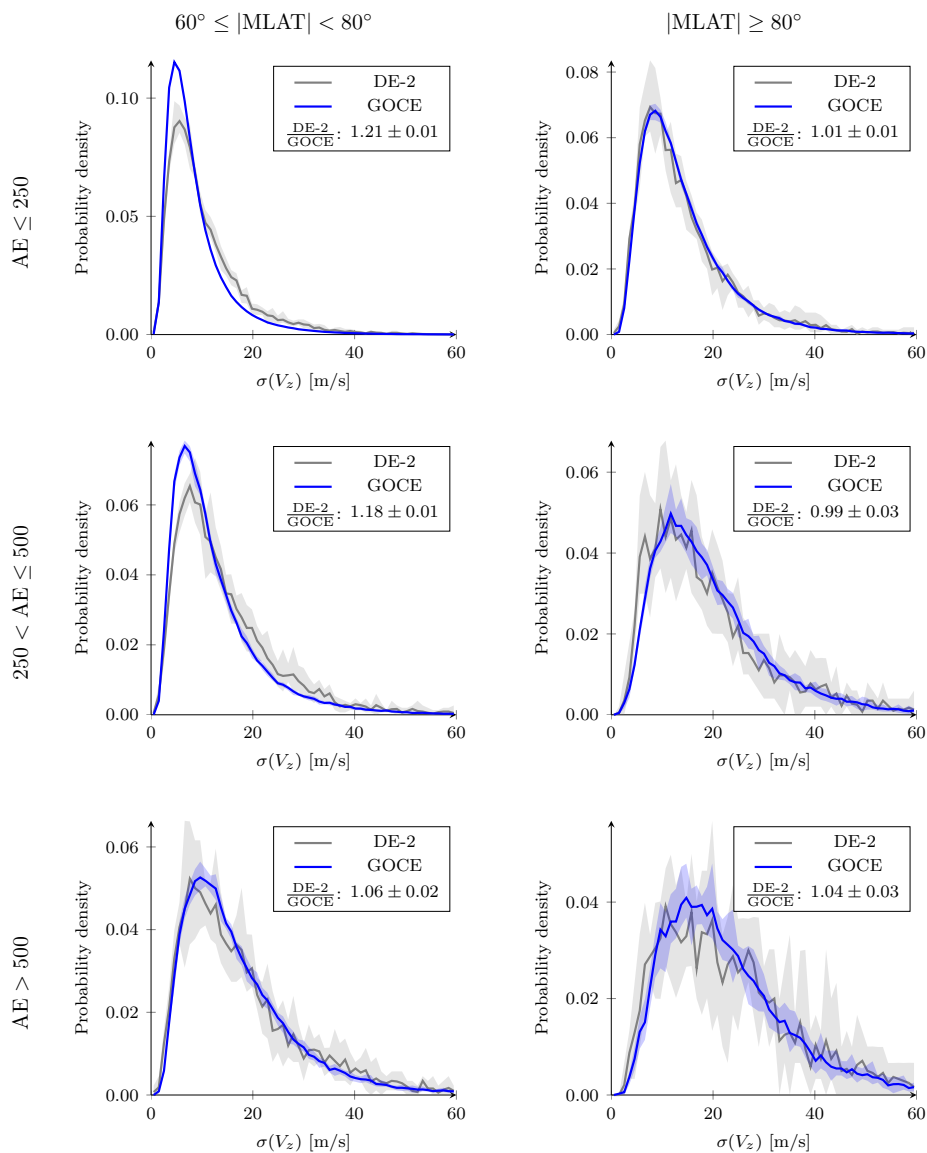


Figure 4.7: Probability density of the  $\sigma(V_z)$  data of GOCE, compared to that of DE-2, in the auroral (left) and polar cap latitudes (right), for different levels of geomagnetic activity.

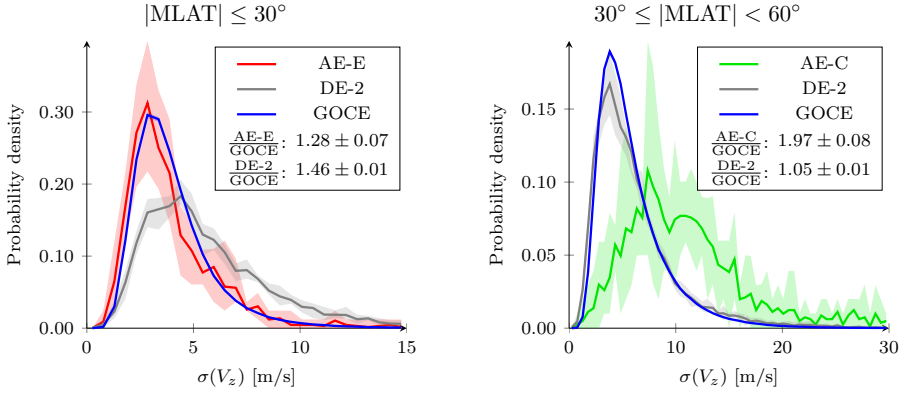


Figure 4.8: Probability density of the  $\sigma(V_z)$  data of GOCE, compared to that of DE-2 and the available Atmosphere Explorer, in the equatorial (left) and mid-latitudes (right), both using only the June and December solstice months, and adhering to the GOCE orbit geometry.

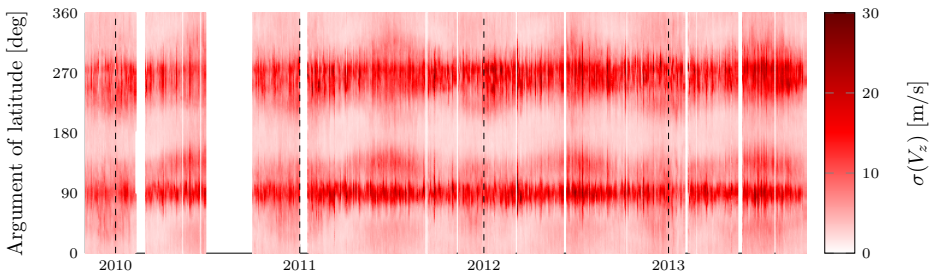


Figure 4.9: Moving window standard deviation of vertical wind  $\sigma(V_z)$  versus time and argument of latitude for the full GOCE mission.

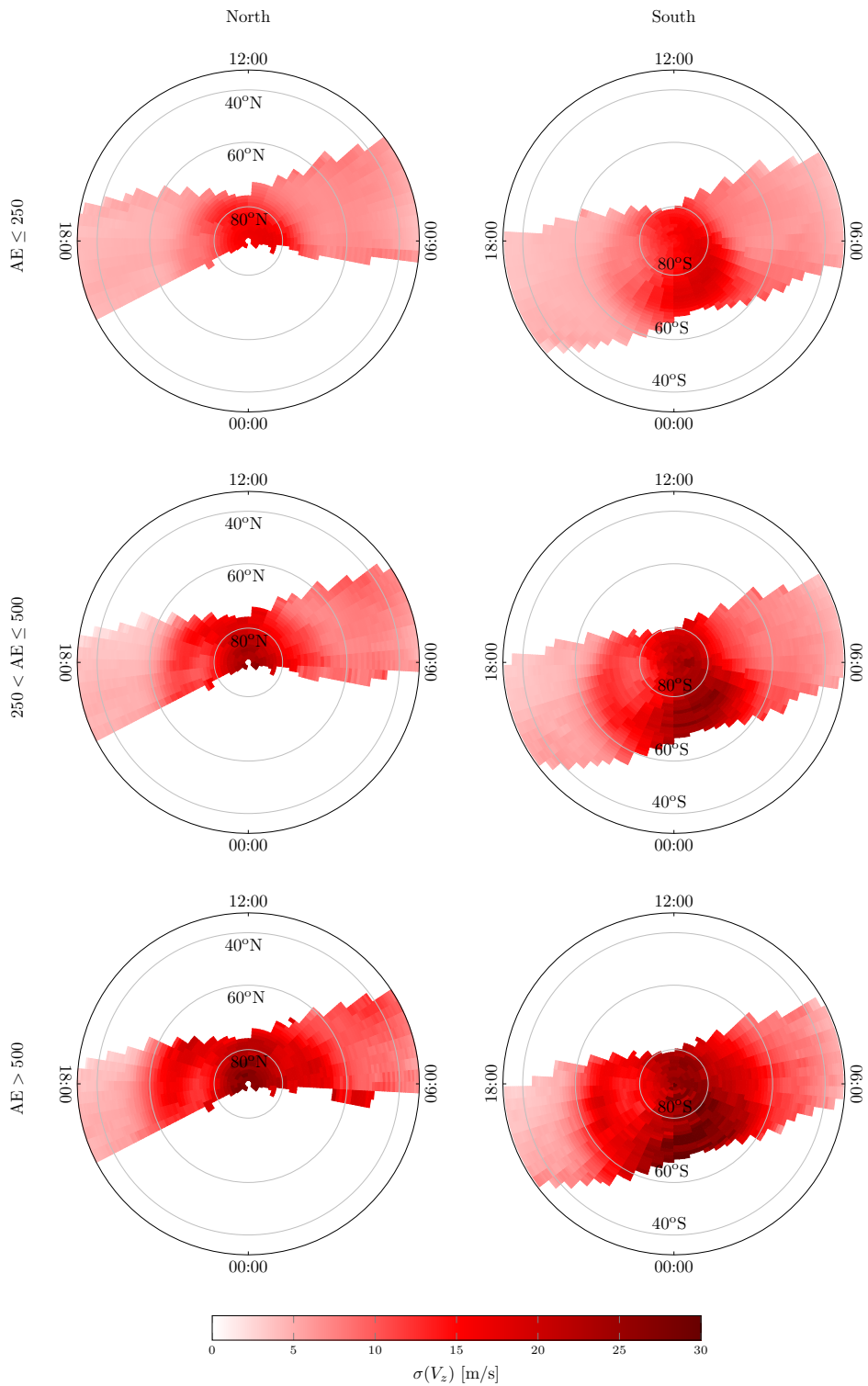


Figure 4.10: Standard deviation  $\sigma(V_z)$  versus magnetic latitude and magnetic local time over the North (left) and South pole (right) for different levels of geomagnetic activity in terms of AE.

ters on the vertical wind activity in the different latitude ranges in great detail. Because apart from the magnitude, no significant difference was found between the vertical wind in the low- and mid-latitude regimes, those regions are combined for the remainder of this discussion. The result of the statistical analysis is presented in plots like Figure 4.11. Here the light shaded area is bounded by the 5<sup>th</sup> and 95<sup>th</sup> percentile, the darker shaded area indicates the first and third quartiles, and the marked line connects the medians. The histogram to the left indicates the amount of data points in each bin. A large peak in  $\sigma(V_z)$  can maintain a level above 80 m/s for several minutes, resulting in 20–40 data points at 0.1 Hz. In our experience this means that bins containing less than 1,000 data points are particularly sensitive to outlier events.

The first parameter that we discuss in more detail is the AE index for geomagnetic activity. In Figure 4.11, the percentiles are plotted for the three magnetic latitude ranges. Over the polar cap the vertical wind response to geomagnetic activity seems to level out for AE values above 800, at  $\sigma(V_z)$  levels of 10–50 m/s (in terms of the 5<sup>th</sup> and 95<sup>th</sup> percentile). A similar trend can be observed in the auroral region at the highest percentile. The fact that the other percentiles follow a linear increasing trend may be explained by the limited latitude extent of the auroral oval within the selected latitude range. Only part of the latitude range is covered by the area of increased  $\sigma(V_z)$ , and this part increases with increasing geomagnetic activity. The increasing trend in  $\sigma(V_z)$  at high AE values in the low- and mid-latitudes is caused by the auroral oval moving down into the mid-latitude region.

The geomagnetic response observed as a function of the AE index does not depend on the choice of index. No important difference has been observed when using the (equatorial) Dst, Polar Cap (PC), or Kp index. The benefit of AE over Kp is that the former is linear and continuous, improving the resolution in the high activity domain of Figure 4.11.

The second parameter of interest is magnetic local time (MLT). Although its influence on the vertical wind was analyzed in the context of the polar plots in Figure 4.10, the percentiles in Figure 4.12 provide a higher resolution, as well as a view of the low- to mid-latitudes. Over the polar cap the distribution of vertical wind over local time is most uniform, with a peak around 04:30 and a dip around 21:00. In the auroral region, plotted separately for the two hemispheres in Figure 4.13, the distribution is much more pronounced. Clear peaks are observed at 01:15 (Southern hemisphere) and 13:15 (Northern hemisphere), and dips between 06:00 and 08:30, and at 17:45. Although especially the peaks can also be observed in Figure 4.10, the location of these extremities is predominantly driven by the non-uniform coverage of magnetic latitude at different local times. This is illustrated by the mean magnetic latitude in each bin, plotted on the right of Figure 4.13. A close correlation is observed between the location of the  $\sigma(V_z)$  extremities and the mean magnetic latitude in each bin. At the low- and mid-latitudes the peaks are lost due to the orbit geometry, but the dips remain visible at 06:45 and 19:00.

Third, we observe seasonal effects in the vertical wind, especially in the low- to mid-latitudes. This is illustrated in Figures 4.14 and 4.15 for the Northern and Southern hemisphere respectively. In the low- to mid-latitudes, the vertical wind activity dips in the equinox months, and peaks in both the June and December solstice months. The trend shows resemblance, if an inverted one, to the semiannual density variation. It is unlikely

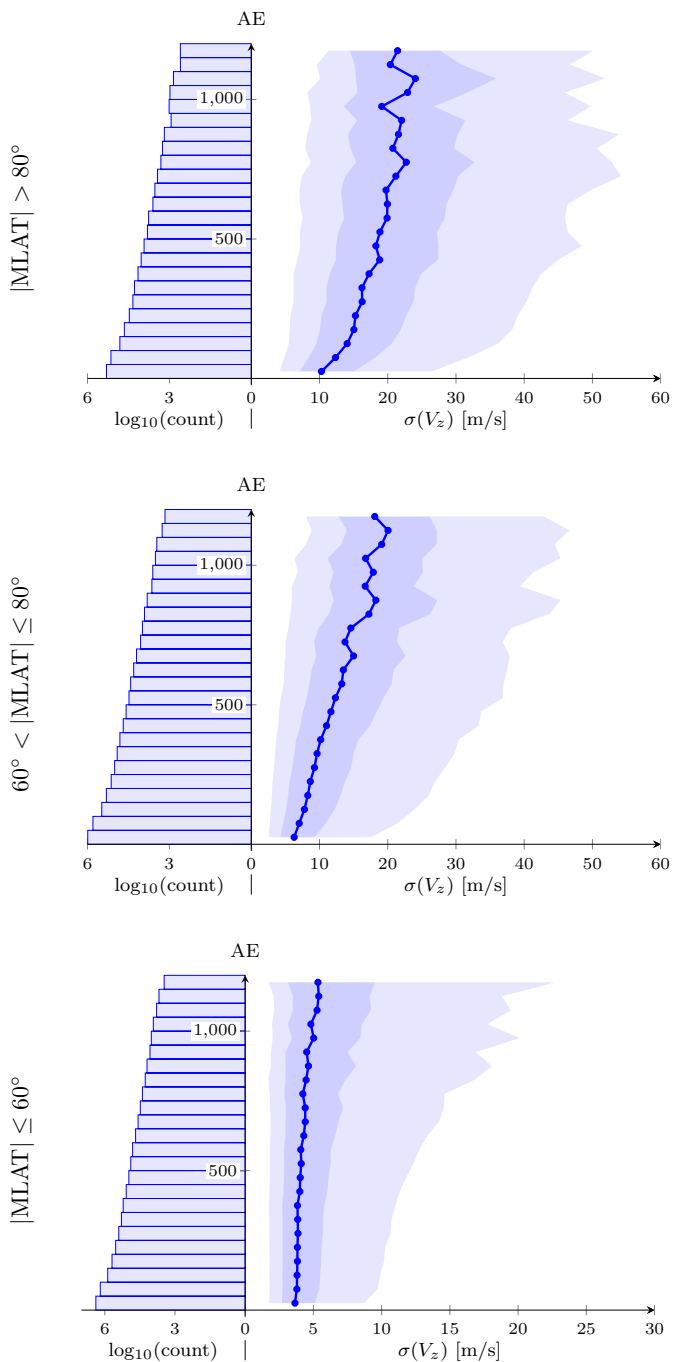


Figure 4.11: Percentiles (5<sup>th</sup>, 25<sup>th</sup>, 50<sup>th</sup>, 75<sup>th</sup>, and 95<sup>th</sup>) of  $\sigma(V_z)$  and data count, per bin of AE index, over the polar cap (top), auroral oval (middle), and low- and mid-latitudes (bottom).

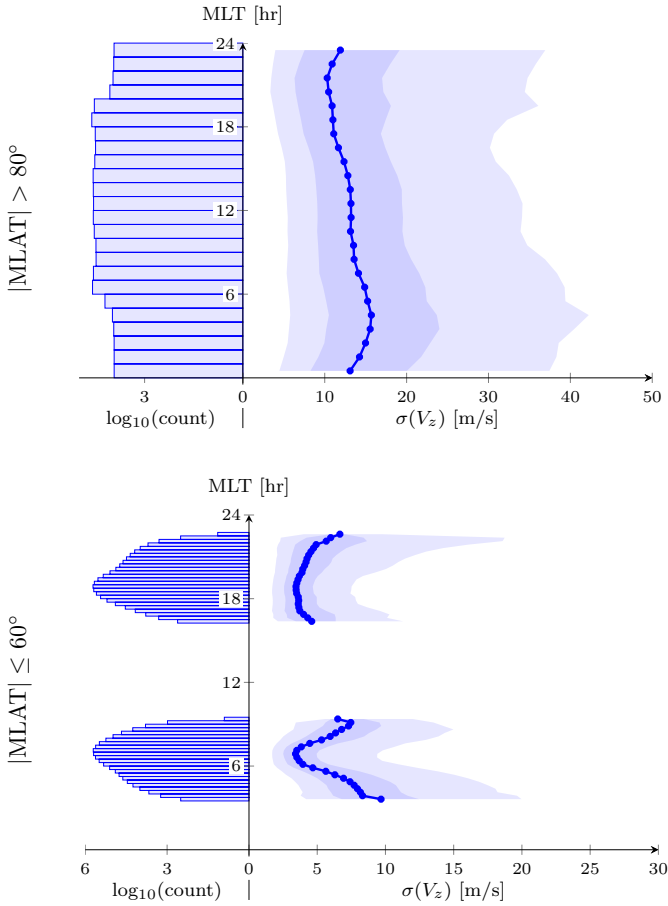


Figure 4.12: Percentiles (5<sup>th</sup>, 25<sup>th</sup>, 50<sup>th</sup>, 75<sup>th</sup>, and 95<sup>th</sup>) of  $\sigma(V_z)$  and data count, per bin of magnetic local time (MLT), over the polar cap (top, bin width one hour) and low- and mid-latitudes (bottom, bin width 15 minutes).

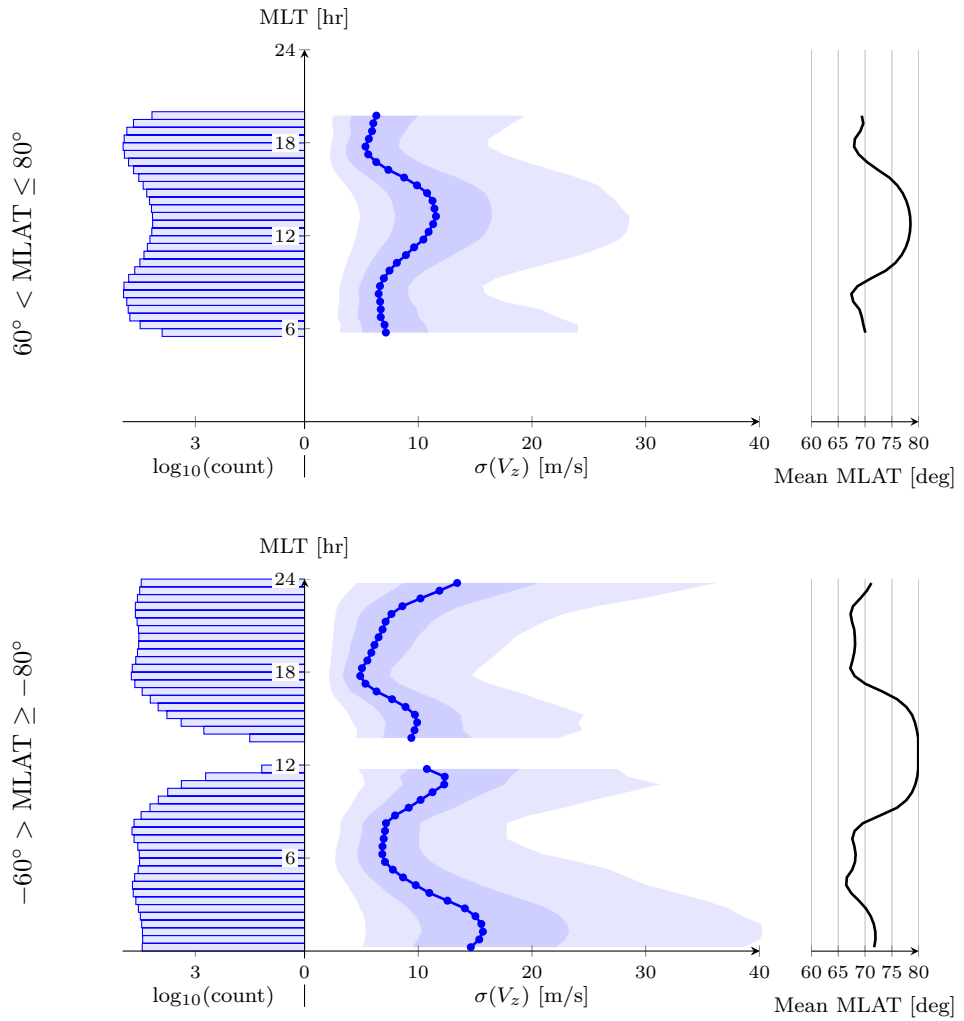


Figure 4.13: Percentiles (5<sup>th</sup>, 25<sup>th</sup>, 50<sup>th</sup>, 75<sup>th</sup>, and 95<sup>th</sup>) of  $\sigma(V_z)$  and data count, per bin of magnetic local time (MLT), over the Northern (top, bin width 30 minutes) and Southern auroral oval (bottom, bin width 30 minutes).

that the change in thermospheric composition will cause a large enough variation in the aerodynamic model to explain the entire difference between equinox and solstice (see Table 3.5 and Figure 3.9 of *Doornbos (2011)*). It is possible that the mechanism driving the semiannual density variation (e.g. the ‘thermospheric spoon’ suggested by *Fuller-Rowell (1998)*) also increases the vertical wind activity. A significant influence of the orbit geometry is unlikely, as the distribution over magnetic local time is mostly constant throughout the year (see Figure 4.3). At the polar cap, the seasonal trends are more erratic, but the peak winds seem to be concentrated around the local summer solstice. Although this observation would contradict the reduction in wind activity with increased solar illumination observed by *Innis and Conde (2002)*, it does confirm their conclusion that the effect is marginal. The trend in the auroral region seems to reflect a gradual transition from the low to the high latitudes.

Finally, we note that the vertical wind response to the observed F10.7 flux is similar for all latitude ranges, and weak overall. This is shown in Figure 4.16, where only the 95<sup>th</sup> percentile increases slightly, although not very consistently, with increasing solar flux. This increase may be explained by an overall increase in geomagnetic activity with increasing solar activity, rather than a direct solar radiation effect.

## 4.6. CONCLUSION

Despite the different sampling rate and uncertainty characteristics of the GOCE accelerometer data compared to the mass spectrometer data of AE-C, AE-E, and DE-2, we conclude that the vertical accelerations of the GOCE satellite are a valid source of vertical wind activity data. From the comparison, in terms of the moving window standard deviation  $\sigma(V_z)$ , with the data of the DE-2 satellite at mid and high latitudes, no structural error was found in the accelerometer-derived vertical wind. In the mid-latitude range, the AE-C winds disagree with the other two satellites. Given the scarcity of these data, outlier events may have had a significant influence on this discrepancy. In the low-latitude regime, the  $\sigma(V_z)$  probability distributions peak close to the expected maximum random error level of the respective data sets. Nevertheless a close match is found between the GOCE and AE-E data.

The result of this process is a vertical wind data set, validated for short time scales of at least 120 seconds, that single-handedly increases the amount of available measurements from satellites with a factor of 27. In total 1100 full days of data containing 16 orbits each and an additional 170 partial days are available, spread out over four years. Due to the orbit geometry, near global coverage is provided at an altitude between 230 and 290 km, limited in local time to dawn and dusk conditions. Data are available for low to medium solar activity and a wide range of geomagnetic activity levels.

The size of the data set allowed for a high-resolution investigation into the driving parameters of the vertical wind activity. Most importantly, a maximum vertical wind activity is observed in the response of the thermosphere to increased geomagnetic activity. In terms of the  $\sigma(V_z)$  parameter, the 95<sup>th</sup> percentile is expected to level out around 50 m/s activity levels, for AE index values above 800. In other geomagnetic indices the same behavior was observed.

Over the polar cap a single peak in activity is observed in the midnight–dawn sector, but the overall response is mostly uniform over the magnetic local time range. In the au-

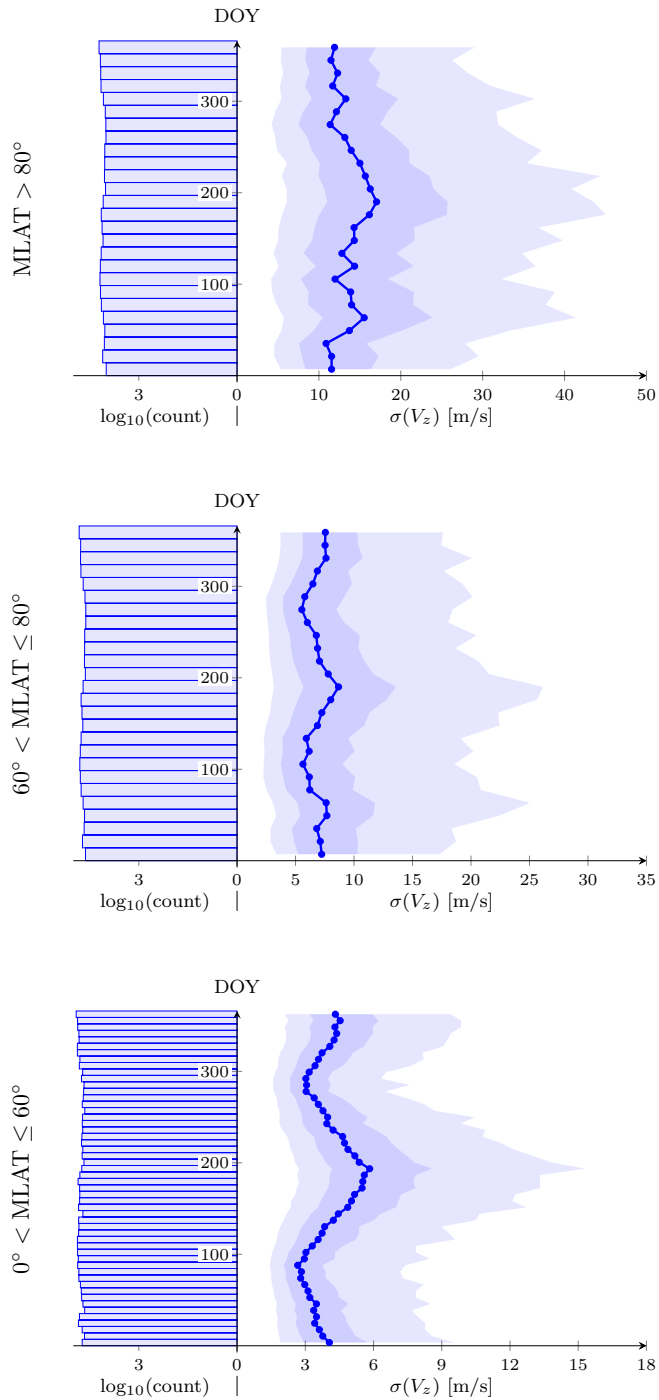


Figure 4.14: Percentiles (5<sup>th</sup>, 25<sup>th</sup>, 50<sup>th</sup>, 75<sup>th</sup>, and 95<sup>th</sup>) of  $\sigma(V_z)$  and data count, per bin of day of year (DOY), over the Northern polar cap (top, bin width two weeks), auroral oval (middle, bin width two weeks), and low- and mid-latitudes (bottom, bin width one week).

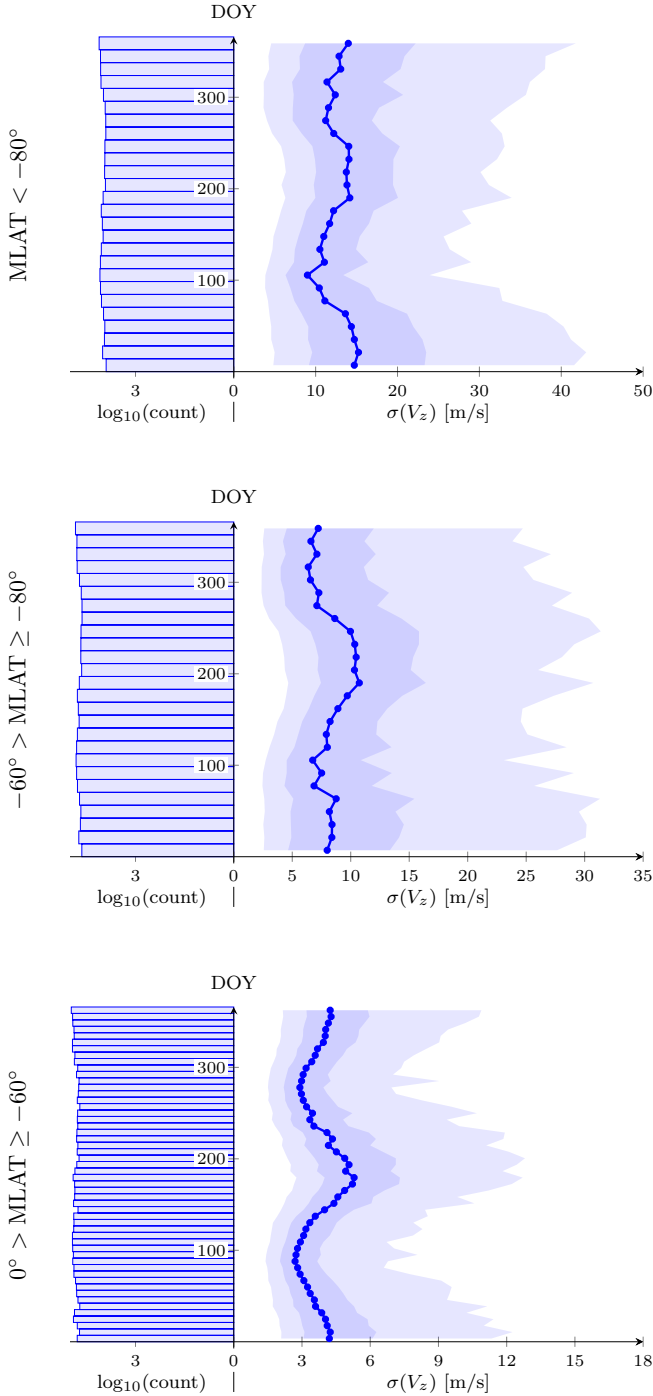


Figure 4.15: Percentiles (5<sup>th</sup>, 25<sup>th</sup>, 50<sup>th</sup>, 75<sup>th</sup>, and 95<sup>th</sup>) of  $\sigma(V_z)$  and data count, per bin of day of year (DOY), over the Southern polar cap (top, bin width two weeks), auroral oval (middle, bin width two weeks), and low- and mid-latitudes (bottom, bin width one week).

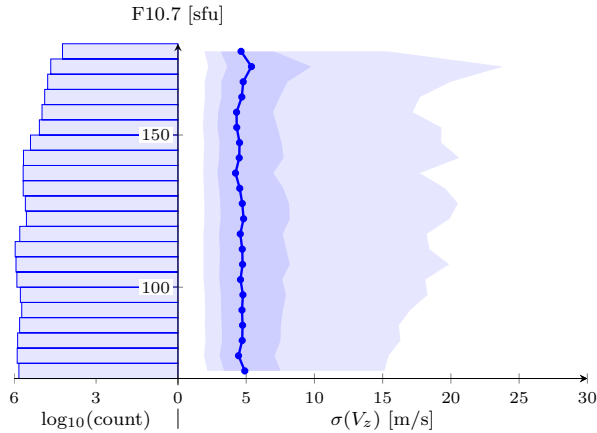


Figure 4.16: Percentiles (5<sup>th</sup>, 25<sup>th</sup>, 50<sup>th</sup>, 75<sup>th</sup>, and 95<sup>th</sup>) of  $\sigma(V_z)$  and data count, per bin of F10.7 flux, over the full latitude range.

roral latitude range the structure in local time is much more pronounced, but predominantly driven by the non-uniform coverage of magnetic latitude at different local times. At equatorial latitudes, dips were observed around 06:00 and 18:00 magnetic local time.

Seasonal variations are much smaller than the above effects, but are the dominant driver in the lower latitudes at fixed local times. Both on the Northern and Southern hemisphere the peak activity occurs around June solstice, with the December solstice producing a smaller peak. This seasonal variation resembles the semiannual density variation, which is thought to be caused by increased interhemispheric circulation at the solstices. At the polar cap, indications were found for a single peak just after local summer solstice, but more research is required to confirm this observation. Solar activity, in terms of the observed solar flux, does not influence the vertical wind activity.

Although the results of this chapter are promising, we do not expect a new accelerometer-derived vertical wind data set to be produced soon. The GOCE mission was unique in both its low altitude and its exceptionally sensitive accelerometers, but also the availability of high quality housekeeping data, like the thrust level. This combination led to an especially high aerodynamic signal, and the ability to actually detect and interpret it. It is however worth investigating whether similar observations can be made using other existing accelerometer-carrying satellites, such as GRACE and CHAMP, or future mission concepts, such as the proposed ESA Earth Explorer 10 candidate mission Daedalus (Sarris *et al.*, 2019).

## DATA STATEMENT

The GOCE thermospheric data used in this study are publicly available at <http://eo-virtual-archive1.esa.int/GOCE-Thermosphere.html> after requesting access through <https://earth.esa.int/web/guest/-/goce-data-access-7219>. The Atmosphere Explorer and Dynamics Explorer data are publicly available through NASA's

OmniWeb service, on <https://omniweb.gsfc.nasa.gov/ftpbrowser/index.html>. The AE index library is maintained by Kyoto University and publicly available at <http://wdc.kugi.kyoto-u.ac.jp/dstae/index.html>. The observed F10.7 flux is available on the NOAA ftp server at [ftp://ftp.ngdc.noaa.gov/STP/space-weather/solar-data/solar-features/solar-radio/noontime-flux/penticton/penticton\\_observed/tables/](ftp://ftp.ngdc.noaa.gov/STP/space-weather/solar-data/solar-features/solar-radio/noontime-flux/penticton/penticton_observed/tables/).



# 5

## THE GOCE PERSPECTIVE ON THE ENERGY ACCOMMODATION COEFFICIENT

*In the aerodynamic modeling of satellites, the energy accommodation coefficient ( $\alpha_E$ ) plays a central role. To find an experimental value for this parameter, the consistency can be investigated of thermospheric density and wind simultaneously observed from the linear and angular motion of a satellite. The applicability of this approach to the GOCE satellite is investigated in this chapter in three ways. First of all, the magnetic dipoles, thruster misalignment angles, and vertical acceleration bias — estimated in previous chapters — are estimated for a range of accommodation coefficient values. No significant improvement is however observed in these estimates. Second of all, the sensitivity of the difference between force- and torque-derived wind to  $\alpha_E$  is evaluated using the aerodynamic model. In the horizontal wind component, a bias of up to 10 m/s is expected between the two data sets; in the vertical component a scale factor up to 10%. Finally, the wind is derived from forces and from torques for a range of accommodation coefficients, and the two data sets are compared. The bias in the horizontal wind component is found to be reduced by the thruster misalignment estimates to a level below the uncertainty caused by those estimates. The vertical wind scale factor suggests the optimal accommodation coefficient lies in the range between 0.80 and 0.93, but this result strongly depends on the torque model set-up. We conclude that more accurate torque models are required to find an optimal accommodation coefficient based on simultaneous observation of linear and angular motion of GOCE.*

### 5.1. INTRODUCTION

The purpose of this chapter is to investigate the possibility of estimating the energy accommodation coefficient, purely by minimizing the difference between GOCE force- and torque-derived wind. We do so by analyzing the parameter estimates (magnetic

dipoles, acceleration bias and thruster misalignment angles) for a range of accommodation coefficients, and by deriving and comparing the required and achieved level of consistency between the force- and torque-derived thermospheric wind data, in both its horizontal and vertical component.

The interaction between neutral atmospheric particles and a satellite is typically modeled using (1) Maxwell theory (*Bird, 1994*), (2) the Cercignani–Lampis–Lord (CLL) model (*Cercignani and Lampis, 1971*), or (3) Diffuse Reflection with Incomplete Accommodation (DRIA) (*Moe and Moe, 2005*). The three models differ in the way particles are assumed to be re-emitted by the satellite wall. In the Maxwell model, a certain fraction of the particles is assumed to reflect of the surface in a specular fashion, while the rest is re-emitted with a fully diffusive (i.e. Lambert cosine) angular distribution. In the CLL model, all particles are re-emitted quasi-specularly, with a diffusive emission pattern centered around the direction of specular reflection. Finally, in the DRIA model, all re-emission is fully diffusive, but assumed to occur before the particles have fully accommodated to the temperature of the satellite wall. From flight tests on the Space Shuttle, *Gregory and Peters (1987)* found that at an altitude of 225 km, reflection of particles is 97–98% diffusive. Based on a range of measurements, *Moe et al. (1993)* concluded that at least around 200 km altitude the reflection of particles could be assumed to be fully diffusive. As GOCE flew below 270 km altitude, the DRIA model has been applied throughout this thesis.

An added benefit of the DRIA model is that it leaves only one parameter to assume or estimate: the energy accommodation coefficient  $\alpha_E$ . This coefficient describes the extent up to which the atmospheric particles are cooled down to the satellite wall temperature before re-emission (see e.g. Equation (2) of *March et al. (2019a)*). The accommodation coefficient depends strongly on the concentration of different atmospheric constituents. More specifically, adsorption of atomic oxygen on the satellite wall causes the accommodation to approach unity (*Moe et al., 1995*). In line with *Sutton (2009)*, we selected 0.93 as the default for our investigations.

Many practical investigations into the energy accommodation coefficient have focussed on obtaining consistent neutral density measurements, e.g. by comparing observed and modeled drag coefficients of spherical satellites (*Bowman and Moe, 2005*), or by combining linear and angular motion of paddlewheel satellites (*Pilinski et al., 2011*). Comparison of the horizontal wind obtained from GOCE to ground observations by *Dhadly et al. (2017, 2018)* however, revealed that a latitude-dependent bias exists in the GOCE cross-wind data. As was suggested in chapter 3, this bias may for a large part be explained by the accommodation coefficient being set too high. At the same time, in chapter 4 it was shown that the vertical wind component, derived using the same accommodation coefficient value, corresponds very well to earlier satellite observations. A comprehensive analysis of the effect of the accommodation coefficient on both force- and torque-derived wind is therefore required.

As described before in chapter 3, the cross-wind is derived by matching the directions of the residual force or torque and an aerodynamic model. A change in the wind data may thus be caused either by a change in the residual, or by a change in the aerodynamic model. Therefore, the effects of accommodation on the estimated non-aerodynamic parameters are analyzed first, by comparing the parameters obtained for three values

for  $\alpha_E$  (0.60, 0.80, and 0.98) to those obtained for the default value of 0.93. The three values of  $\alpha_E$  were chosen to be very low (0.60), close to the optimal value from the self-consistency of GOCE force-derived wind (0.80 at the time of writing, according to *March et al. (2019b)*), and the mean of the values suggested by *Pilinski et al. (2010)* from a range of measurements (0.98). Second, the effect of  $\alpha_E$  on the consistency of the aerodynamic model is investigated through a sensitivity analysis of the difference between force- and torque-derived wind. Finally, the force- and torque-derived wind are compared directly for all four accommodation coefficients. For each day of the mission, the bias and linear scale factor between the two wind data sets are determined, both in the horizontal and the vertical direction. To reduce the impact of remaining non-aerodynamic signals in the residual torque, this process is repeated after a constant electric dipole is estimated (as suggested in chapter 3).

Comparing the required and achieved consistency between GOCE force- and torque-derived horizontal wind, we conclude that simultaneous observation of linear and angular accelerations will likely not provide an estimate for the accommodation coefficient. But more importantly, several recommendations are provided for selecting suitable past missions and designing future ones to tackle this problem. The results of this chapter may therefore support future attempts to obtain aerodynamic parameters from simultaneous observation of linear and angular satellite dynamics.

In the subsequent sections of this chapter, the three aforementioned analyses and their results are presented. First, in section 5.2, the difference between the estimated parameters is shown for the aforementioned set of four accommodation coefficients. Then, in section 5.3, the aerodynamic coefficients are used to show the sensitivity of the difference between force- and torque-derived wind to the accommodation value. Finally, in section 5.4, the actual force- and torque-derived winds are compared, again assuming the set of four accommodation coefficient values. Each of these sections contains two subsections: one describing the methodology, and one presenting the results. In section 5.5, the results of this chapter are summarized and conclusions are drawn.

## 5.2. ESTIMATED PARAMETERS

In chapter 3, it was suggested that the search for the optimal accommodation coefficient may start at a comparison of parameters that are estimated throughout the process of deriving thermospheric data. More specifically, these parameters are the magnetic dipoles of the payload (as defined in chapter 2), the thruster misalignment angles, and the vertical acceleration bias (both defined in chapter 3). For this section all the parameters were estimated for three more values of the accommodation coefficient, namely 0.60, 0.80, and 0.98. The daily parameter values thus obtained, are compared to the default values found for  $\alpha_E = 0.93$ .

### 5.2.1. METHODOLOGY

The method of deriving the payload magnetic dipoles, magnetic torquer scale factors, and the residual torque offset is described in detail in subsection 2.3.6. In short, it amounts to a weighted least squares estimation minimizing the residual measured torqued that remains after reducing the total measured torque by the modeled aerodynamic, solar

radiation pressure, gravity gradient, magnetic control, and other magnetic torques (see Equation (2.1), and (2.11) to (2.12)). The magnetic dipoles and scale factors are first estimated using a simplified aerodynamic model, in which the density is obtained from NRLMSISE-00 and thermospheric wind is excluded. The torque caused by the initial daily estimates thus obtained, is included in the algorithm described in section 3.3 to obtain the vertical acceleration bias and thruster misalignment angles. These estimates are approximated by linear fits, and the measured force and the thruster force and torque are updated accordingly. Then the magnetic parameters are estimated again using these new models, and the resulting daily estimates are approximated by linear fits. In this section, the final sets of parameters are investigated. Note that a different value for accommodation affect these parameters through the initial aerodynamic model.

The daily estimates of the magnetic parameters and the acceleration bias are compared to the default values directly. This is done by plotting the default estimates on the horizontal axis, and the new estimates on the vertical axis (see e.g. Figure 5.1). To improve the readability of the plots, the data is first binned such that each bin contains 10% of the estimates. Then the 5<sup>th</sup> and 95<sup>th</sup> percentile are found in each bin, and connected to form the shaded polygons. All data that lie outside the polygon are plotted separately. Because the data is expected to be concentrated around the main diagonal of the domain (i.e.  $x = y$ ), the edges of the bins are defined perpendicular to this line. A comparison of the linear fits (as plotted in Figure 2.4 and 3.5) and the default daily estimates is added for reference. The thruster misalignment angles are plotted in a similar way, but in this case the difference from the default estimates is plotted on the vertical axis against the mean thrust level on the horizontal axis. The bins are then also defined along the horizontal axis.

5

### 5.2.2. RESULTS

First of all, the estimated dipoles and torquer scale factors are compared. In Figure 5.1, the hard and soft magnetic dipole estimates for different accommodation coefficients are plotted against the default estimates; the same is done in Figure 5.2 for the magnetic torquer scale factors and the torque offset.

For most dipole and scale factor estimates, the effect of a change in accommodation coefficient is small. Note that the comparison of the linear fit and daily estimates for  $\alpha_E = 0.93$  often tends to form an S-curve, or even a horizontal line. This suggests that the estimates oscillate around the linear fit (as is observed in Figure 2.4), and therefore the fit only explains part of the high and low values. In general, the error of the linear fit is significantly larger than the change in the estimates due to the change in accommodation coefficients. In other words, the remaining signal in the daily estimates cannot be explained by a different value of the accommodation coefficient.

The only significant exception is found in the estimates of the torque offset (in the bottom row of Figure 5.2). This offset is however merely included in the estimation process to improve the dipole estimates and therefore not included in the torque models, as explained in chapter 2. The differences in this parameter may be reflected in the thermospheric data, which are the subject of section 5.4.

Second of all, the vertical acceleration bias is plotted in the same way in Figure 5.3. In this case, the spread of the estimates for  $\alpha_E = 0.60$  is of similar magnitude as the residuals

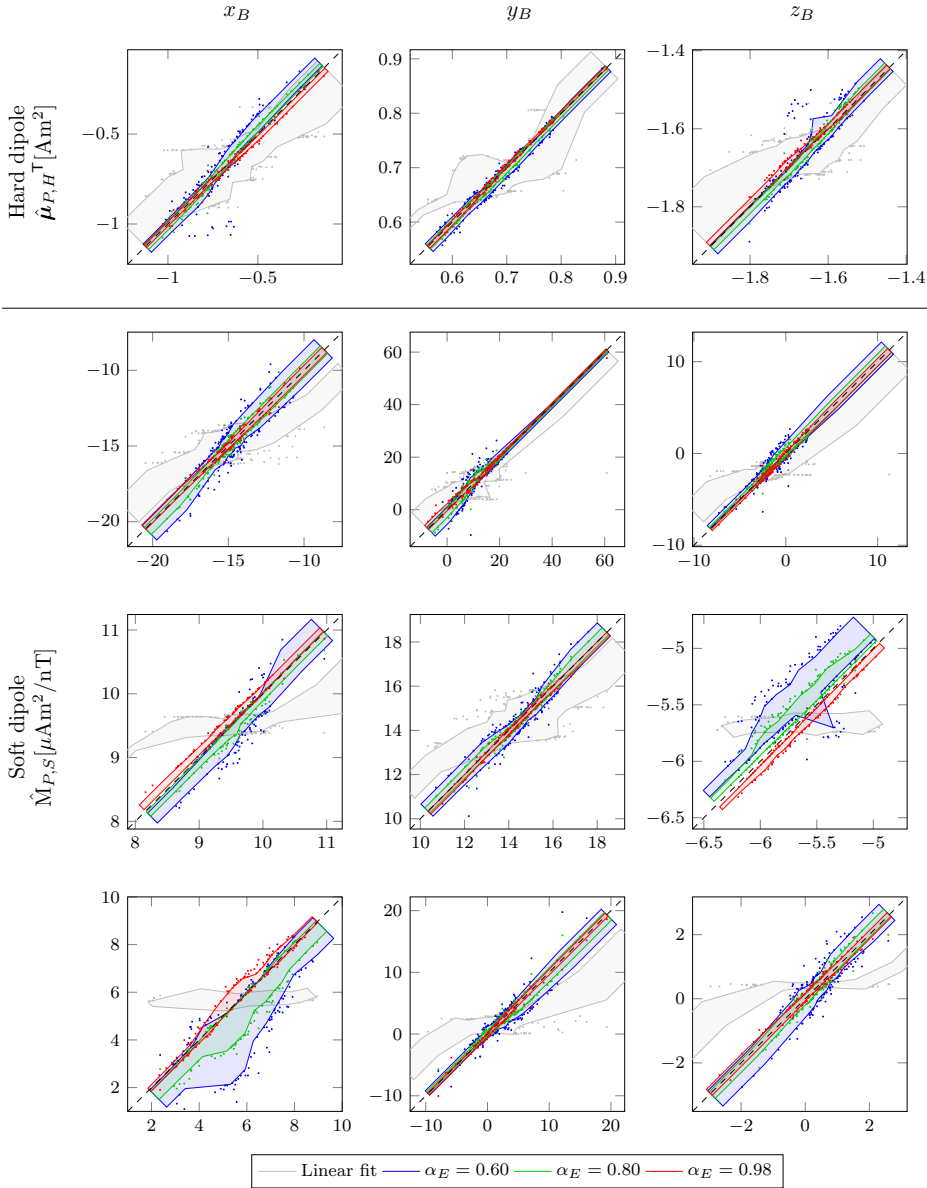


Figure 5.1: Estimated constant hard magnetic ( $\hat{\mu}_{P,H}$ , top) and soft magnetic dipoles ( $\hat{M}_{P,S}$ , bottom) for alternative accommodation coefficients (vertical axis), plotted against those derived for the default value of 0.93 (horizontal axis), in terms of the 5<sup>th</sup> and 95<sup>th</sup> percentile.

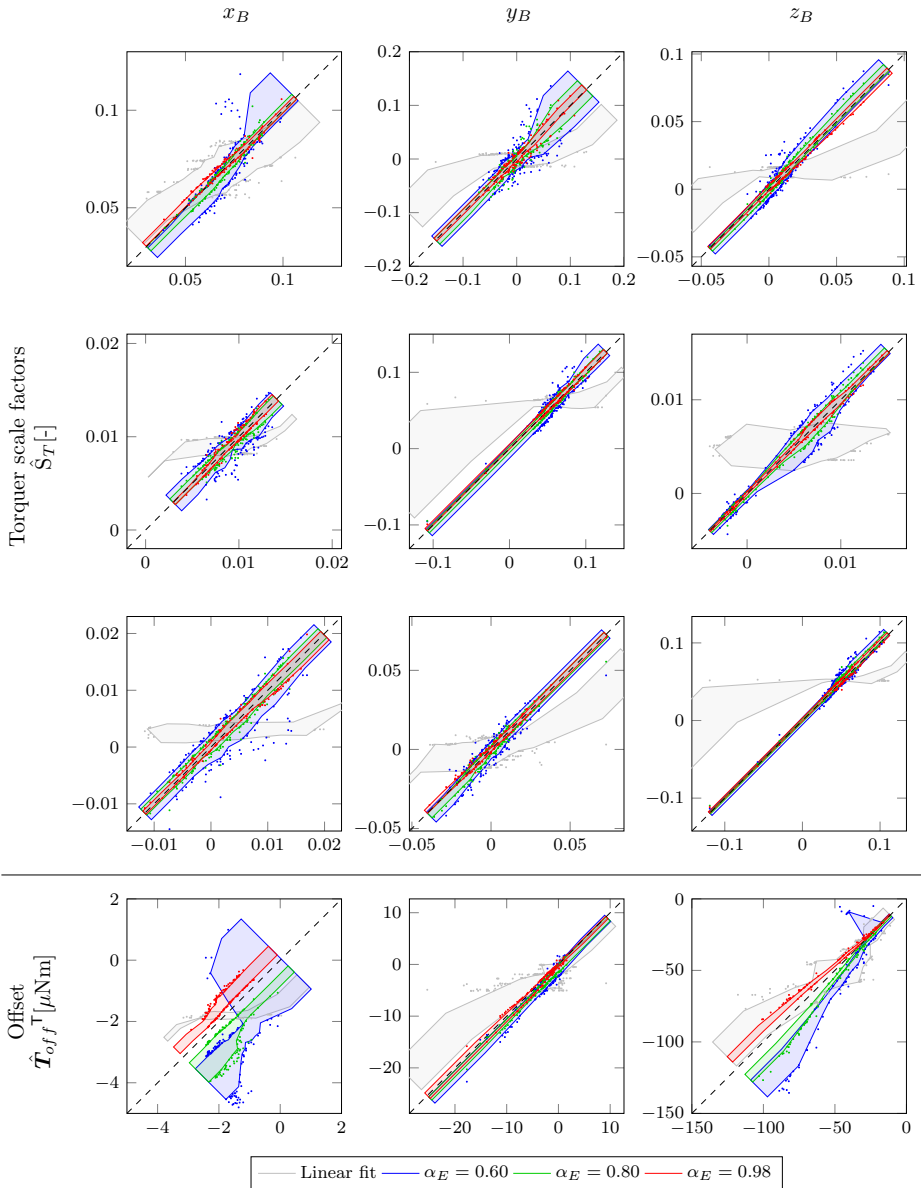


Figure 5.2: Estimated magnetic torquer scale factors ( $\hat{S}_T$ , top) and torque offsets ( $\hat{T}_{off}$ , bottom) for alternative accommodation coefficients (vertical axis), plotted against those derived for the default value of 0.93 (horizontal axis), in terms of the 5<sup>th</sup> and 95<sup>th</sup> percentile.

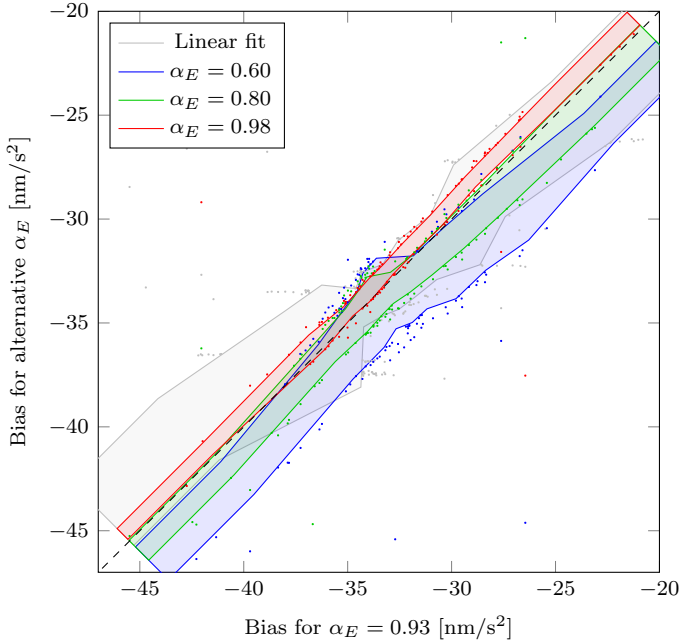


Figure 5.3: Vertical acceleration bias for alternative accommodation coefficients, plotted against those derived for the default value of 0.93, in terms of the 5<sup>th</sup> and 95<sup>th</sup> percentile. The axes bounds coincide with the outlier definition (as set in section 3.3).

of the linear fit. Still, the main difference is an offset from the default estimates. Compared to the difference with the orbit-derived acceleration biases (as plotted in Figure 3.5), the effect of the accommodation coefficient is negligible.

Finally, for the thruster misalignment angles  $\alpha$  and  $\beta$  (as defined in Figure 3.3), the difference between the new estimates and their default counterparts is plotted against the daily mean thrust in Figure 5.4. As for the magnetic dipoles, the spread of the difference is smaller than that around the default linear fit. The thruster  $\alpha$  seems to be mostly unaffected at thrust levels above 3 mN. At lower thrust, the thruster behavior is more erratic and other model errors find their way into the estimates. At the same time, a significant offset is observed for the  $\beta$  angles. Although the shift of  $-0.02^\circ$  for  $\alpha_E = 0.98$  is an improvement towards the documented value of  $\beta$ , it is insignificant compared to the remaining error between the two (cf. Figure 5.4).

### 5.3. AERODYNAMIC COEFFICIENTS

In section 3.5, the sensitivity of both the force- and torque-derived cross-wind to the accommodation coefficient was analyzed. In the search for an optimal accommodation coefficients however, the aim is to minimize the difference between these two data sets. Therefore the behavior and sensitivity of the difference between force- and torque-

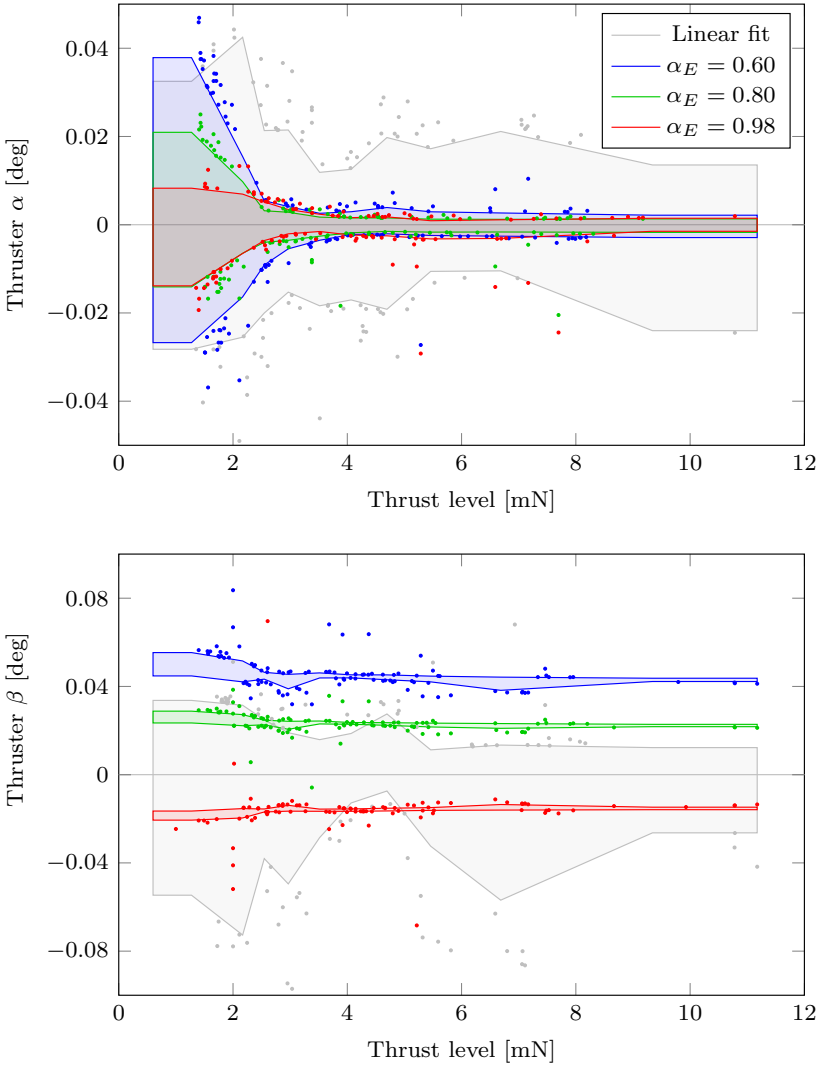


Figure 5.4: Difference between thruster misalignment angles  $\alpha$  (top) and  $\beta$  (bottom) derived for alternative accommodation coefficients with respect to the default value of 0.93, plotted against mean daily thrust in terms of the 5<sup>th</sup> and 95<sup>th</sup> percentile.

derived wind is investigated in this section.

### 5.3.1. METHODOLOGY

Using the SPARTA software, the aerodynamic force and moment coefficients can be derived for any value of the accommodation coefficient. This process is however rather time consuming. Therefore the results from [March et al. \(2019a\)](#) of the Monte Carlo simulations for accommodation 0.60, 0.85, and 1.00 are used to derive the linear relation suggested by [Fritsche et al. \(1998\)](#). From their Equation (4-5.6–4-5.9) we derive for any force and torque coefficient  $C$  the linear relation

$$C = C_i + C_r \sqrt{\frac{T_W}{T_{W_{\text{ref}}}}}, \quad (5.1)$$

where  $C_i$  and  $C_r$  are the contributions from incoming and re-emitted particles respectively,  $T_W$  is the wall temperature, and  $T_{W_{\text{ref}}}$  is the reference wall temperature used in the Monte Carlo simulation. This relation holds for the assumption of full accommodation. We can however adapt the wall temperature to obtain the aerodynamic coefficients for any accommodation, by taking the weighted sum of the two extremes for the kinetic temperature of the re-emitted particles  $T_{k,r}$ , derived by [Koppewallner \(2009\)](#).

$$T_{k,r} = T_{k,i} (1 - \alpha_E) + T_W \alpha_E, \quad (5.2)$$

where

$$T_{k,i} = \frac{1}{2} S^2 T_i \quad (5.3)$$

is the kinetic temperature of the incoming atmospheric particles, obtained from the atmospheric temperature  $T_i$  and the speed ratio of the particles  $S$  (defined as the ratio between the aerodynamic flow velocity divided by the most probable thermal velocity). Since the reference wall temperature was defined to be equal to the atmospheric temperature in the SPARTA simulations, we may combine the above to find

$$C = C_i + C_r \sqrt{\frac{T_{k,r}}{T_i}}, \quad (5.4)$$

with  $T_{k,r}$  defined by the wall temperature, speed ratio, and accommodation coefficient as described by Equation (5.2) and (5.3). The values of  $C_i$  and  $C_r$  for each angle of attack, angle of sideslip, and speed ratio are obtained from the total coefficient  $C$  through a least squares estimation. The reason for using the aerodynamic coefficients for three accommodation values is to reduce the effect of Monte Carlo noise. The method was validated and found to be accurate to the level of the Monte Carlo noise, by comparing the result with the original SPARTA coefficients for 0.93.

The aerodynamic coefficients can be used to determine the required consistency between force- and torque-derived wind to distinguish between accommodation coefficients. In this process, we first assume that the true value of  $\alpha_E$  is known to be 0.80, and that at a specific time instant the force- and torque-derived wind align perfectly, i.e. the aerodynamic incidence angles are identical. These assumptions provide

us the force coefficient vector  $C_F = [ C_X \ C_Y \ C_Z ]$  and the torque coefficient vector  $C_T = [ C_X \ 10C_m \ 10C_n ]$ , defined as in section 3.3. Then the accommodation coefficient is changed over a range of values, from 0.60 to 0.99. For each value, the incidence angles are changed such that either the force or the torque coefficient vector aligns with the original one, using the built-in interior-point algorithm of the Matlab `fmincon` function. This process results in new incidence angles, one  $(\alpha, \beta)$ -pair for the force vector, and one for the torque vector. Assuming a total flow velocity of 7.8 km/s, the horizontal and vertical wind can be calculated from these incidence angles, and the difference between the force- and torque-derived wind is found. Note that the assumed optimal accommodation value of 0.80 is chosen purely because it is the middle of the investigated domain.

### 5.3.2. RESULTS

With the linear description of the aerodynamic coefficients in Equation 5.4, the analysis described above can be performed with a high  $\alpha_E$ -resolution. The results are displayed in Figure 5.5, which shows the difference between force- and torque-derived horizontal wind for  $\alpha = 0^\circ$ ,  $\beta \in [-4^\circ, 0^\circ, 4^\circ]$ , and vertical wind for  $\alpha \in [-1^\circ, 0^\circ, 1^\circ]$ ,  $\beta = 0^\circ$ . These bounds correspond to the typical minimum and maximum incidence angles experienced by GOCE.

From the figures, we can read that if 0.80 is the true value of the accommodation coefficient, then the horizontal wind difference due to the error in the aerodynamic model with the default 0.93 accommodation, is in the order of 10 m/s. We also observe that this error is positive for both positive and negative  $\beta$ , and thus for both positive and negative horizontal wind. This suggests that the wind difference manifests itself primarily as a bias. Note that a bias of 10 m/s is very minor compared to the total wind measurement of 544 m/s at  $\beta = 4^\circ$  (assuming a total flow velocity of 7.8 km/s).

The vertical wind difference is of the same order of magnitude at  $\alpha = 1^\circ$  as the horizontal wind difference, but the sign of the vertical wind errors is opposite to the sign of  $\alpha$ , and thus to the sign of the vertical wind itself. This suggests that the relation between the vertical wind data sets can largely be described by a scale factor. This factor would be just under 10% at  $\alpha_E = 0.93$ , since the vertical wind at  $1^\circ$  angle of attack is approximately 135 m/s (again assuming a total velocity of 7.8 km/s).

## 5.4. WIND COMPARISON

Now that the sensitivity of the wind difference to the accommodation coefficient is known, the achieved consistency between force- and torque-derived wind is analyzed for four accommodation coefficient values: 0.60, 0.80, 0.93, and 0.98. As mentioned in chapter 3, a structural difference remains between the two horizontal wind sets, which closely follows the vertical magnetic field component. This difference may be explained by an electric dipole, but no source for an electric charge of sufficient magnitude was identified at the time. To prevent this signal from masking a real aerodynamic signal, the analysis in this section is performed both for the nominal wind data, and for data derived after estimating a constant electric dipole. The estimation procedure is described in subsection 5.4.1, the results of the wind analysis are presented in subsection 5.4.2.

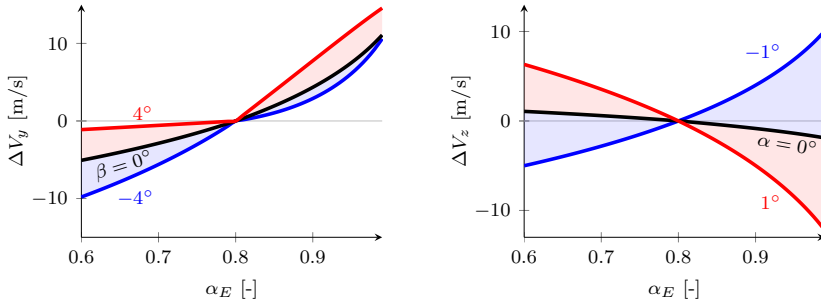


Figure 5.5: Effect of an off-optimal accommodation coefficient value on the difference between force- and torque derived horizontal ( $\Delta V_y$ , left) and vertical wind ( $\Delta V_z$ , right), assuming the optimum is at 0.80.

### 5.4.1. METHODOLOGY

The estimation process for the electric dipole is identical to (and simultaneous with) the magnetic dipole estimation described in section 2.3.6. The electric dipole torque  $\mathbf{T}_E$  is defined as

$$\mathbf{T}_E = \mathbf{r} \times (q\mathbf{V} \times \mathbf{B}_E), \quad (5.5)$$

with  $\mathbf{r}$  the moment arm,  $q$  the charge,  $\mathbf{V}$  the orbital velocity, and  $\mathbf{B}_E$  the Earth's magnetic field. To estimate the electric dipole  $q\mathbf{r}$ , a new term is added to Equation (2.13) of the form of the first right-hand side term, substituting  $q\mathbf{r}$  for  $\boldsymbol{\mu}_{P,H}$ , and the cross-product matrix of the vector  $\mathbf{V} \times \mathbf{B}_E$  for  $\mathbf{B}_{E,H}$ . This estimation is only performed after estimating the acceleration bias and thruster misalignment angles. A linear fit is made to the daily estimates for the entire mission, in line with the fits to the magnetic parameters. This linear trend runs from  $[-20.4 \ 19.5 \ -2.2] \mu\text{Cm}$  on 2 November 2009 to  $[-57.8 \ 19.8 \ -26.5] \mu\text{Cm}$  on 30 September 2013. Note that the lateral magnetic field is generally small due to GOCE's polar orbit, and the yaw torque is therefore dominated by the product of the vertical field component and the lateral ( $y$ ) body component of  $q\mathbf{r}$ . It is especially this component of the electric dipole that is very consistent throughout the mission.

When the electric dipole is estimated along with the magnetic parameters, the latter also differ from the original values presented before. Most notably, all magnetic torquer scale factors are reduced to the order of  $10^{-7}$  (cf. Figure 2.4). This suggests that no scaling or rotation of the magnetic torquer output is required from the documented model. Although this is a strong indication that an electric dipole should be included, no source has been found for this dipole so far. From a first order calculation, we found that the accelerator grid of the ion thruster creates an electric dipole of the order of  $10^{-2} \mu\text{Cm}$ , several orders of magnitude smaller than the required dipole. If part of the satellite wall is not properly discharged, it may charge up to several hundreds of volts (Anderson, 2012, e.g.). Assuming the wall is covered by  $50 \mu\text{m}$  kapton foil (with a dielectric constant of 3.4), a first order calculation shows that a charge of  $60 \mu\text{C}/\text{m}^2$  may build up (assuming a potential of 100 V). Considering the size of GOCE (a 5 m long, 1.1 m diameter cylinder with 1 m wide wings), the estimated electric dipole could thus be explained by charging of the

front panel or of (part of) the solar array. A more detailed analysis of GOCE's charging budget and characteristics is however required to make a conclusive argument for it.

After deriving the horizontal and vertical wind for the four accommodation values, the force- and torque-derived wind are compared for each day of the mission. In this comparison, a least squares estimate is made of a bias and linear scale factor that best describe the relation between the two wind data sets. As illustrated in section 3.4, the vertical wind data sets are best compared at high frequencies. Therefore both sets are high-pass filtered with a third-order Butterworth filter, rejecting frequencies below ten times the orbit frequency, before further processing.

#### 5.4.2. RESULTS

The force- and torque-derived wind on 2 March 2013 are compared in Figure 5.6 for accommodation coefficient 0.93, both excluding and including the electric dipole model. In each bin the transparency of the color indicates how many data points it contains, compared to the most densely packed bin. If a bin is filled for less than 5%, it is kept 5% opaque. The line indicates the convex hull of the data. It is clear from the top left panel that without the electric dipole, the horizontal wind is divided in two lobes that strongly adhere to the magnetic hemispheres. This is consistent with the observation that the wind difference correlates well with the vertical magnetic field component. Adding the electric dipole model removes the two-lobed structure completely. The addition seems to have little effect on the consistency of the filtered vertical wind component.

The daily estimates of bias and linear scale factor between the force- and torque-derived wind are collected for the full mission in probability density plots in Figure 5.7 and 5.8 respectively. We observe that these plots confirm the observation made in section 5.3 that an off-optimal accommodation coefficient causes a bias in the horizontal, but a scale factor in the vertical wind component. Irrespective of the electric dipole model, the horizontal wind bias increases with accommodation, while the scale factor stays constant when the electric dipole is included. The change in scale factor without the electric dipole can be explained by the imbalance between the Northern and Southern hemispheres. As accommodation decreases, Southern hemisphere torque-derived winds will increase, compensating for the upward magnetic field component, while the Northern hemisphere torque-derived winds decrease, compensating for the downward magnetic field component. The two lobes moving apart causes the linear scale factor to rise.

Considering the horizontal wind bias, no optimal accommodation coefficient can be selected. Excluding the electric dipole, Figure 5.7 suggests an optimum can be found between 0.80 and 0.93, but all peaks lie within the 10 m/s uncertainty bounds of other parameters, as was suggested before in section 5.3. When the electric dipole is included, the biases shift to more positive values and the probability distributions for 0.60–0.93 are spread out over a wider range. We expect that this is due to a mismatch with the estimated thruster misalignment angles. If the electric dipole was also included before estimating those angles, the offset would most likely be removed. Any bias between the vertical wind components would have been removed by the high-pass filter, and is therefore not considered here.

The linear scale factors in Figure 5.8 provide more insight. From the top right panel,

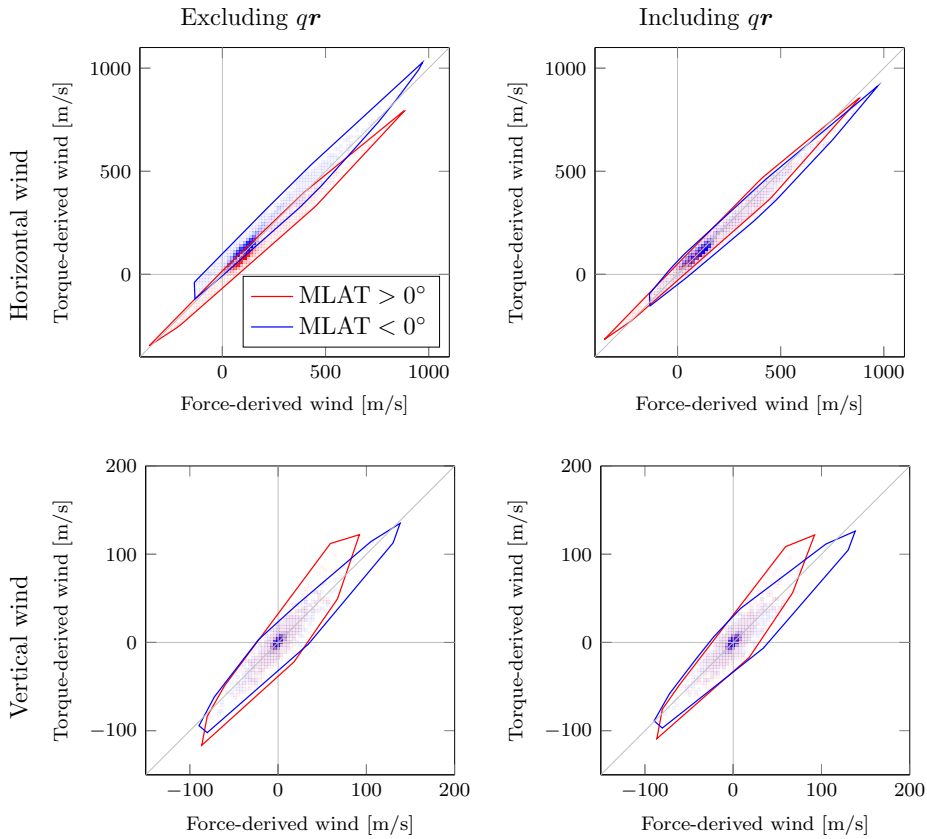


Figure 5.6: Torque-derived horizontal and filtered vertical wind on 2 March 2013 plotted against its force-derived counterpart, in terms of the data distribution and convex hull for the magnetic Northern and Southern hemisphere. The left and right column respectively exclude and include the model for a constant electric dipole.

the horizontal wind scale factor is found to be centered around 0.9 for all accommodation coefficients. This suggests that a structural error persists between the two wind data sets. Looking at the top right panel of Figure 5.6, we find that the data is densely packed around the linear trend defined by the bias and scale factor. Therefore it is likely that the structural error lies in the aerodynamic model, for example in the geometry model. The vertical wind scale factors are more spread out in general, but do reveal very clear optima:  $\alpha_E \approx 0.93$  excluding and  $\alpha_E \approx 0.80$  including the electric dipole. Note that for 0.93 the force-derived vertical wind was already validated against other satellite data in chapter 4. It is unclear however, how the structural error in the horizontal wind translates to the vertical component.

## 5.5. CONCLUSION

The comparison of the estimated non-aerodynamic parameters for four different accommodation coefficients does not provide a conclusive result. In most cases, the change in the daily estimates is smaller than the error of the linear fit for  $\alpha_E = 0.93$ . The only exception is the thruster  $\beta$  angle, which shows a tendency to offset from the default estimates. These offsets are however too small to speak of a significant improvement with respect to the documented thruster angles.

The analysis of the aerodynamic coefficients reveals that only small differences are to be expected between force- and torque-derived wind in case of a suboptimal choice for accommodation. Assuming the optimum lies at 0.80, a value of 0.93 results in an offset of the order of 10 m/s in horizontal wind. This error is of the same order of magnitude as the uncertainty due to the linear fit to the thruster  $\beta$  angle (see Table 3.5). In fact, since the thruster angles are estimated such that the wind difference is reduced, the offset between the thruster  $\beta$  estimates for different accommodations compensates for the change due to the aerodynamic model. This brings the search for an optimal accommodation coefficient back to the thruster misalignment. The daily estimates for the bias between force- and torque-derived horizontal winds confirm this conclusion. When an electric dipole is included in the estimation process, the biases differ only by a few meters per second for different accommodation coefficient values. The scale factors in this case, are centered around 0.9, suggesting a structural inconsistency between the aerodynamic force and torque models that cannot be explained by  $\alpha_E$ .

For the vertical wind component, a suboptimal accommodation coefficient primarily results in a scale factor between force- and torque-derived wind. Under nominal conditions, the scale factor may deviate from unity by up to 10%, assuming an optimal accommodation value of 0.80. Such values are indeed observed in the daily scale factor estimates. Depending on whether an electric dipole is included, the scale factors are centered around unity for accommodation values between 0.80 and 0.93. Apart from providing an indication of an optimal accommodation coefficient, these results clearly show how sensitive the procedure is to assumptions made in the torque modeling process. On top of that, the structural inconsistency between the horizontal wind data sets may also hold for the vertical wind.

Combining all results presented in this chapter, we conclude that no optimal accommodation coefficient can be found based on the consistency between the GOCE linear and angular accelerations. The difference between the force- and torque-derived hori-

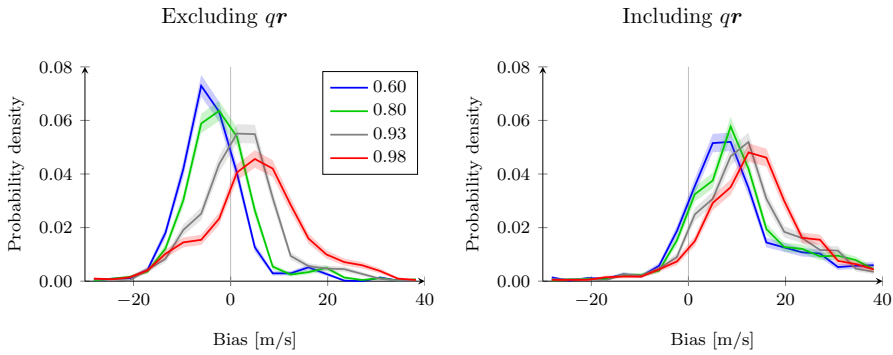


Figure 5.7: Probability distribution of the bias between force- and torque-derived horizontal wind for four accommodation coefficient values, both excluding (left) and including (right) the electric dipole. The bias between the vertical winds is removed by the high-pass filter, and therefore not plotted here.

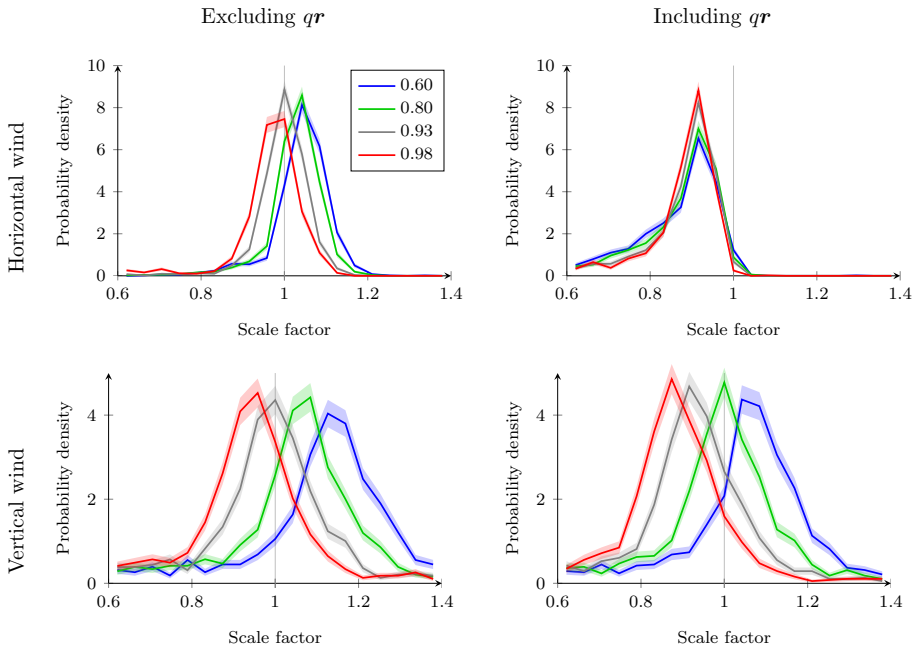


Figure 5.8: Probability distribution of the scale factor between force- and torque-derived horizontal (top) and high-pass filtered vertical wind (bottom) for four accommodation coefficient values, both excluding (left) and including (right) the electric dipole.

zontal wind is more sensitive to other parameters, most notably the thruster misalignment angle. As both  $\alpha_E$  and the thruster  $\beta$  angle cause a bias between the two sets, a better model of the thruster behavior is required to draw conclusions about the aerodynamic model. Because of the small magnitude of the aerodynamic signal in pitch, the vertical wind component is quite inconsistent to start with. Only after high-pass filtering can the two data sets be compared. Due to the inconsistency between the horizontal wind data sets however, it is unclear whether a unity scale factor for the vertical component corresponds to the optimal accommodation coefficient.

For both components, a small change in the torque models (such as the addition of the electric dipole in this chapter) has a significant impact. This confirms our recommendation in section 3.6 that a complete magnetic and electric budget is required if the aerodynamic model or thermospheric data are to be improved through simultaneous observation of the linear and angular accelerations of a satellite.

On the other hand, the GOCE geometry is very clean and produces practically no aerodynamic moment at zero force. We expect that if a satellite geometry were to produce a zero-force moment, the difference between force- and torque-derived wind may be more sensitive to the accommodation coefficient. Examples of such geometries are the paddewheel satellites (producing a rolling moment at zero lateral or vertical force), but also the CHAMP satellite (producing a pitching moment with its inclined front panel). An added benefit of these less symmetric geometries (also including e.g. GRACE and Swarm), is that a rolling moment is produced by the horizontal cross-wind on the inclined sides (or the paddewheel fins). This adds another aerodynamic measurement, and therefore the opportunity to also estimate the density from the torques independently from the longitudinal force.

All things considered, we recommend that, if and only if a complete magnetic and electric budget is available, a full analysis of either of the aforementioned missions is considered. As a starting point for such an investigation, the sensitivity of the difference between force- and torque-derived wind (and possibly density) to the accommodation coefficient should be determined from an analysis like the one described in section 5.3. Since the vertical wind is generally small, especially a large sensitivity of the horizontal component would justify a complete study of a different satellite than GOCE.

# 6

## CONCLUSION

In chapters 2–5 conclusions have been drawn regarding the results in the respective chapters. The purpose of this chapter is to first combine those conclusions to answer the research questions posed in section 1.5, and reflect on the overall research goal. This is done in section 6.1. Second, in section 6.2, recommendations are made for future research. This concerns both research into the attitude motion of GOCE, and more general recommendations for satellite-based studies of the thermosphere.

### 6.1. RESEARCH QUESTIONS AND GOAL

To reflect on the research goal in a structured manner, the research questions posed in section 1.5 are answered first. These answers are based on the concluding sections of the previous chapters.

In chapter 2, an analysis was made of the most significant torques acting on the GOCE satellite. This results in the answer to question 1: the significant torques acting on a LEO satellite are the control, aerodynamic, solar and Earth radiation pressure, passive magnetic, induced magnetic (by currents in the satellite), gravity gradient, and thruster misalignment torques. It is important to note that not all torques are significant for all LEO satellites. A satellite without continuous thrusting, for example, would not experience thruster misalignment torque. Similarly, a spherical satellite would most likely not experience a significant gravity gradient torque. In studying the wind in chapter 4 and 5, it was found that satellite charging could explain the mismatch between force- and torque-derived horizontal wind. If charging of the front or back panel can be validated for GOCE, the resulting torque should therefore be added to the above list. Apart from that, the most significant torque may be different for each rotational direction. In the case of GOCE, aerodynamic torques are the most significant contribution in yaw, while magnetic torques dominate the pitch and roll axes. Depending on the satellite design, this may be very different for other satellites.

In the same chapter 2, the accuracy of the collective torque model is evaluated. This allows us to answer question 2: the accuracy of the total torque model depends heavily

on the most significant torque. For the strictly controlled pitch axis the root mean square error was found to be only 2% of the standard deviation of the largest torque (i.e. the control torque). Aerodynamic torques are especially small in this direction, while they dominate the yaw motion. In that axis the error reaches levels exceeding 30%. Based on the behavior of this error in latitude and its response to geomagnetic activity, it may be concluded that the error stems from a mismatch between the aerodynamic model and the thermospheric density and wind data. Assuming that the new aerodynamic model is more accurate than the panel model with which the original thermospheric data was derived, the error lies primarily in the thermospheric data. This finding confirms the limitation of accelerometer-derived density and wind measurements: their quality is limited by that of the aerodynamic model. When the aerodynamic model and the thermospheric data do match (as is the case when the thermospheric data is estimated in chapter 3), other models turn out to cause large uncertainties. Most important is the thruster misalignment torque, which turned out to be exceptionally sensitive to the alignment angles. Within the documented error margins, an offset in excess of 1000 m/s can be expected. This shows that continuous thrusting is the primary limitation to estimating thermospheric wind from angular accelerations.

To answer question 3, an algorithm has been developed with which density and wind can be derived from an arbitrary combination of force and torque residuals. In this algorithm the residual force and/or torque is reduced to zero by iteratively changing the direction of the incoming flow. Internally the algorithm works with the angular difference between the aerodynamic and residual force and/or torque, to prevent gimbal lock. In the specific case of GOCE, it was found that forces and torques are not generally linearly independent. Density is primarily reflected by the longitudinal force, horizontal wind by the lateral force and yaw torque, and vertical wind by the vertical force and pitch torque. The aerodynamic signal in the roll torque is insufficient to obtain any thermospheric information. These limitations should be considered when selecting three force and torque components to be processed. It also means that the density can not be derived from torques alone, and its internal consistency could therefore not be investigated in this way. It was noted in section 5.5 that other satellites, especially those with slanted sides, may experience a significant aerodynamic roll torque, and could therefore be selected for a future study. This is discussed in more detail in section 6.2.

Using the results of the aforementioned algorithm, we can compare the force- and torque-derived wind to answer question 4. First, however, it is important to explain why a comparison with the force-derived wind is considered the best way to evaluate the accuracy of the torque-derived wind. First, it is convenient and especially fair to compare two data sets that were obtained under identical conditions, at the same place and time. Second, in this thesis we are especially interested in the internal consistency of accelerometer-derived wind data. By comparing with force-derived data, most errors in the aerodynamic model are expected to cancel (or even lead to improvements of the aerodynamic model, as discussed hereafter). When comparing the force- and torque derived wind in chapter 3, a close match between the two was found in the horizontal component. In general, the difference between the two does not exceed 100 m/s, which is less than 10% of the maximum horizontal wind observed. The trend in the difference suggests that an electric charge in or on the satellite and an unmodelled effect depending

on the solar incidence angle are the main contributors to the error. In section 5.4 a first order calculation was made to check whether the charge on the satellite wall could be large enough to explain the main difference between the Northern and Southern hemisphere. It was found that it might be, if the charge were concentrated on the front or back panel, or otherwise concentrated away from the center of mass in the longitudinal direction. The difference between the vertical components was found to be significantly larger in an absolute sense. Because the vertical wind is itself approximately one order of magnitude smaller than the horizontal one, this results in a much larger relative error. The largest errors in torque-derived wind are caused by the thruster, either due to its erratic behavior in low-thrust conditions (introducing noise around polar passes) or because of its high sensitivity to the alignment angles (primarily introducing a large bias). After high-pass filtering both data sets however, the short-lived peaks that characterize the vertical wind in the thermosphere were found to align very well.

Because most differences between force- and torque-derived vertical wind can be related to errors in the latter, the force-derived wind was validated against mass spectrometry data in chapter 4 to answer question 5. Due to the erratic nature of vertical wind, consisting primarily of short-lived small-scale peaks in the auroral and polar cap zones, a direct comparison of wind data is impractical. Therefore the vertical wind activity was defined as the 120-second central moving-window standard deviation of the vertical wind component. This parameter was calculated for all data of Atmosphere Explorer (AE) C and E, Dynamics Explorer 2 (DE-2), and GOCE. By comparing the result for a range of parameters, carefully selecting the range of driving parameters, it was found that the GOCE measurements align with DE-2 within 5% scale factor over the polar cap for all geomagnetic activities, and 6% in the auroral latitudes for high activity. When geomagnetic activity reduces, the scale factor suggests that GOCE underestimates the wind activity with up to 21% in this latitude regime. A further comparison with also the AE satellites reveals that GOCE corresponds well with AE-E at equatorial latitudes, but better with DE-2 at mid-latitudes. As these last results lie close to the total error level reported for the different measurement techniques, we may only conclude that the vertical wind activity is validated at the high latitudes, especially at high geomagnetic activity levels. It is important to note that in chapter 5 we suggest to lower the accommodation coefficient from its default value of 0.93. This would reduce the magnitude of the wind, and therefore the vertical wind activity. If it were decided to do this, the validation would have to be repeated. However, given the fact that GOCE already underestimates the activity in most cases, an improvement is not to be expected.

Note that the statistical analysis of the vertical wind data in chapter 4 was extended beyond the validation effort. This led to the additional conclusion that vertical wind activity primarily depends on latitude, magnetic local time, geomagnetic activity, and seasonal effects. The first three are clearly interconnected, as the activity peaks in the polar cap and auroral oval, in the midnight–dawn sector, at high values of the Auroral Electrojet (AE) index. The most important result however, is that this response levels out for values of AE above approximately 800. This indicates that the response of the thermosphere to geomagnetic storms will not increase monotonically with the strength of the storm.

Referring back to question 4, several unexplained differences are still present be-

6

tween force- and torque-derived winds. The question remains how these differences impact the possibility of improving the aerodynamic model and thermospheric data, as suggested in question 6. Answering this question was the goal of chapter 5. First, the sensitivity of the various non-aerodynamic parameters that were estimated throughout the data processing, to changes in the aerodynamic model was investigated. It was found that this sensitivity in case of the energy accommodation coefficient was generally smaller than the error of the linear fit to the parameter estimates. The only exception was the thruster angle in the horizontal plane ( $\beta$ ), which is offset by changes in the accommodation coefficient. As the documented value of this parameter is relatively far from the estimates, it is however not possible to select an optimal result. Looking more closely at the aerodynamic model, the sensitivity of the difference between force- and torque-derived wind to the accommodation coefficient could be determined. This sensitivity was found to be of similar magnitude as that to the thruster misalignment angles. A large part of the effect of the accommodation coefficient may therefore be canceled by a new estimate for the thruster angles. Finally a linear scale factor and bias between force- and torque-derived wind were estimated for each day of the mission, for several different accommodation coefficients. Analyzing these estimates, it was concluded that a systematic error may still exist in the aerodynamic model, as the horizontal wind scale factors were all centered around 0.9 instead of unity. The biases deviated only by a few meters per second due to accommodation, presenting no conclusive evidence for an optimal accommodation coefficient value. Only in the scale factors of the vertical wind an optimum may be observed. Due to the large uncertainty and sensitivity of especially the torque-derived vertical wind, this result was insufficient to draw a conclusion on the matter. We can therefore answer this question by stating that at this point, the fidelity of the torque models of GOCE is still insufficient to improve the aerodynamic model or thermospheric data using simultaneous observation of its linear and angular dynamics. Since GOCE has a very clean and symmetric aerodynamic design, it is very well possible that this does not hold for other satellites. This is discussed in some detail in section 6.2.

Having answered all research questions, we find ourselves in a good position to reflect on the overarching goal of this thesis work. The first part of the goal was twofold: to (1) improve our estimates of aerodynamic parameters and (2) assess the quality of accelerometer-derived thermospheric wind data; and so was the second part: by (A) adding the angular accelerations of the GOCE satellite as a source of wind data, and (B) comparing these data to those derived from linear accelerations. The approach in the second part of the goal can in general be described as a success. The thermospheric wind was derived from angular accelerations, with especially promising results for the horizontal component. Because the aerodynamic signal was too small in the roll direction, no separate measurements of the density could be obtained. In a comparison of the force- and torque-derived wind, only small systematic errors were observed. Because of the small magnitude of the vertical wind, the low frequency signals in the wind could not be matched between the two data sets. These observations also relate to the first part of the goal, assessing the quality of the accelerometer-derived wind data. Both in the horizontal and the vertical cross-wind component the main features (horizontal flow reversal and vertical wind peaks) are confirmed by the torque-derived data. Especially for the vertical wind this is an important result, as measurements of this component are

scarce. Improving the estimates of aerodynamic parameters however, proved impossible for GOCE with the current state of disturbance models. The clean design of GOCE just does not provide a large enough difference between force- and torque-derived wind to overpower the sensitivity to other model uncertainties.

All in all, the output from this thesis work consists of three parts. First, an algorithm has been described with which horizontal and vertical wind, as well as neutral density, can be derived from the linear and/or angular accelerations of a satellite. Conditions have been formulated for the successful application of this algorithm, mainly pertaining to the linear (in)dependence of the separate force and torque measurements. If these conditions are met, the algorithm may be applied to any LEO satellite. Second, the required accuracy of torque models for the derivation of thermospheric wind has been studied. A sensitivity study showed that especially continuous thrusting causes difficulties in this context. On top of that, several results have revealed that the magnetic and electric budget of a medium-size satellite like GOCE are of vital importance for this work. Finally, this work has resulted in the first modern validated accelerometer-derived vertical wind data set, which is now publicly available. Considering that the vertical wind component was often ignored or assumed zero in the past, this new data set may aid atmosphere researchers and modelers to improve our understanding of thermosphere dynamics.

## 6.2. RECOMMENDATIONS

Deriving from the conclusions, many recommendations can be made for future research. First we briefly formulate the recommendations pertaining to the GOCE mission, before turning our attention to other past, current, and future satellite missions.

As pointed out before, the torque models of the GOCE satellite presented in this work can be improved in several ways. Given its sensitivity, the thruster misalignment model requires further validation. An explanation has to be given for the change in the dependence of the alignment angles on thrust level, that occurs over the orbit maneuver of August 2012. The magnetic budget also requires an update, to include the magnetic effects of the currents running through the satellite, particularly from the solar panels. A further improvement of wind consistency can be expected from adding a model of satellite charging, or of other electric charge build-up on-board. At the same time however, we have already arrived at a point in the torque modeling process where the wind output serves to improve the torque models. If the goal remains to improve the consistency of thermospheric data through simultaneous observation of linear and angular dynamics, it is of vital importance that as few as possible parameters are estimated in this way. Therefore we recommend that if newly added models require extensive parameter estimation, that the GOCE mission is abandoned for this purpose.

Except for its exceptionally low altitude, and therefore high aerodynamic signal, GOCE may be one of the least suited missions for simultaneous observation of linear and angular aerodynamics. Other accelerometer carrying LEO satellites — mainly CHAMP, GRACE and Swarm — have much more suitable geometries for such investigations. Especially the asymmetric slanted sides, which provide a strong roll signal in the case of non-zero sideslip, are a valuable addition to this work. The CHAMP satellite adds to that a slanted front panel and boom, which are likely to remove dependencies between linear

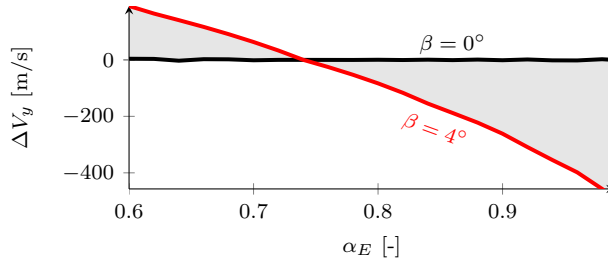


Figure 6.1: The difference between the force- and torque-derived wind  $\Delta V_y$  derived from CHAMP measurements as a function of accommodation coefficient, assuming the optimum lies at  $\alpha_E = 0.74$ .

and angular accelerations, potentially making it a more suitable mission for the goal of this thesis. This is illustrated in Figure 6.1, where the analysis of section 5.3 is repeated for the horizontal wind as measured by CHAMP, using the roll torque instead of the longitudinal force in the triplet of torques (cf. Figure 5.5). It is immediately clear that the difference between force- and torque-derived wind is much more sensitive to the accommodation coefficient for this satellite than it is for GOCE. Added benefit of all three alternative satellite missions is that they do (or did) not apply continuous thrusting. On top of that, because of the geomagnetic mission goals of both CHAMP and Swarm, detailed information is likely available about the magnetic and electric budget of both these missions. We therefore recommend that one of these missions is considered for a similar study as described in this work. Since the aerodynamic signal is smaller at the higher altitude of these satellites, the vertical wind component should most likely be excluded from such a study.

Taking a broader view of thermosphere research in general, one of the most important challenges for the future is to align the different measurement techniques. In this work we have made an effort to compare mass spectrometer-derived wind with data derived from accelerations, and others have included FPI measurements as well. On the Explorer missions these three different instruments were sometimes combined, but generally to measure different components of the wind. It is highly recommendable that a future mission combines at least a mass spectrometer and accelerometers to validate the density measurements of the latter. A combination of a cross-track pointed FPI, spectrometer with horizontally scanning baffle, and a combination of linear and angular acceleration measurements on a single platform would be of great value to the field and has the potential to improve all thermospheric data generated in the past.

## REFERENCES

- Agrawal, A., and S. Prabhu (2008), Survey on measurement of tangential momentum accommodation coefficient, *Journal of Vacuum Science & Technology A*, 26(4), doi: 10.1116/1.2943641.
- Anderson, C., M. Conde, and M. McHarg (2012), Neutral thermospheric dynamics observed with two scanning Doppler imagers: 2. Vertical winds, *Journal of Geophysical Research*, 117(A03305), doi: 10.1029/2011JA017157.
- Anderson, P. (2012), Characteristics of spacecraft charging in low earth orbit, *Journal of Geophysical Research*, 117(A07308), 1–11, doi: 10.1029/2011JA016875.
- Aruliah, A., and D. Rees (1995), The trouble with thermospheric vertical winds: geomagnetic, seasonal and solar cycle dependence at high latitudes, *Journal of Atmospheric and Terrestrial Physics*, 57(6), 597–609, doi: 10.1016/0021-9169(94)00100-3.
- Bandikova, T., J. Flury, and U.-D. Ko (2012), Characteristics and accuracies of the GRACE inter-satellite pointing, *Advances in Space Research*, 50(1), 123–135, doi: 10.1016/j.asr.2012.03.011.
- Bird, G. (1994), *Molecular gas dynamics and the direct simulation of gas flows*, vol. 42, Oxford Scientific Publications.
- Bowman, B., and K. Moe (2005), Drag coefficient variability at 175–500 km from the orbit decay analysis of spheres, in *Astrodynamics Specialist Conference*, AAS 05-257, AAS/AIAA, San Diego, CA.
- Bruinsma, S., D. Tamagnan, and R. Biancale (2004), Atmospheric densities derived from CHAMP/STAR accelerometer observations, *Planetary and Space Science*, 52, 297–312, doi: 10.1016/j.pss.2003.11.004.
- Cercignani, C., and M. Lampis (1971), Kinetic models for gas–surface interactions, *Transport Theory and Statistical Physics*, 1(2), 101–114, doi: 10.1080/00411457108231440.
- Cheng, M., B. Tapley, S. Bettadpur, and J. Ries (2008), Determination of thermospheric winds from GRACE accelerometer data, in *Advances in the Astronautical Sciences*, vol. 130, pp. 1181–1192.
- Chu, X., J. Zhao, X. Lu, V. Harvey, R. Jones, E. Becker, C. Chen, W. Fong, Z. Yu, B. Roberts, and A. Dörnbrack (2018), Lidar observations of stratospheric gravity waves from 2011 to 2015 at McMurdo (77.84°S, 166.69°E), Antarctica: 2. Potential energy densities, log-normal distributions, and seasonal variations, *Journal of Geophysical Research: Atmospheres*, 123(15), 7910–7934, doi: 10.1029/2017JD027386.

- Cometto, F. (2007), GOCE Models Data Bank, *Tech. Rep. GO-TN-AI-0081\_6*, Alenia Spazio.
- Dhadly, M., J. Emmert, D. Drob, M. Conde, E. Doornbos, G. Shepherd, J. Makela, Q. Wu, R. Niciejewski, and A. Ridley (2017), Seasonal dependence of northern high-latitude upper thermospheric winds: A quiet time climatological study based on ground-based and space-based measurements, *Journal of Geophysical Research: Space Physics*, 122(2), 2619–2644, doi: 10.1002/2016JA023688.
- Dhadly, M., J. Emmert, D. Drob, M. Conde, E. Doornbos, G. Shepherd, J. Makela, Q. Wu, R. Niciejewski, and A. Ridley (2018), Seasonal dependence of geomagnetic active-time northern high-latitude upper thermospheric winds, *Journal of Geophysical Research: Space Physics*, 123(1), 739–754, doi: 10.1002/2017JA024715.
- Doornbos, E. (2011), *Thermospheric Density and Wind Determination from Satellite Dynamics*, Springer, Berlin, Heidelberg, Germany, doi: 10.1007/978-3-642-25129-0.
- Doornbos, E. (2016), *GOCE+ Theme 3: Air density and wind retrieval using GOCE data: Data set user manual*, Delft University of Technology.
- Doornbos, E., M. Foerster, B. Fritsche, T. Van Helleputte, J. van den IJssel, G. Koppenwallner, H. Lühr, D. Rees, and P. Visser (2009), ESTEC contract 21022/07/NL/HE air density models derived from multi-satellite drag observations - Final report, pp. 7–39.
- Doornbos, E., J. van den IJssel, H. Lühr, M. Förster, and G. Koppenwallner (2010), Neutral density and crosswind determination from arbitrarily oriented multi-axis accelerometers on satellite, *Journal of Spacecraft and Rockets*, 47(4), 580–589, doi: 10.2514/1.48114.
- Drinkwater, M., R. Floborghagen, and R. Haagmans (2003), GOCE: ESA's first Earth Explorer Core mission, in *Earth gravity field from space - from sensors to Earth sciences*, Space Sciences Series of ISSI, pp. 419–432.
- Drob, D., J. Emmert, J. Meriwether, J. Makela, E. Doornbos, M. Conde, G. Hernandez, J. Noto, K. Zawdie, S. McDonald, J. Huba, and J. Klenzing (2015), An update to the Horizontal Wind Model (HWM): the quiet time thermosphere, *Earth and Space Science*, 2(7), 301–319, doi: 10.1002/2014EA000089.
- Dumontel, M. (2010), GOCE Stand-alone Aerodynamic Model How-to, *Tech. Rep. GO-TN-AI-0179*, ThalesAlenia Space.
- Emmert, J. (2015), Thermospheric mass density: A review, *Advances in Space Research*, 56(5), 773–824, doi: 10.1016/j.asr.2015.05.038.
- Falin, J., F. Barlier, and G. Kockarts (1981), Densities from the CACTUS accelerometer as an external test of the validity of the thermospheric models, *Advances in Space Research*, 1(12), 221–225, doi: 10.1016/0273-1177(81)90436-1.
- Fehringer, M., G. Andre, D. Lamarre, and D. Maeusli (2008), A jewel in ESA's crown, *ESA bulletin*, pp. 14–23.

- Floberghagen, R., M. Fehringer, D. Lamarre, D. Muzi, B. Frommknecht, C. Steiger, J. Piñeiro, and A. da Costa (2011), Mission design, operation and exploitation of the Gravity field and steady-state Ocean Circulation Explorer mission, *Journal of Geodesy*, 85(11), 749–758, doi: 10.1007/s00190-011-0498-3.
- Fritsche, B., and H. Klinkrad (2004), Accurate predictions of non-gravitational forces for precise orbit determination part I: principles of the computation of coefficients of force and torque, in *AIAA/AAS Astrodynamics Specialist Conference and Exhibit*, doi: 10.2514/6.2004-5461.
- Fritsche, B., M. Ivanov, A. Kashkovsky, G. Koppenwallner, A. Kudryavtsev, U. Voskoboinikov, and G. Zhukova (1998), Radiation pressure forces on complex spacecraft; final report, *Tech. Rep. (ESOC) 11908/96/D/IM*, Hypersonic Technology Göttingen (HTG)/ Institute of Theoretical and Applied Mechanics (ITAM).
- Fuller-Rowell, T. (1998), The “thermospheric spoon”: a mechanism for the semi-annual density variation, *Journal of Geophysical Research*, 103(A3), 3951–3956, doi: 10.1029/97JA03335.
- Gallis, M., J. Torczynski, S. Plimpton, D. Rader, and T. Koehler (2014), Direct simulation Monte Carlo: the quest for speed, in *Proceedings of the 29th International Symposium on Rarefied Gas Dynamics*, vol. 1628, edited by J. Fan, pp. 27–36, AIP Publishing, doi: 10.1063/1.4902571.
- Garcia, R., S. Bruinsma, P. Lognonné, E. Doornbos, and F. Cachoux (2013), GOCE: The first seismometer in orbit around the Earth, *Geophysical Research Letters*, 40, 1015–1020.
- Garcia, R., E. Doornbos, S. Bruinsma, and H. Hebert (2014), Atmospheric gravity waves due to the Tohoku-Oki tsunami observed in the thermosphere by GOCE, *Journal of Geophysical Research: Atmospheres*, 119(8), 4498–4506, doi: 10.1002/2013JD021120.
- Gasperini, E., J. Forbes, E. Doornbos, and S. Bruinsma (2015), Wave coupling between the lower and middle thermosphere as viewed from TIMED and GOCE, *Journal of Geophysical Research: Space Physics*, 120(7), 5788–5804, doi: 10.1002/2015JA021300.
- GOCE Flight Control Team (HSO-OEG) (2014), GOCE End-of-Mission Operations Report, *Tech. Rep. GO-RP-ESC-FS-6268*, European Space Agency (ESA).
- Gregory, J., and P. Peters (1987), A measurement of the angular distribution of 5 eV atomic oxygen scattered off a solid surface in Earth orbit, in *Proceedings of the 15th International Symposium of Rarefied Gas Dynamics, Grado, Italy*, vol. 2, edited by V. Boffi and C. Cercignani, pp. 644–654, B. Teubner, Stuttgart, Germany.
- Harding, B., J. Makela, J. Qin, D. Fisher, C. Martinis, J. Noto, and C. Wrasse (2017), Atmospheric scattering effects on ground-based measurements of thermospheric vertical wind, horizontal wind, and temperature, *Journal of Geophysical Research: Space Physics*, 122(7), 7654–7669, doi: 10.1002/2017JA023942.

- Hoffman, R. (1980), Dynamics Explorer Program, *Eos, Transactions American Geophysical Union*, 61(44), 689–692, doi: 10.1029/EO061i044p00689.
- Innis, J., and M. Conde (2002), High-latitude thermospheric vertical wind activity from Dynamics Explorer 2 Wind and Temperature Spectrometer observations: Indications of a source region for polar cap gravity waves, *Journal of Geophysical Research*, 107(A8, 1172), doi: 10.1029/2001JA009130.
- Innis, J., P. Greet, D. Murphy, M. Conde, and P. Dyson (1999), A large vertical wind in the thermosphere at the auroral oval/polar cap boundary seen simultaneously from Mawson and Davis, Antarctica, *Journal of Atmospheric and Solar-Terrestrial Physics*, 61, 1047–1058, doi: 10.1016/S1364-6826(99)00060-7.
- Kärräng, P. (2015), Comparison of thermospheric parameters from space- and ground-based instruments, Master's thesis, Luleå University of Technology.
- King-Hele, D. (2005), *A tapestry of orbits*, Cambridge University Press.
- Knutson, J., D. Kayser, and W. Potter (1977), Mass spectrometric measurements of thermospheric wind, *Journal of Geophysical Research*, 82(32), 5253–5256, doi: 10.1029/JA082i032p05253.
- Kolkmeier, A., G. Präger, P. Möller, T. Strandberg, K. Kempkens, J. Stark, L. Gessler, and K. Hienerwadel (2008), GOCE - DFAC Interface Control Document, *Tech. Rep. GO-IC-ASG-0005\_12*, EADS Astrium.
- Koppenwallner, G. (2008), Comment on special section: New perspectives on the satellite drag environments of Earth, Mars, and Venus, *Journal of Spacecraft and Rockets*, 45(6), 1324–1327, doi: 10.2514/1.37539.
- Koppenwallner, G. (2009), Energy accommodation coefficient and momentum transfer modeling, *Tech. Rep. HTG-TN-08-11*, Hypersonic Technology Göttingen (HTG).
- Larsen, M., and J. Meriwether (2012), Vertical winds in the thermosphere, *Journal of Geophysical Research*, 117(A09319), doi: 10.1029/2012JA017843.
- Liu, H., E. Doornbos, and J. Nakashima (2016), Thermospheric wind observed by GOCE: Wind jets and seasonal variations, *Journal of Geophysical Research: Space Physics*, 121(7), 6901–6913, doi: 10.1002/2016JA022938.
- March, G., E. Doornbos, and P. Visser (2019a), High-fidelity geometry models for improving the consistency of CHAMP, GRACE, GOCE, and Swarm thermospheric density data sets, *Advances in Space Research*, 63(1), 213–238, doi: 10.1016/j.asr.2018.07.009.
- March, G., T. Visser, P. Visser, and E. Doornbos (2019b), CHAMP and GOCE thermospheric wind characterization with improved gas-surface interaction modelling, *Advances in Space Research*, 64(6), 1225–1242, doi: 10.1016/j.asr.2019.06.023.
- Mehta, P., C. McLaughlin, and E. Sutton (2013), Drag coefficient modeling for GRACE using Direct Simulation Monte Carlo, *Advances in Space Research*, 52(12), 2035–2051, doi: 10.1016/j.asr.2013.08.033.

- Mehta, P., A. Walker, E. Lawrence, R. Linares, D. Higdon, and J. Koller (2014), Modeling satellite drag coefficients with response surfaces, *Advances in Space Research*, 54(8), 1590–1607, doi: 10.1016/j.asr.2014.06.033.
- Mehta, P., A. Walker, E. Sutton, and H. Godinez (2017), New density estimates derived using accelerometers on board the CHAMP and GRACE satellites, *Space Weather*, 15(4), 558–576, doi: 10.1002/2016SW001562.
- Moe, K. (1966), Absolute atmospheric densities determined from the spin and orbital decays of explorer VI, *Planetary and Space Science*, 14(11), 1065–1075, doi: 10.1016/0032-0633(66)90022-5.
- Moe, K., and M. Moe (2005), Gas–surface interactions and satellite drag coefficients, *Planetary and Space Science*, 53(8), 793–801, doi: 10.1016/j.pss.2005.03.005.
- Moe, M., S. Wallace, and K. Moe (1993), Refinements in determining satellite drag coefficients: method for resolving density discrepancies, *Journal of Guidance, Control, and Dynamics*, 16(3), 441–445, doi: 10.2514/3.21029.
- Moe, M., S. Wallace, and K. Moe (1995), Recommended drag coefficients for aeronomic satellites, in *The Upper Mesosphere and Lower Thermosphere: A Review of Experiment and Theory (87)*, edited by R. Johnson and T. Killeen, pp. 349–356, American Geophysical Union (AGU), doi: 10.1029/GM087p0349.
- Neil Davis, T., and M. Sugiura (1966), Auroral electrojet activity index AE and its universal time variations, *Journal of Geophysical Research*, 71(3), 785–801, doi: 10.1029/JZ071i003p00785.
- Olsen, N., E. Friis-Christensen, R. Floberghagen, P. Alken, C. Beggan, A. Chulliat, E. Doornbos, J. Teixeira da Encarnação, B. Hamilton, G. Hulot, J. van den IJssel, A. Kuvshinov, V. Lesur, H. Lühr, S. Macmillan, S. Maus, M. Noja, P. E. Olsen, J. Park, G. Plank, C. Püthe, J. Rauberg, P. Ritter, M. Rother, T. Sabaka, R. Schachtschneider, O. Sirol, C. Stolle, E. Thébault, A. Thomson, L. Tøffner-Clausen, J. Velínský, P. Vigneron, and P. Visser (2013), The Swarm Satellite Constellation Application and Research Facility (SCARF) and Swarm data products, *Earth, Planets and Space*, 65(1), doi: 10.5047/eps.2013.07.001.
- Picone, J., A. Hedin, D. Drob, and A. Aikin (2002), NRLMSISE-00 empirical model of the atmosphere: statistical comparisons and scientific issues, *Journal of Geophysical Research: Space Physics*, 107(A12), doi: 10.1029/2002JA009430.
- Pilinski, M., B. Argrow, and S. Palo (2010), Semiempirical model for satellite energy-accommodation coefficients, *Journal of Spacecraft and Rockets*, 47(6), 951–956, doi: 10.2514/1.49330.
- Pilinski, M., K. Moe, S. Palo, and B. Argrow (2011), Measuring absolute thermospheric densities and accommodation coefficients using paddlewheel satellites: past findings, present uses, and future mission concepts, *Journal of the Astronautical Sciences*, 58(3), 531–549, doi: 10.1007/BF03321184.

- Pilinski, M., B. Argrow, S. Palo, and B. Bowman (2013), Semi-empirical satellite accommodation model for spherical and randomly tumbling objects, *Journal of Spacecraft and Rockets*, 50(3), 556–571, doi: 10.2514/1.A32348.
- Rees, D., T. Fuller-Rowell, R. Gordon, T. Killeen, P. Hays, L. Wharton, and N. Spencer (1983), A comparison of wind observations of the upper thermosphere from the Dynamics Explorer satellite with the predictions of a global time-dependent model, *Planetary and Space Science*, 31(11), 1299–1314, doi: 10.1016/0032-0633(83)90067-3.
- Robertson, R. (2015), Highly Physical Solar Radiation Pressure Modeling During Penumbra Transitions, Ph.D. thesis, Virginia Polytechnic Institute and State University, Blacksburg (VA), United States.
- Robertson, R., J. Flury, T. Bandikova, and M. Schilling (2015), Highly physical penumbra solar radiation pressure modeling with atmospheric effects, *Celestial Mechanics and Dynamical Astronomy*, 123(2), 169–202, doi: 10.1007/s10569-015-9637-0.
- Roithmayr, C. (1991), Contribution of zonal harmonics to gravitational moment, *Journal of Guidance, Control, and Dynamics*, 14(1), 210–214, doi: 10.2514/3.20626.
- Rummel, R., W. Yi, and C. Stummer (2011), GOCE gravitational gradiometry, *Journal of Geodesy*, 85, 777–790, doi= 10.1007/s00190-011-0500-0.
- Sarris, T., E. Talaat, M. Palmroth, I. Dandouras, E. Armandillo, G. Kervalishvili, S. Buchert, D. Malaspina, A. Jaynes, N. Paschalidis, J. Sample, J. Halekas, S. Tourgaidis, V. Lappas, M. Clilverd, Q. Wu, I. Sandberg, A. Aikio, and P. Pirnaris (2019), Daedalus: A low-flying spacecraft for the exploration of the lower thermosphere - ionosphere, *Geoscientific Instrumentation, Methods and Data Systems, under review*, doi: 10.5194/gi-2019-3.
- Sentman, L. (1961), Comparison of the exact and approximate methods for predicting free molecule aerodynamic coefficients, *American Rocket Society Journal*, 31(11), 1576–1579.
- Siemes, C. (2018), Improving GOCE cross-track gravity gradients, *Journal of Geodesy*, 92(1), 33–45, doi: 10.1007/s00190-017-1042-x.
- Siemes, C., R. Haagmans, M. Kern, G. Plank, and R. Floberghagen (2012), Monitoring GOCE gradiometer calibration parameters using accelerometer and star sensor data: methodology and first results, *Journal of Geodesy*, 86(8), 629–645, doi: 10.1007/s00190-012-0545-8.
- Siemes, C., J. De Teixeira Da Encarnação, E. Doornbos, J. Van Den IJssel, J. Kraus, R. Perešty, L. Grunwaldt, G. Apelbaum, J. Flury, and P. Holmdahl Olsen (2016), Swarm accelerometer data processing from raw accelerations to thermospheric neutral densities 2. Aeronomy Swarm science results after two years in space, *Earth, Planets and Space*, 68(1), 92, doi: 10.1186/s40623-016-0474-5.
- Sipler, D., M. Biondi, and M. Zipf (1995), Vertical winds in the midlatitude thermosphere from Fabry–Perot Interferometry measurements, *Journal of Atmospheric and Terrestrial Physics*, 57(6), 621–629, doi: 10.1016/0021-9169(94)00102-T.

- Smith, R. (1998), Vertical winds: a tutorial, *Journal of Atmospheric and Solar-Terrestrial Physics*, 60, 1425–1434, doi: 10.1016/S1364-6826(98)00058-3.
- Smith, R., and G. Hernandez (1995), Vertical winds in the thermosphere within the polar cap, *Journal of Atmospheric and Terrestrial Physics*, 57(6), 611–620, doi: 10.1016/0021-9169(94)00101-S.
- Spencer, N., H. Niemann, and G. Carignan (1973a), The neutral-atmosphere temperature instrument, *Radio Science*, 8(4), 287–296, doi: 10.1029/RS008i004p00287.
- Spencer, N., L. Brace, and D. Grimes (1973b), The Atmosphere Explorer spacecraft system, *Radio Science*, 8(4), 267–269, doi: 10.1029/RS008i004p00267.
- Spencer, N., R. Theis, L. Wharton, and G. Carignan (1976), Local vertical motions and kinetic temperature from AE-C as evidence for aurora-induced gravity waves, *Geophysical Research Letters*, 3(6), 313–316, doi: 10.1029/GL003i006p00313.
- Spencer, N., L. Wharton, H. Niemann, A. Hedin, G. Carignan, and J. Maurer (1981), The Dynamics Explorer wind and temperature spectrometer, *Space Science Instrumentation*, 5(4), 417–428.
- Spencer, N., L. Wharton, G. Carignan, and J. Maurer (1982), Thermosphere zonal winds, vertical motions and temperature as measured from Dynamics Explorer, *Geophysical Research Letters*, 9(9), 953–956, doi: 10.1029/GL009i009p00953.
- Stummer, C. (2012), Gradiometer Data Processing and Analysis, Ph.D. thesis, Technische Universität München, Munich, Germany.
- Sutton, E. (2009), Normalized force coefficients for satellites with elongated shapes, *Journal of Spacecraft and Rockets*, 46(1), doi: 10.2514/1.40940.
- Sutton, E., J. Forbes, and R. Nerem (2005), Global thermospheric neutral density and wind response to the severe 2003 geomagnetic storms from CHAMP accelerometer data, *Journal of Geophysical Research: Space Physics*, 110(A9), doi: 10.1029/2004JA010985.
- Trinh, Q., M. Ern, E. Doornbos, P. Preusse, and M. Riese (2018), Satellite observations of middle atmosphere-thermosphere vertical coupling by gravity waves, *Annales Geophysicae*, 36(2), 425–444, doi: 10.5194/angeo-36-425-2018.
- Virgili-Llop, J., P. Roberts, and Z. Hao (2018), Using the attitude response of aerostable spacecraft to measure thermospheric wind, *CEAS Space Journal*, 10(1), 101–113, doi: 10.1007/s12567-017-0153-9.
- Visser, P., and J. van den IJssel (2016), Calibration and validation of individual GOCE accelerometers by precise orbit determination, *Journal of Geodesy*, 90, 1–13, doi: 10.1007/s00190-015-0850-0.
- Visser, P., E. Doornbos, J. van den IJssel, and J. Teixeira da Encarnação (2013), Thermospheric density and wind retrieval from Swarm observations, *Earth, Planets and Space*, 65(11), doi: 10.5047/eps.2013.08.003.

- Visser, T., E. Doornbos, C. de Visser, P. Visser, and B. Fritsche (2018), Torque model verification for the GOCE satellite, *Advances in Space Research*, 62(5), 1114–1136, doi: 10.1016/j.asr.2018.06.025.
- Visser, T., G. March, E. Doornbos, C. de Visser, and P. Visser (2019a), Horizontal and vertical thermospheric cross-wind from GOCE linear and angular accelerations, *Advances in Space Research*, 63(10), 3139–3153, doi: 10.1016/j.asr.2019.01.030.
- Visser, T., G. March, E. Doornbos, C. de Visser, and P. Visser (2019b), Characterization of thermospheric vertical wind activity at 225- to 295-km altitude using GOCE data and validation against Explorer missions, *Journal of Geophysical Research: Space Physics*, 124(6), 4852–4869, doi: 10.1029/2019JA026568.
- Walker, A., P. Mehta, and J. Koller (2014a), Drag coefficient model using the Cercignani–Lampis–Lord gas–surface interaction model, *Journal of Spacecraft and Rockets*, 51(5), 1544–1563, doi: 10.2514/1.A32677.
- Walker, A., P. Mehta, and J. Koller (2014b), Different implementations of diffuse reflection with incomplete accommodation for drag coefficient modeling, *Journal of Spacecraft and Rockets*, 51(5), 1522–1532, doi: 10.2514/1.A32668.
- Wallace, N., P. Jameson, C. Saunders, M. Fehringer, C. Edwards, and R. Floberghagen (2011), The GOCE ion-propulsion assembly - lessons learnt from the first 22 months of flight operations, in *32nd International Electric Propulsion Conference, Wiesbaden, Germany*, IEPC-2011-327.
- Wertz, J. (1978), *Spacecraft attitude determination and control*, Springer Netherlands, doi: 10.1007/978-94-009-9907-7.
- Wie, B. (2008), *Space Vehicles Dynamics and Control*, American Institute of Aeronautics and Astronautics.

# CURRICULUM VITÆ

## Tim VISSER

14-03-1991 Born in Groningen, The Netherlands.

### EDUCATION

1995–2003 Primary school  
Bisschop Bekkersschool, Groningen

2003–2009 Secondary school  
Willem Lodewijk Gymnasium, Groningen

2009–2012 BSc in Aerospace Engineering  
Delft University of Technology, Delft

2012–2014 MSc in Aerospace Engineering: Control and Simulation  
Delft University of Technology, Delft

2014–2019 PhD in Aerospace Engineering: Astrodynamics and Space Missions  
Delft University of Technology, Delft  
*Thesis:* Cross-wind from linear and angular satellite dynamics: the GOCE perspective on horizontal and vertical wind in the thermosphere  
*Promotor:* Prof. dr. P.N.A.M. Visser

### AWARDS

2010 Best Propaedeutic Exam in Aerospace Engineering 2009–2010

2015 Best Graduate in Aerospace Engineering 2014–2015



# LIST OF PUBLICATIONS

## JOURNAL PUBLICATIONS

4. G. March, **T. Visser**, P. Visser, and E. Doornbos, *CHAMP and GOCE thermospheric wind characterization with improved gas-surface interaction modeling*, [Advances in Space Research](#) **64** (6), 2019.
3. **T. Visser**, G. March, E. Doornbos, C. de Visser, and P. Visser; *Characterization of thermospheric vertical wind activity at 225- to 295-km altitude using GOCE data and validation against Explorer missions*, [Journal of Geophysical Research: Space Physics](#) **124** (6), 2019.
2. **T. Visser**, G. March, E. Doornbos, C. de Visser, and P. Visser; *Horizontal and vertical thermospheric cross-wind from GOCE linear and angular accelerations*, [Advances in Space Research](#) **63** (10), 2019.
1. **T. Visser**, E. Doornbos, C. de Visser, P. Visser, and B. Fritsche; *Torque model verification for the GOCE satellite*, [Advances in Space Research](#) **62** (5), 2018.

## CONFERENCE PUBLICATIONS

2. M. van den Aarsen, **T. Visser**, and C. de Visser; *Distributed approach for aerodynamic model identification of the ICE aircraft using the alternating direction method of multipliers in combination with simplotope B-splines*, [AIAA SciTech Forum, San Diego \(CA\)](#), 2019.
1. **T. Visser**, C. de Visser, and E. van Kampen; *Quadrotor system identification using the multivariate multiplex B-spline*, [AIAA Atmospheric Flight Mechanics Conference, Kissimmee \(FL\)](#), 2015.